Enhancing $J_c(B,\theta)$ in $YBa_2Cu_3O_{7-\delta}$ via nano-engineering of pinning structures

Rose Lyn Salangsang Emergo

B.S. Applied Physics, University of the Philippines at Los Baños, 1999

Submitted to the Department of Physics and Astronomy and the Faculty of the

Graduate School of the University of Kansas in partial fulfillment of the requirement

for the degree of Doctor of Philosophy

Dissertation Committee:

_____

Chair: Dr. Judy Z. Wu

_____

Dr. Philip S. Baringer

_____

Dr. Siyuan Han

_____

Dr. Karen J. Nordheden

_____

Dr. Hui Zhao

Date Defended: April 16, 2009

The Dissertation Committee for Rose Lyn Salangsang Emergo certifies that this is the

approved version of the following dissertation:

Enhancing $J_c(B,\theta)$ in $YBa_2Cu_3O_{7-\delta}$ via nano-engineering of pinning structures

_____

Chair: Dr. Judy Z. Wu

Date approved: April 27, 2009

Abstract

Critical current density (J_c) has been identified as one of the most critical parameters for the practical application of high temperature superconductors such as $YBa_2Cu_3O_{7-\delta}$ (YBCO). Unfortunately, the J_c of optimized un-doped YBCO films barely satisfies the criteria for these applications. High J_c can be achieved by introducing strong artificial pinning centers in YBCO which can inhibit flux motion and prevent dissipation. However, insertion of strong pins has been observed to strain and poison the YBCO lattice resulting in unnecessary degradation of T_c and low field J_c. In this work, two types of strong pinning centers with negligible effect on the T_c and low field J_c were incorporated in YBCO films via strain engineering on the nanoscale. The nanotube pores were generated by depositing YBCO films on vicinal $SrTiO_3$ (STO) substrates. A close correlation between J_c and the magnetic pinning potential U_p of the nanotube pores has been demonstrated below the accommodation field, suggesting that nanotube pores are strong pins on the magnetic vortices. Splayed $BaZrO_3$ nanorords (BZO-NRs) were generated in YBCO film by depositing 2 vol.% BZO-doped YBCO on vicinal STO substrates. The interplay between the lattice strain caused by the large lattice mismatch between YBCO and BZO and the anisotropic strain due to vicinal growth resulted in the dispersed orientation of BZO-NRs. The splayed BZO-NRs led to an enhanced J_c in the entire range of the magnetic field orientation up to 5 T as compared to the non-splayed case of YBCO/BZO-NRs films.

Dedication

This dissertation is dedicated to my Nanay, Tatay and my sister Rea.

Acknowledgements

I would like to thank everyone who has sustained me during these seven and a half years of my journey in graduate school. To everyone who has clothed, fed, sheltered, encouraged and prayed for me, I could have not done it without you. I am hoping that someday I will be able to return all the kindness that you have shown me.

This journey would have not been possible without my research adviser, Dr. Judy Wu. Thank you very much for having faith in me and fighting for me so that I can achieve this dream. Thank you for believing in me even at times when I didn't believe in myself. Thank you for not letting me give up on my Ph.D. You have taught me to persevere, to work hard and to think smart. You have pushed me to be the best that I can be and you have made me love Physics even more. I really have no idea how to thank you. You have changed my life. My whole family and I will always be grateful for this opportunity.

I am also indebted to Dr. Albert A. Gapud who opened the doors for me to come to KU and to become Dr. Wu's student. Thank you so much for everything.

I would like to thank my dissertation committee for their valuable inputs: Dr. Philip Baringer, Dr. Siyuan Han, Dr. Karen Nordheden and Dr. Hui Zhao. Dr. Han, you have served as an inspiration for me. Our class in Solid State Physics 1 is the most memorable class I had at KU. I have learned so much from you and I hope that someday I will be as knowledgeable as you are.

I would like to thank the amazing staff of the Department of Physics and Astronomy at KU namely: John Clune, Bob Curry, Doug Fay, Tess Gratton, Alan Hase, Kim Hubble, Zach Kessler, Nicky Kolatch, Teri Leahy, Don Nieto and Jeff Worth.

I would like to thank my lab mates both past and present. This journey has been more bearable and pleasant because of you. Dr. Sangho Yun, who was my first mentor when I joined the group, thank you for teaching me how to fabricate films using the PLD system. Dr. Roberto S. Aga, who was my big brother in the lab, thanks for all the measurement and photolithography techniques that you have taught me. Dr. Ronald N. Vallejo, who was my second big brother in the lab, thanks for teaching me the sputtering and e-beam technique. To Hua Zhao, Xiang Wang, Javier Baca and Jonathan Dizon, my batch mates and friends, thank you for sharing your knowledge with me. I have learned so much from all of you. Thank you for helping me during all those rigorous measurements and film fabrications and most of all, thank you for standing by me during those tough times of Ph.D. life. I wish you all the best in life. May all of us reap the sacrifices that we have made for our Ph.D. To Caitlin Rochford, Guowei Xu, Dr. Rongtao Lu and Dr. Zhuangzhi Li, thank you so much for all your help. I have learned so much from you and I cherish the time that I have spent with you.

I would like to thank my international friends, Haruko Nakano, Shimantini Shome, Dimitra Atri, Odessa Reis, Sakeeb Mehdi, Elodie Lasserre, Barbara Starr and Yisin Tan, who have been constant sources of support and adventure for me. Yisin

and Barb, thank you so much for the love and acceptance that you have given me. I am not sure what the future will bring to us, but I will always be here for you no matter what.

My Filipino friends in Kansas have been a big support to me. The Schmidt's, the Aga's and the Vallejo's have welcomed me so warmly when I first came to KU. Thank you very much for helping me adjust to my new home. Thank you so much Kuya Brian and Ate Cheryl Ocfemia for welcoming me into your lives. You have been a big part of this journey. I have so much to thank you for and I don't even know where to begin. I am just very, very grateful to you. To my fellow Filipino KU graduate students (Ate Lynn, Joseph, Maila, Ferdinand, Carl, Julius, Robert, Aileen and Ate Nette) thank you very much for the support and encouragements. I will definitely miss your company.

To my darling Julien, who is my source of love and joy, thank you so much for everything. It has been a tough journey for us but it was all worth it. I wish you all the success in your Ph.D. I love you very much.

I would like to thank my Nanay, Tatay and my sister Rea for all the love, support and prayers. Thank you so much for being the wind beneath my wings. I have soared this high because of you. You have enabled me to dream and now, finally, it has come true. I love you all very much.

Thank you Lord for sustaining me. I am nothing without you.

List of Figures

profile. The x-direction in the inset is the scan direction defined by the green line in (d). A NP at the bottom of the pore can be clearly seen. [Data taken by Guowei Xu.]

Figure 4.5 (a) TEM cross-section of a nanopore; (b) TEM image of the base of a nanopore showing a nanoparticle underneath; (c) higher resolution image of the nanoparticle. [Data taken by Dr. Hong Hui Chou.]

Figure 4.6 Comparison of the longitudinal J_c values of a reference and three porous vicinal YBCO films with H‖film normal at (a) 77 K and (b) 65 K. All samples have thickness of 0.2 μm. [Wu 2008]

Figure 4.7 (a) Comparison of the J_c and N values of the four samples shown in Figure 4.6 at 77 K and 0.01 T. (b) Normalized N-value and J_c as function of H for a porous 20º vicinal YBCO film. Inset refers to the I-V curves at different applied H fields. [Emergo 2008]

Figure 4.8 Pinning force per volume as function of the applied H field for a flat, 8º nonporous vicinal (derived from Cantoni 2005 data) and 10º porous vicinal YBCO films. [Emergo 2008]

Fig 5.1 Resistivity versus temperature plots of the longitudinal and transverse bridges of 0.2 μm-thick porous 5°, 10° and 20° vicinal YBCO films. [Emergo 2008]

Figure 5.2 Temperature dependence of ρ_c of the porous 5°, 10° and 20° vicinal YBCO films. [Emergo 2008]

Figure 5.3 (a) Temperature dependence of ρ_c/ρ_{ab} for the porous 5°, 10° and 20° vicinal YBCO films; (b) Normalized temperature dependence of ρ_c/ρ_{ab} for the three samples mentioned above. [Emergo 2008]

Figure 5.4 MO images of flux behavior in the 0.2 μm thick (a) flat and (b) 10° vicinal YBCO samples taken at temperature T=10 K and H= 28 mT. 2*w* is the sample width, 2*b* is the width of flux-free Meissner region and *PL* and *PT* are the depths of flux penetration parallel and perpendicular to the steps of growth, respectively. [Polyanskii 2005]

Figure 5.5 (a) Contours of the magnetization current streamlines and (b) current distribution map calculated by deconvolution procedure for MO image of the same sample in Figure 5.4(b) taken at 10 K and 120 mT. [Polyanskii 2005]

Figure 5.6 Temperature dependence of J_c in the 0.2 μm thick flat and 10° vicinal YBCO samples. Inset: T dependence of the J_c anisotropy ($J_{c,L}$ /$J_{c,T}$) in the vicinal sample. [Polyanskii 2005]

List of tables

Contents

xv

Chapter 1

Introduction

1.1 Brief introduction to superconductivity

The first superconductors were discovered by Kamerlingh Onnes in 1911. During that time, he had successfully liquefied helium and he was determining the temperature dependence of the resistance of mercury as T approaches zero. Surprisingly, he observed that the resistance disappeared at 4.2 K, which is shown in Figure 1.1 [Onnes, 1911]. This perfect conductivity at temperatures below the critical temperature (T_c) is the first trademark of superconductivity. Furthermore, his group also discovered that applying a certain current and magnetic field at a particular temperature, which are known as critical current density (J_c) and critical field (H_c), could destroy this superconducting property.
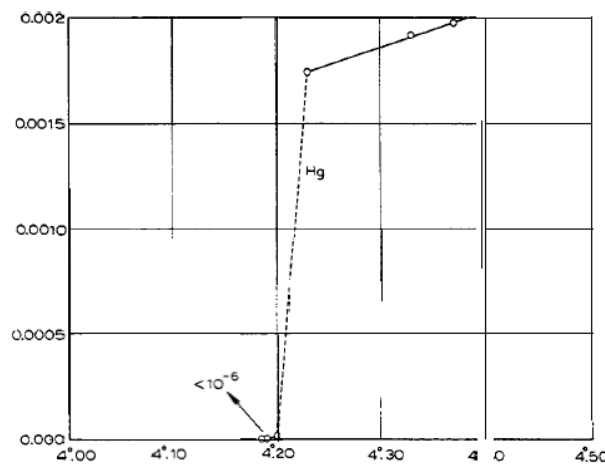
Figure 1.1 Original resistance vs. temperature curve of mercury by K. Onnes.[Onnes, 1911]

Aside from having zero resistance below T_c, superconductors also exhibit perfect diamagnetism. This phenomenon, discovered by Meissner and Ochsenfeld in 1933, demonstrated that a certain applied magnetic field is expelled out of the superconductor, signifying that superconductivity is more than perfect conductivity [Meissner, 1933]. Figure 1.2 illustrates the Meissner effect in a superconductor. Before the transition temperature is reached as temperature decreases, the applied magnetic field penetrates the material. But as soon as the material turns superconducting, the applied magnetic field is completely expelled from the superconductor.
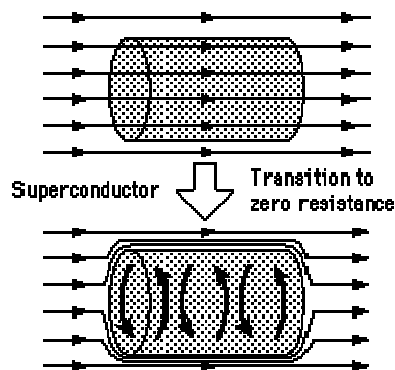
Figure 1.2 Illustration of Meissner effect in superconductors. [http://hyperphysics.phy-astr.gsu.edu]

1.1.1 Theories of superconductivity

a. Microscopic BCS Theory

A theory that has been successful in explaining superconductivity is known as the BCS theory named after Bardeen, Cooper and Schreiffer [Bardeen 1957, Campbell 1972, Tinkham 1996, Huebner 2001 and Matsushita 2008]. The BCS theory explains that the absence of resistance in superconductors is due to electrons

pairing up and moving along the crystal lattice without any collisions. These pairs are known as ***Cooper pairs*** and are formed through electron-phonon interactions. When an electron moves in a crystal lattice, it distorts the lattice around it and creates an area of greater positive charge density around itself. Another electron, with an equal but opposite spin and momentum, at some distance in the lattice is then attracted to this charge distortion. The electrons are thus indirectly attracted to each other and form a Cooper pair. Since each Cooper pair is composed of electrons with opposite spins, it can be viewed as a particle with zero total spin, which suggests that Cooper pairs can have the same quantum state at the same time. Thus, at superconducting state, all Cooper pairs are correlated and they can all move together. These Cooper pairs, having dimensions on the order of ξ and comprising the conducting charge carriers, require a minimum energy, $E_g \approx \gamma k_B T_c$, (where γ is a fixed universal value according to BCS theory) to break them. Interestingly, the ratio between the value of the energy gap at zero temperature and the T_c value (expressed in energy units) takes the universal value of 3.528 regardless of the material's nature. The BCS theory predicted a theoretical maximum T_c of around 30 K because above this the thermal energy would be too high to allow formation of Cooper pairs. But in 1986, superconductors of T_c around 90 K were discovered. Up to now, the mechanism responsible for the pairing of charge carriers in high-T_c superconductors is still unknown. There are significant numbers of models describing superconductivity. Most of them are phenomenological in nature, which means that they describe superconductivity but they do not explain how superconductivity occurs.

3

b. London Theory

The first theory that attempted to describe superconductivity was proposed by the London brothers in 1935 [London 1950 and London 1963]. Since a steady, persistent current can flow through superconductors, the superconducting electrons are accelerated only by the local applied electric field $\vec{E}$. Consequently, the equation of motion can be written as $m\dfrac{d\vec{v}}{dt}=-e\vec{E}$, where m, e and $\vec{v}$ are the mass, charge and velocity of the superconducting electrons. At the same time, the critical current density $\vec{j}$ of the superconductor can be expressed as $\vec{j}=-n_e e \vec{v}_s$, where n_s is the density of the superconducting electrons. Substituting this equation into the first equation gives an expression for the local electric field: $\vec{E}=\dfrac{m}{e^2 n_e}\dfrac{d\vec{j}}{dt}$. The latter equation is known as the first London equation [Campbell 1972, Tinkham 1996, Huebner 2001 and Matsushita 2008].

Applying the Maxwell equation $\vec{\nabla}\times\vec{E}=-\dfrac{\partial\vec{B}}{\partial t}$ to the first London equation, the following can be derived: $\dfrac{m}{e^2 n_e}\left(\vec{\nabla}\times\dfrac{d\vec{j}}{dt}\right)=-\dfrac{\partial\vec{B}}{\partial t}$. Furthermore, if $\vec{\nabla}\times\dfrac{\vec{B}}{\mu_o}$ is substituted to $\vec{j}$ in the latter, the first London equation transforms to $\dfrac{d}{dt}\left(\dfrac{m}{e^2 n_e \mu_o}\left(\vec{\nabla}\times\vec{\nabla}\times\vec{B}\right)+\vec{B}\right)=0$. Thus, the quantity inside the parenthesis is a constant and does not vary with time. The London brothers showed that the Meissner

effect can be explained if this constant is made equal to zero. This is known as the second London equation: $\dfrac{m}{e^2 n_e \mu_o}\left(\vec{\nabla}\times\vec{\nabla}\times\vec{B}\right)+\vec{B}=0$.

The expression $\vec{\nabla}\times\vec{\nabla}\times\vec{B}$ can be replaced by $\nabla^2\vec{B}$ since $-\vec{\nabla}\cdot\vec{B}=0$. Consequently, the second London equation can be expressed as $\nabla^2\vec{B}-\dfrac{1}{\lambda^2}\vec{B}=0$, where $\lambda=\left(\dfrac{m}{e^2 n_e \mu_o}\right)^{1/2}$, which is known as the London penetration depth. For a thin slab of superconductor with an applied external magnetic field (H_e) perpendicular to the superconductor's surface, the solution to this differential equation is $B(x)=\mu_o H_e e^{-x/\lambda}$. This shows that the applied magnetic field can only penetrate the superconductor surface by a distance on the order of λ. Furthermore, application of the Maxwell equation $\vec{\nabla}\times\dfrac{\vec{B}}{\mu_o}=\vec{j}$ on the latter equation gives the local current density $j(x)=\dfrac{H_e}{\lambda}e^{-x/\lambda}$. This so-called Meissner current shields the external field thereby supporting the Meissner effect.

Although the London theory is able to explain the Meissner effect and the corresponding screening current, it is not capable of explaining the simultaneous existence of superconducting and normal states in superconductors. Furthermore, the London theory focuses on the microscopic behavior of a superconductor which is problematic especially since the response of an electron gas to an external electric

5

field is non-local. However, the theory proves to be valid for situations wherein the superconducting properties are homogeneous over a certain spatial region.

    c. Ginzburg-Landau Theory

Due to the non-localization of the superconducting properties, it is more convenient to use the Ginzburg-Landau theory to describe the macroscopic behavior of superconductors. One of the main contributions of this theory is the introduction of the following parameters: order parameter, penetration depth and the coherence length. The order parameter ψ describes how deep into the superconducting phase the system is. The penetration depth $\lambda(\mathrm{T}) = \left[\dfrac{m^* c^2}{4\pi e^{*2} \psi_o} \right]^{1/2}$ is defined as the extent to which the magnetic field pierces a superconducting region. The m* and e* are, respectively, the mass and charge of the charge carrier. Lastly, the coherence length $\xi(\mathrm{T}) = \dfrac{h}{\left| 2m^* \alpha(\mathrm{T}) \right|^{1/2}}$, where $\alpha(\mathrm{T})$ is a constant, is defined as the distance over which the order parameter $\psi(\mathbf{r})$ can vary without undue energy increase. The ratio between λ and ξ, also known as the Ginzburg-Landau parameter ($\kappa = \lambda/\varepsilon$), determines what category of superconductor a material falls into.

1.1.2 Types of Superconductors

Type I superconductors have $\kappa < 1/\sqrt{2}$. The field dependence of the magnetization for this type of superconductor is divided into two regions. For the region below $H_c(\mathrm{T})$, the applied field is expelled from the superconducting material and hence the latter is in the *Meissner state*. On the other hand, the superconductor

turns into a normal material when the applied field exceeds $H_c(T)$. The field dependence of the magnetization for a Type I superconductor is illustrated in Figure 1.3(a) [Campbell 1972, Tinkham 1996, Huebner 2001 and Matsushita 2008].

In the case of Type II superconductors, where $\kappa > 1/\sqrt{2}$, the wall energy separating the superconducting and normal regions becomes negative. In order to lower the free energy of the system, it is necessary to increase the interface between the superconducting and normal regions of the superconductor. This leads to the dispersion of the magnetic flux inside the superconductor into individual flux quanta, Φ_o, where the vortices arrange themselves into a stable configuration called the vortex lattice. This leads to three distinct regions in the magnetization curve of the Type II superconductor (Figure 1.3(b)). For applied field strengths lower than H_{c1}, the superconductor exhibits perfect diamagnetism, above H_{c2} the superconductivity is completely destroyed and when $H_{c1} \leq H \leq H_{c2}$ we have what we call the mixed state where some of the magnetic field penetrates the superconducting matrix [Campbell 1972, Tinkham 1996, Huebner 2001 and Matsushita 2008].
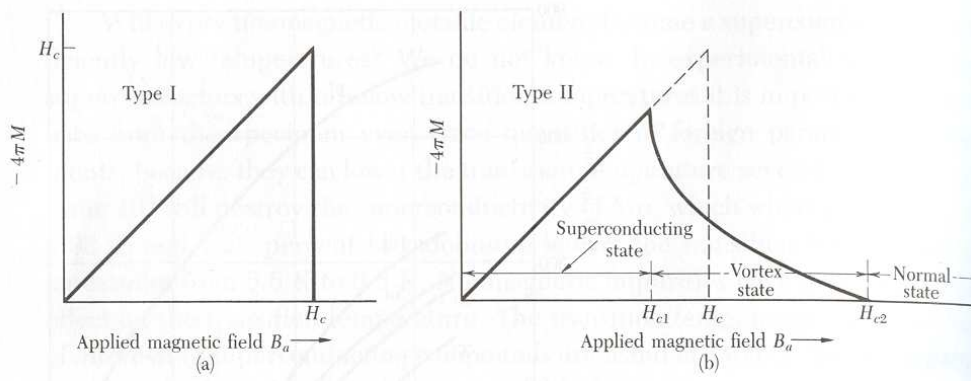
Figure 1.3 The magnetization curve for (a) type I and (b) type II superconductors. [Huebner 2001]

The photograph below shows the top surface of a type II superconductor that has been decorated by tiny micron-sized nickel particles as the applied field was set between H_{c1} and H_{c2}. The particles coalesced on the surface along lines of constant flux density and formed a triangular array. The flux from each pattern throughout the slab is known as the *vortex*. If the distance between the centers of nearest patterns is α, the density of patterns n_v is then $n_v = \dfrac{2}{\sqrt{3}\alpha^2}$. Because each pattern looks identical, the flux in each vortex Φ_v must be the same. Therefore, the average flux density in the slab is $\langle B \rangle = n_v \Phi_v$. Since both $\langle B \rangle$ and α can be measured, then the value of Φ_v can be extracted experimentally and it is always found to be a single flux quantum Φ_o.
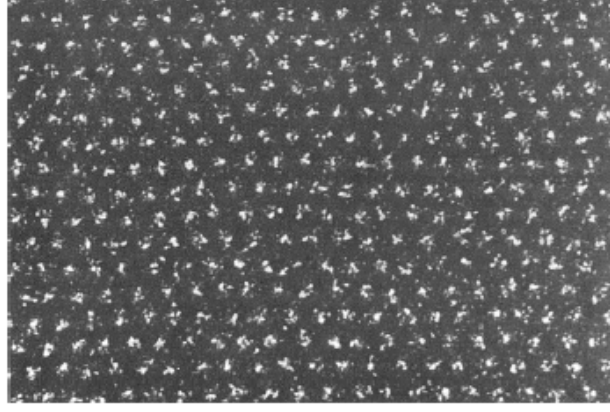
Figure 1.4 A Type II superconductor decorated with magnetic particles. [Campbell 1972, Tinkham 1996, Huebner 2001 and Matsushita 2008]

Since H_{c2} can be much greater than H_c, type II superconductors have been deemed more relevant for technological applications than their type I counterparts. As a matter of fact, type II superconductors have made it possible to achieve high-field superconducting magnets. Another important parameter for the applicability of a type II superconductor is the amount of current it can carry before turning back to its normal state, typically known as its critical current density (J_c). In the next sections, the factors affecting the J_c in type II superconductors, specifically in high-T_c ones (HTSs), will be discussed.

1.2 Depairing J_c in superconductors

The depairing J_c is the necessary J_c required to break the Cooper pairs and is considered as the theoretical limit of J_c in superconductors. The current density in a superconductor is defined as $\vec{J_s} = 2e|\psi|^2 \vec{v_s}$ where $|\psi|^2 = n_s$, the density of

superconducting electrons. Using Ginzburg-Landau's theory, $\vec{J}_s$ can be expressed in

terms of the order parameter ψ so, $J_s = 2e\psi_\infty^2 \left(1 - \dfrac{m^* v_s^2}{2|\alpha|}\right) v_s$. The behavior of J_s as a

function of the depairing velocity, v_s, is plotted in Figure 1.5 and shows that at a

certain critical velocity the Cooper pairs have higher energy than the energy gap. This

results in pair breaking and a lower density of superconducting electrons leading to a

decreased current density.
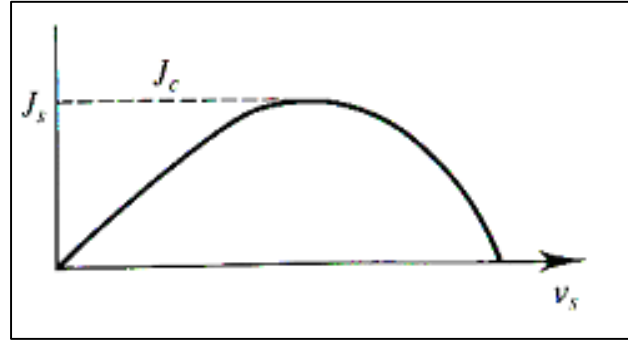
Figure 1.5 Variation of J_s with the super fluid velocity
v_s. [Tinkham 1996]

The maximum J value, J_c, is achieved when $\dfrac{\partial J_s}{\partial v_s} = 0$. This yields to a value of

$v_s = \sqrt{\dfrac{2|\alpha|}{3m^*}}$ and plugging this back into the current density equation yields

$J_c = 2e\psi_\infty^2 \dfrac{2}{3}\left(\dfrac{2}{3}\dfrac{|\alpha|}{m^*}\right)^{1/2}$. In terms of more measurable quantities, where

$\alpha(T) = -\dfrac{2e^2}{m^* c^2} H_c^2(T)\lambda_{\text{eff}}^2(T)$, $|\psi_\infty|^2 = \dfrac{m^* c^2}{8\pi e^2 \lambda_{\text{eff}}^2(T)}$ and $H_c(T) = \dfrac{\Phi_o}{2\pi\sqrt{2}\xi(T)\lambda_{\text{eff}}(T)}$,

10

(where $\Phi_{\circ} = hc/2e = 2.07 \times 10^{-7} G \cdot cm^2$, is the flux quantum) the critical current density

will be $J_c \approx \dfrac{c\Phi_{o}}{\lambda^2 \xi}$ [Orlando 1991]. For type II HTSs like YBa$_2$Cu$_3$O$_{7-\delta}$ (YBCO) with

ξ=35 Å [Poole 2000] and λ=2600 Å [Poole 2000] at 77 K, the calculated depairing J_c

is equal to 5×10^7 A/cm^2. However, the depairing J_c is not readily achieved in

superconductors because dissipation occurs due to the interaction of $\vec{J}$ and $\vec{B}$.

If the width and thickness of a superconducting wire or film are of the same

order or less than λ or ξ, no vortex lines can be accommodated in this configuration.

Thus, films that are too narrow to contain a pair of vortices should not suffer this

critical-current degradation due to dissipative flux motion. This has been observed

experimentally in low temperature superconductors when the width of lead and tin

were made smaller than the width of a pair of vortices [Hunt 1966]. They observed a

depairing J_c of $\sim 5 \times 10^7$ A/cm^2 for a lead film with width of 1 μm and thickness of 475

Å which is comparable to the theoretical value of 7.46×10^7 A/cm^2 [Hunt 1966].

Unfortunately this depairing J_c has not been achieved in HTSs' such as

YBCO. This gives us motivation to understand what dictates the critical current

density in high temperature superconductors.

1.3 Structure, motion, and pinning of magnetic vortices

For type II superconductors, when the applied field is near H_{c1}, the magnetic

vortices start to penetrate the superconductor. These magnetic vortices can be taken

as tubes of normal phase with radius of ξ embedded inside the superconductor. A

schematic diagram of an isolated vortex is shown in Figure 1.6 [Matshushita 2000 and 2007].
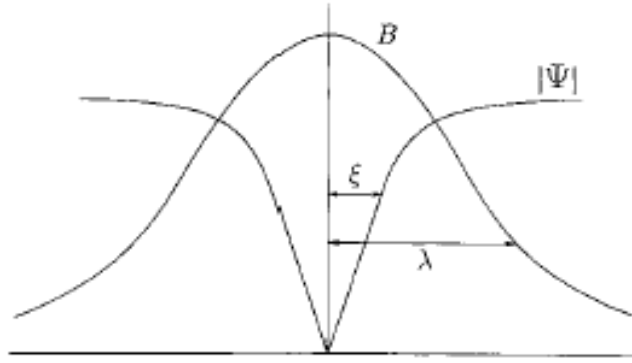
Figure 1.6 Structure of a quantized flux line. [Matshushita 2000 and 2007]

At the vortex core, the density of superconducting electrons, n_s, is zero and its value is a maximum at the radius approximately equal to ξ. The local magnetic field B is highest inside the vortex core and diminishes exponentially beyond a radius on the order of λ. The critical current density J_s of the circular supercurrents generating the field B of the vortex line has its maximum value at a radius equal to λ and vanishes at the vortex core. For magnetic fields slightly stronger than B_{c1}, the vortices are considered to be isolated since they are separated by more than λ and the interaction among neighboring vortices is negligible. When the applied magnetic field is moderate, $B_{c1} \leq B < B_{c2}$, the vortices are within interaction range and when $B=B_{c2}$ the vortex cores overlap and turn the whole superconductor into a normal material.

The vortex structure shows circular symmetry when B is parallel to the c-axis of the superconductor. However, for layered HTSs such as YBCO, the vortex

structure becomes anisotropic when the external magnetic field is applied parallel to either the a- or b-axis (Figure 1.7). The core radius along the plane direction will be ξ_{ab} while the core radius in the c direction will be $\xi_c \ll \xi_{ab}$. On the other hand, the flux-penetration radius will be λ_c along the plane direction and along the c direction it will be λ_{ab}, which is smaller. Thus, the vortex core and current streamlines confining the flux are ellipsoidal in shape.
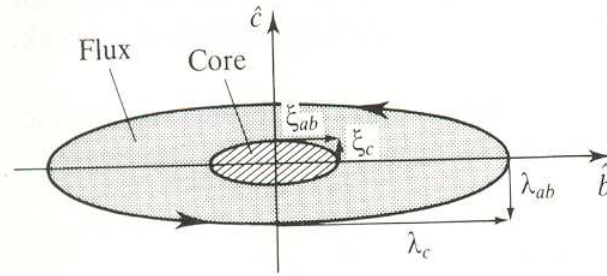
Figure 1.7 Schematic cross section of a vortex along the **a**-axis in an anisotropic superconductor. [Huebner 2001]

The interaction between the current density and the magnetic vortices produces a Lorentz force density defined as $\vec{F_L} = \vec{J} \times \vec{B}$. This force can be generated by both an electrical transport current and by the shielding current associated with the magnetization of the sample. The Lorentz force drives the magnetic vortices outside the superconducting matrix causing dissipation and destroying superconductivity. Flux motion can be prevented if the vortices are pinned on fixed locations inside the superconducting material by a pinning force F_p, which is determined by the pinning potential well. In this regard, the Lorentz force can be viewed as a tilting agent to the potential well, allowing flux lines to hop out of their pinning wells more easily and

13

resulting in the appearance of electrical resistance. This flux motion is known as flux flow and its mechanism is illustrated in Figure 1.8. Therefore, the balance between the driving force and pinning force, known as the critical state, determines the J_c.

The superconducting current originating from the pinning mechanism is assumed to be persistent in time as long as all external conditions are unchanged. However, a decrease in the magnetization of the superconductor with respect to time suggests that the pinning of magnetic vortices is quasi-stable [Matsushita 2007]. As a matter of fact, the magnetic vortices acquire additional energy through thermal activation, which permits the magnetic vortices to move. Such flux motion is called flux creep.
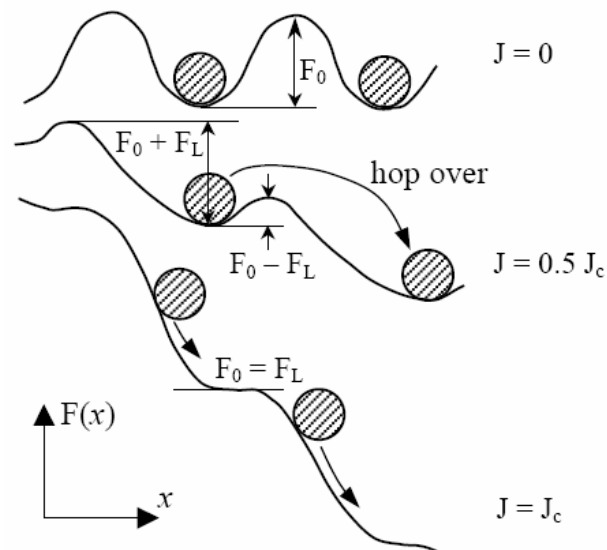
Figure 1.8 Mechanism of flux-flow. [Stavrev 2002]

14

1.4 Angular dependence on J_c

Earlier, it was shown that the magnetic vortices are anisotropic in layered HTSs, such as YBCO. Figure 1.9 illustrates the lattice structure of YBCO containing superconducting planes separated by almost insulating blocks. More specifically, it is composed of CuO_2 conducting layers where superconductivity takes place, a YCO separating layer and a BaO bridging layer which is connected to the CuO chains that act as charge reservoirs.
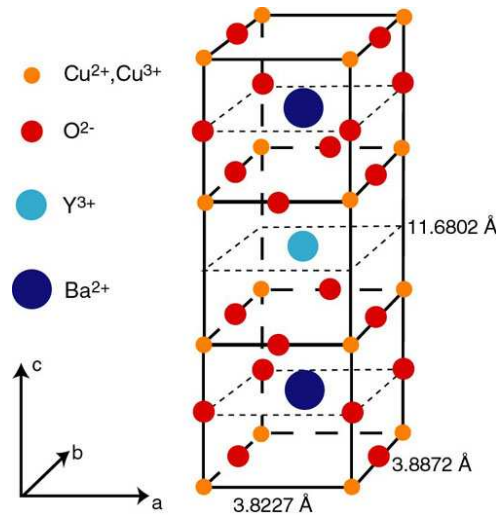
Figure 1.9 Schematic diagram of a unit cell of YBCO crystal. [http://www.tkk.fi]

Interestingly, intrinsic pinning (Figure 1.10(a)) was observed when a current density **J** was applied along the ab-plane of YBCO and the film was allowed to rotate with respect to the external magnetic field [Roas 1990]. Figure Fig. 1.10(b) shows the configuration of the sample vs B field, from which θ can be defined. When the flux lines are parallel to the ab-plane, the resulting Lorentz force will either push the flux

15

lines away or towards the film-substrate interface depending on the **J** direction, (Figure 1.10 (c)). However, this movement is prevented by the insulating layers of YBCO causing very strong pinning and thus resulting in a peak on the angular dependence of J_c when H is parallel to the ab-planes. Furthermore, the pinning is also very strong because the entire flux length is pinned.
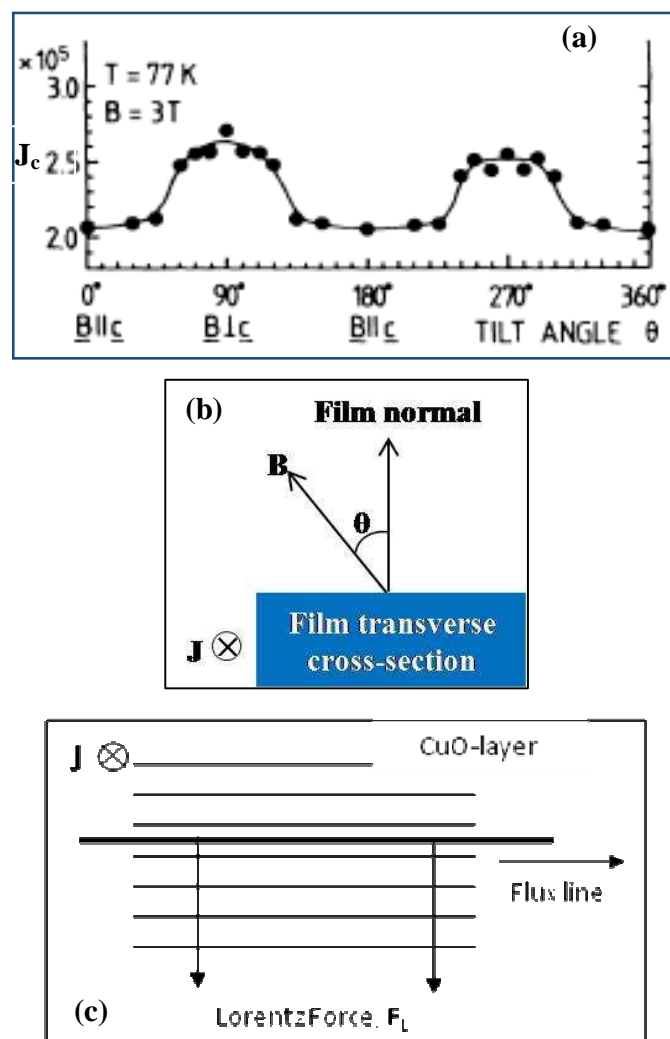
Figure 1.10 (a) Illustration of intrinsic pinning in YBCO films [Roas 1990]; (b) Configuration of the sample vs B field, from which θ can be defined; and (c) Direction of current, magnetic field and Lorentz force when H is parallel to the ab-plane.

1.5 Criteria for choosing appropriate pinning centers

Having discussed the structure, motion and pinning of magnetic vortices, we are now in the position of determining the most effective pinning centers in YBCO.

First, the coherence length in YBCO is very small compared to that of low temperature superconductors. This means the superconducting state is more susceptible to local disruptions from interfaces or defects on the order of a single unit cell, such as the boundary between twinned crystal domains or atomic defects such as oxygen vacancies and dislocations. Therefore, pinning centers with a size on the order of ξ would be enough to accomplish this task. At the same time, this is preferable since it will minimize the reduction in the superconducting volume portion.

Second, since the density of vortices increases with increasing field, the required field **B** for a given application will dictate the density of defects incorporated inside the YBCO. Thus the pinning center density should be equal to or comparable to the vortex density given by the equation: $B = \Phi_o / a^2$, where *a* is the distance between neighboring vortices.

Lastly, from the observation of intrinsic pinning, one can deduce that strong pinning sites can be created along the c-axis if the pinning centers can hold the entire flux length corresponding to columnar defects that traverse the whole film thickness. Also, to have a less anisotropic J_c-θ profile, pinning sites should be introduced at all angular orientations.

In Chapter 2, a summary of reported artificial pinning centers incorporated inside YBCO superconductors will be given and remaining issues will be presented.

The succeeding chapters will enumerate the studies performed in this work to provide

solutions to the identified issues.

Chapter 2

Artificial pinning landscapes in YBa$_2$Cu$_3$O$_{7-\delta}$ films

The application of YBa$_2$Cu$_3$O$_{7-\delta}$ (YBCO) in high temperature superconductor coated conductors (HTScc) has been a focus of rigorous research for the last decade. Aside from the fact that YBCO has a T$_c$ of ~90-92 K, it is also known for carrying a high critical current density (J$_c$), on the order of 10^4 A/cm^2 at 77 K and H=5 T. But in order for it to be applicable in various electrical power devices and systems, YBCO should satisfy the industry requirements summarized in Table 2.1 [Larbalestier 2001].

Table 2.1: Summary of requirements for device application of HTS.					
Application	J$_c$ (A cm^{-2})	Field (T)	Temperature (K)	I$_c$ (A)	Wire length (m)
Fault current limiter	10^4-10^5	0.1-3	20-77	10^3-10^4	1,000
Large motor	10^5	4-5	20-77	500	1,000
Generator	10^5	4-5	20-50	>1,000	1,000
SMES*	10^5	5-10	20-77	~10^4	1,000
Transmission Cable	10^4-10^5	<0.2	65-77	100 per strand	100
Transformer	10^5	0.1-0.5	65-77	10^2-10^3	1,000
*SMES, superconducting magnetic-energy storage. Data supplied by R. Blaugher.[Larbalestier 2001]					

The ultimate requirement for coated conductors is to fabricate tapes in kilometer lengths that can carry large currents on the order of a few hundreds to a thousand Amperes per centimeter width. Since typical YBCO thin films with thickness less than 0.3 μm have a J$_c$ of 4-5 MA/cm^2 at 77 K and zero applied magnetic field, the capability to carry large critical currents will require YBCO films of similar J$_c$ to have thicknesses of a few to several micrometers. Unfortunately, J$_c$

suffers a dramatic decrease with increasing YBCO film thickness whether on single crystal oxide or on bi-axially textured metal substrates [Luborsky 1988, Busch 1991, Foltyn 1993, Miura 1997, Foltyn 1999, Paranthaman 2000, Kang 2002 and Foltyn 2003], as illustrated in Figure 2.1 [Christen 2000]. Thus, an alternative way to increase I_c would be to increase J_c. This will be the ideal route since thinner films will be required to produce the required I_c and the processing time of HTScc's will be reduced.
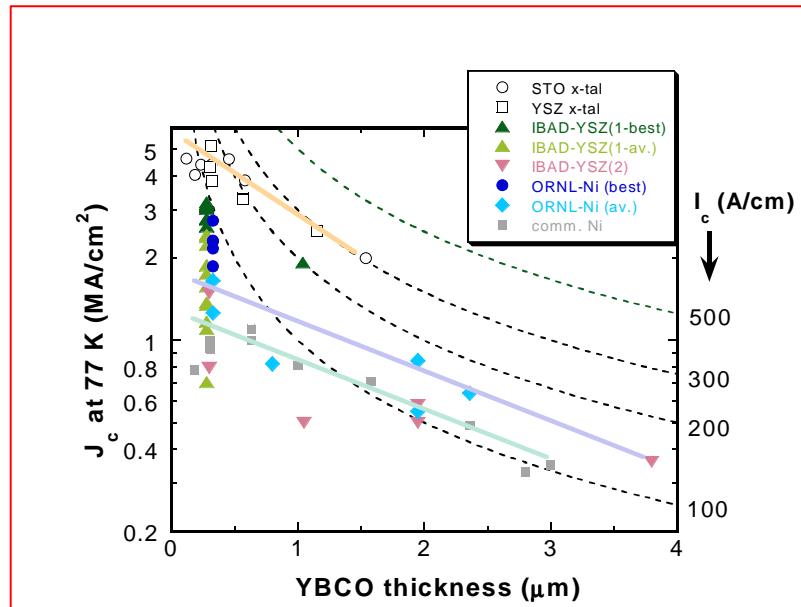
Figure 2.1 Thickness dependence of J_c in YBCO films deposited on single crystal substrates and bi-axially textured metal substrates. [Christen 2000]

Currently, high-quality un-doped YBCO thin films have self-field (SF) J_c's of around 4-5 MA/cm^2, which is only one-tenth of the depairing J_c. Furthermore, the J_c of YBCO typically drops by a factor of 10 from self field (SF) to an applied field of 1 T. In addition, the layered structure of YBCO is highly anisotropic and yields an

anisotropic transport property that is observable when J_c is plotted as a function of field orientation [Roas 1990]. Due to this anisotropy, the versatility of YBCO for applications in different field orientations is reduced. To address these issues, various artificial pinning centers (APCs) were generated inside the YBCO films. Interestingly, most of these APCs were modeled after the naturally occurring pinning sites inside the YBCO film, which is illustrated in Figure 2.2 [Foltyn 2007]. The artificial pinning sites that will be discussed in the next sections are: point defects in the form of nanoparticles and columnar defects generated by high-energy ion bombardment and self-assembling, vertically-aligned nanodots.
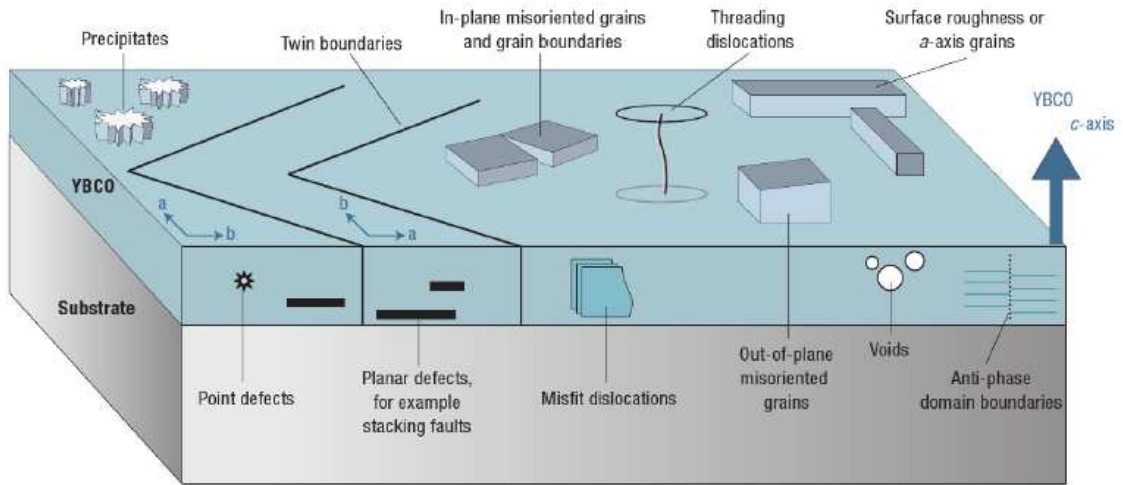
Figure 2.2 Illustration of the different naturally occurring pinning sites in YBCO films. [Foltyn 2007]

2.1 Nanoparticles

Nanometer-sized pinning centers are highly desirable in YBCO films since the size of the vortex core is on the same order of magnitude. Extremely small pinning centers will also minimize the reduction in the superconducting volume thus allowing

21

incorporation of defects with higher density. However, the density of native nanometer-sized point defects in YBCO films is only on the order of 10^9-10^{10} defects/cm^2 [Van der Beek 2002] and only corresponds to a matching field of 0.021-0.21 T. Thus, it is necessary to artificially incorporate nanoparticles in the YBCO film to enhance the matching field.

Haugan *et al* [Haugan 2004] incorporated second-phase Y$_2$BaCuO$_5$ (211) nanoparticles inside the YBCO film by alternating YBCO and 211 multilayers via a pulsed laser deposition (PLD) technique. The 211 layer can grow into islands of nanoparticles inside the YBCO lattice because of 211's large lattice mismatch of ~2-8% with YBCO. Figure 2.3(a) shows that the 211 nanoparticles with estimated areal density of >4x10^{11} particles/cm^2 were dispersed uniformly across the YBCO film. Furthermore, transmission electron microscopy (TEM) analysis showed that these nanoparticles grew randomly inside the YBCO matrix. A comparison of the field dependence of J$_c$ for a standard YBCO and YBCO/211 films is shown in Figure 2.3(b) and a significant improvement in J$_c$ at H > 0.5 T was observed for the YBCO/211 film. At a higher field of 1.5 T an increase in J$_c$ of >300% was achieved. This increase in high-field J$_c$ in the YBCO/211 film is attributed to the increased density of point defects in the YBCO film.
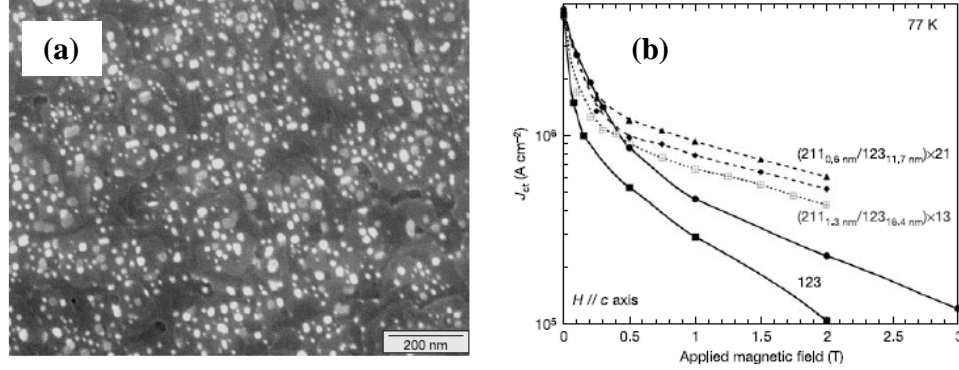
Figure 2.3 (a) SEM micrograph of a YBCO/211 film; (b) J_c-H comparison of YBCO and YBCO/211 films. [Haugan 2004]

Even though the density of point defects was remarkably increased in the YBCO/211 films, the defects are still randomly oriented leading to an un-optimized pinning force per unit length. Also, although significant improvement in J_c was observed at higher field, only a slight improvement was observed at low field. Lastly, no significant reduction in the J_c-θ anisotropy was realized.

2.2 Columnar defects

As shown in Chapter 1, columnar defects are considered to be the most effective pinning centers in YBCO. However, the only naturally occurring c-axis oriented linear defects in YBCO films are dislocations [Dam 1999] and measurements of the angular dependence of J_c for these films did not show a peak when the external field is applied parallel to the film's c-axis, suggesting that these dislocations are not strongly correlated columnar defects. Thus, the only route to introduce columnar defects in YBCO is through artificial methods.

2.2.1 Via heavy-ion irradiation

Columnar defects have been generated in YBCO single crystals by very-high-energy heavy ion irradiation [Civale 1991 and Krusin-Elbaum 1996]. Due to the ballistic motion of the high energy ions, columnar tracks of damaged YBCO were produced. The crystals were irradiated with 580 MeV Sn ions with the incident beam 2°, 30° and 45° away from the c-axis. The irradiation dosage was chosen to match the vortex density at fields of 1, 3 and 5 T. Electron micrographs of the columnar tracks are illustrated below in Figure 2.4(a). The columnar tracks consist of discontinuous columns with a diameter of ~50 Å and a separation of 100 Å. Figures 2.4(b) and (c) show J_c versus H for the crystals with different irradiation dosage at 5 K and 77 K, respectively, where H is parallel to the columnar defects and to the c-axis. Comparison with an un-irradiated crystal revealed that the irradiated crystal's J_c was greatly enhanced. Furthermore, it was observed that the J_c of Sn-irradiated crystals is monotonically increasing with dose suggesting that higher heavy-ion doses will further enhance J_c. Measurements of J_c when the flux line is aligned to or tilted away from the axis of the damaged tracks proved that the strong pinning is due to the alignment of the flux lines with the damaged columns. However, a reduction in the peak when H is in the ab-plane was observed due to an alignment effect.
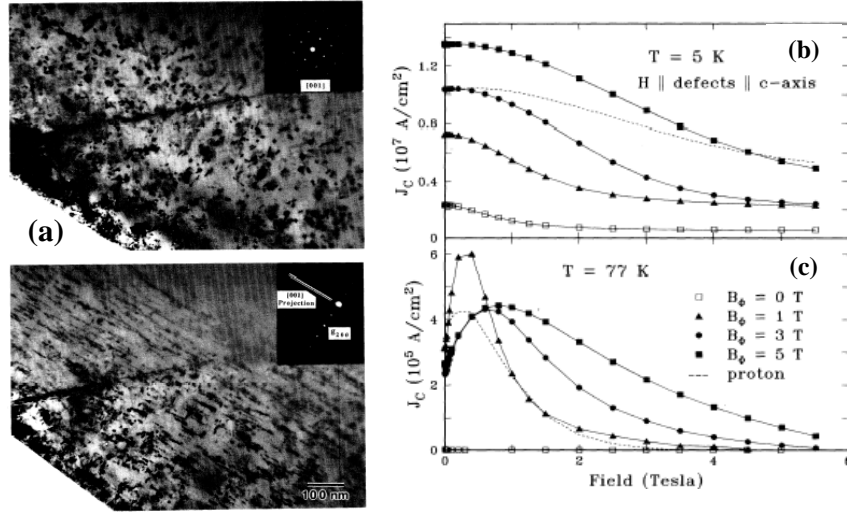
Figure 2.4 (a) TEM cross-section of the ion-irradiated YBCO crystal; J_c-H comparison of ion-irradiated YBCO crystals with different ion dose at (b) 5 K and (c) 77 K. [Civale 1991]

Although these linear defects have been proven to be the most effective pinning centers in YBCO, this method is not practical for scale-up because it is too expensive and it can render the metallic substrate radioactive. Thus, it is necessary to create columnar defects in YBCO via growth. In the next subsection, recent advances in doping YBCO films with columnar defects are discussed.

2.2.2 Via growth

a. BaZrO₃ (BZO) nanorods insertion

One of the most recent studies focuses on doping YBCO with BZO nanoparticles [Driscoll 2004, Yamada 2005, Goyal 2005, Kang 2006, Peurla 2006, Peurla 2007, Pompeo 2008, Mele 2008]. Because BZO has a large lattice mismatch with YBCO, it has been observed that the BZO nanoparticles developed into nanorod structures inside the YBCO film and grew parallel to the normal to the film surface. A

25

TEM micrograph (Figure 2.5(a)) shows that the BZO nanodots are aligned along the crystallographic c-direction in YBCO and have a diameter ~2–3 nm and a separation distance of ~15 nm. Also, it was observed that the areal density of the BZO nanorods is on the order of 10^{11}-10^{12}/cm^2, which corresponds to a matching field of 8-10 T. The J_c-H plot in Figure 2.5(b) shows that the J_c is enhanced over the full field range. Also, the slope of the linear part of the J_c-H plot, α, was reduced to 0.3. Consequently the $J_{c,SF}$ to $J_{c,5T}$ ratio is about 15-20, which is a factor of 4 lower than the un-doped YBCO film. The observed peak in the J_c-θ plot when H is along the c-axis (Figure 2.b(c)) demonstrates that the enhancement in J_c is caused by the correlated pinning of the BZO nanorods.   Furthermore, comparison of J_c-θ between YBCO/BZO and YBCO/211 films revealed that both have a H||ab peak but the latter has no H||c-axis peak proving that the former has more superior pinning. This further emphasizes that columnar defects are stronger pinning centers than point defects.
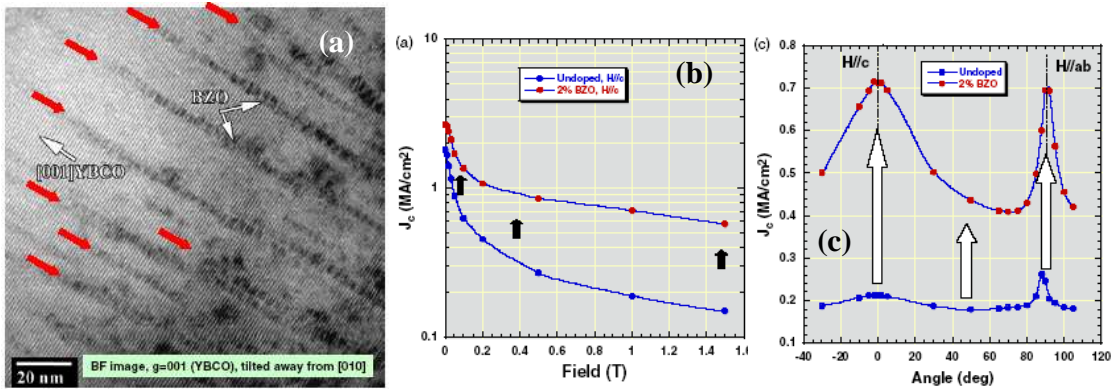
Figure 2.5 (a) TEM micrograph of YBCO/BZO film showing c-axis alignment of the BZO nanorods; (b) J_c-H comparison of YBCO and YBCO/BZO film; and (c) J_c-θ comparison of YBCO and YBCO/BZO film at 1 T and 77 K. [Goyal 2005]

26

Although a remarkable increase in in-field J_c has been observed in the YBCO/BZO film, its self-field J_c is not improved as compared to an optimized flat YBCO film. Furthermore, the T_c is significantly reduced in these films.

b. BaSnO₃ (BSO) nanorods insertion

BSO nanorods in YBCO films have been observed to have better in-field performance than the BZO nanorods. [Varanasi 2008(a), Varanasi 2008(b) and Mele 2008]. Also, insertion of BSO, which has a smaller lattice mismatch of ~6.6% with YBCO, did not diminish the T_c of YBCO as much as BZO insertion did [Mele 2008]. The T_c values are 87.74 K for the BZO-doped sample and 88.57 K for the BSO-doped sample. TEM cross-sections of the BZO-doped and BSO-doped YBCO films are shown in Figure 2.6(a). The BZO nanorods became heavily curved with increasing film thickness. However, the BSO nanorods grew almost parallel to the *c*-axis direction of the film. Since the nanorods work as c-axis correlated pinning centers, the length of the straight portion is very important to obtaining a large pinning force when B is applied parallel to the c-axis. From TEM cross-sectional images, the effective length (which is the ratio between the length of the straight part of the nanorod and the film thickness) of the BZO nanorods is 78.2 nm while that of the BSO nanorod is 139.4 nm. The effective length of the BSO-doped film is twice that of the BZO-doped film. As a result, a much more improved pinning along the c-axis was observed on the former film as depicted in the much higher J_c-θ peak when H is along the c-axis in the BSO-doped YBCO film (Figure 2.6(b)).

27
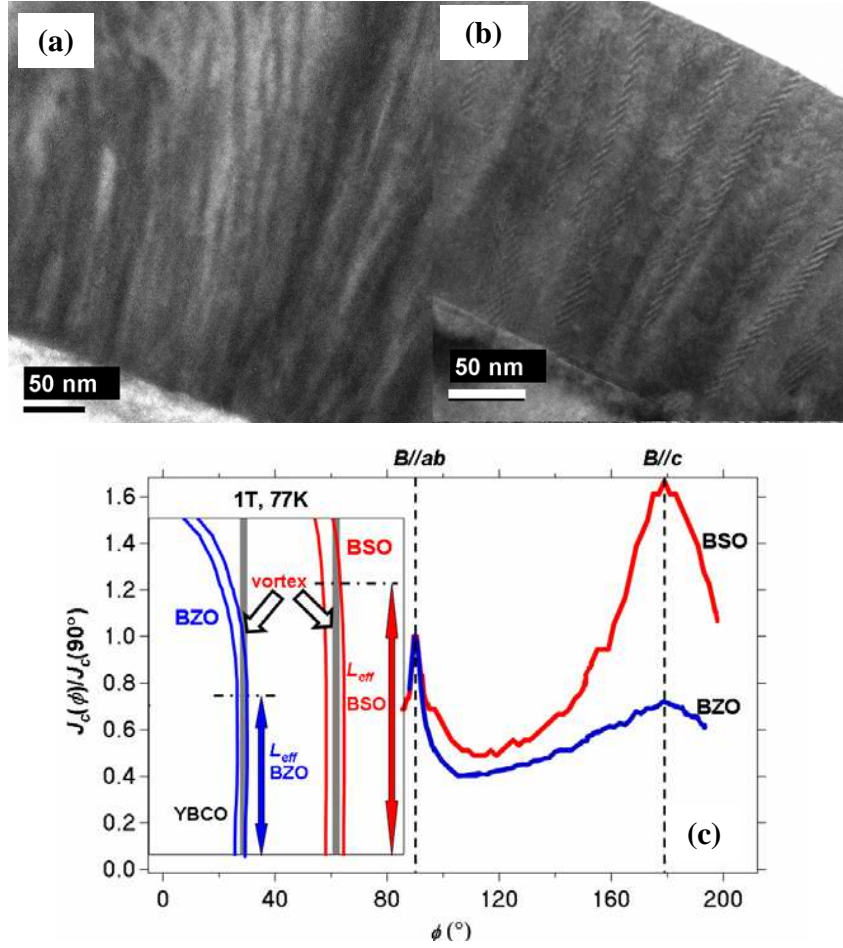
Figure 2.6 TEM micrograph of (a) BZO-doped YBCO film and (b) BSO-doped YBCO film; (c) J_c-θ comparison of YBCO/BZO and YBCO/BSO films at 1 T and 77 K. The inset illustrates the effective length of the BZO and BSO nanorods. [Mele 2008]

c. Rare-earth Tantalite (RTO) insertion

RTO nanorods are the most recent self-assembled columnar defects incorporated in YBCO films [Harrington 2009]. YBCO films containing RTO, with lattice mismatch ranging from 1.4-4.7%, did not suffer any T_c degradation even for RTO concentrations up to 8 mol.% . The TEM cross-section in Figure 2.7(a) shows the c-axis aligned RTO nanorods. The rods are highly linear and extend through the

28

whole film thickness. The RTO nanorods are ~5 nm wide, comparable to the width of BZO and BSO nanorods, and the density corresponds to a matching field of ~3.8 T. A comparison of the field dependence of J_c for three different types of RTO-doped YBCO films and an un-doped YBCO film is shown in Figure 2.7(b). The film thickness is ~0.5 µm. Significant improvement in the J_c, particularly at high field, was observed in the RTO-doped YBCO films. The J_c in the RTO-doped YBCO film is far superior to that of the BZO-doped YBCO film (Figures 2.7(c) and (d)) over all field orientations of the RTO-doped YBCO film.
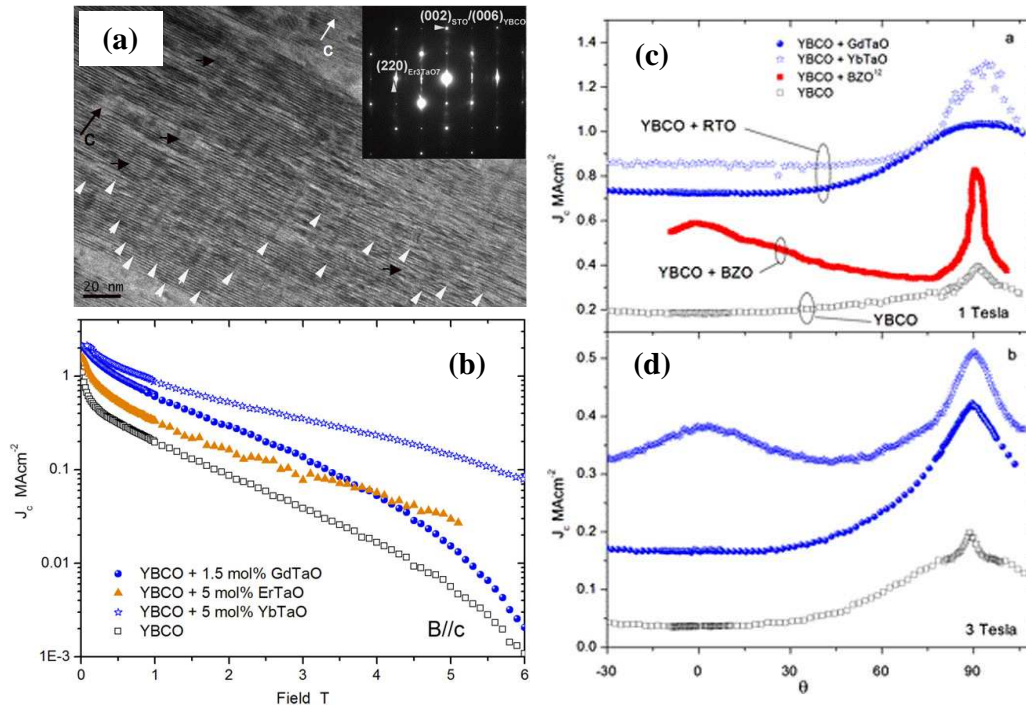
Figure 2.7 (a) TEM cross-section of an RTO-doped YBCO film; (b) J_c-H plot of three different kinds of RTO-doped YBCO film and an un-doped YBCO film; Comparison of J_c-θ plots for the RTO-doped YBCO films, BZO-doped YBCO films and un-doped YBCO film at (c) 1 T and (d) 3 T. [Harrington 2009]

However, even though an improved J_c was observed at all the field strengths, it is important to note that the J_c at SF in the un-doped YBCO film is far lower than the reported J_c values in optimized un-doped YBCO film of the same thickness (0.5 μm) [Wang 2008].

2.3 Remaining Issues

Although significantly enhanced in-field J_c was achieved in YBCO films containing artificially incorporated pinning centers, few of them reported significant enhancement of J_c at self and low field. This is unfortunate because high J_c at low field is necessary for device applications such as transmission cables [Larbalestier 2001].

Since the pinning force is defined as the gradient of the energy of a vortex as a function of position, it follows that the strength of a pinning center is determined by the gradient of the order parameter between the superconducting and normal region, $F_P \propto \dfrac{\partial U_P}{\partial r} \propto \dfrac{\partial \psi(r)}{\partial r}$. This suggests that maximum pinning can be achieved if the inhomogeneity inside the YBCO film is a void. In Chapters 4 and 5, we show how the nanotube pores generated inside the YBCO film doubled the J_c value at self field as compared to that in optimized un-doped YBCO films.

Furthermore, since almost all of the reported nanometer-sized columnar defects are aligned nearly perfectly along the c-axis, the in-field J_c is not much improved or even reduced at field orientations deviating from the c-axis. This is unfortunate for many applications of YBCO coated conductors, such as motors and

generators, wherein the generated strong magnetic field may bend or twist causing the vortices to stray from the correlated pins. Broadening or splaying the orientation of columnar defects in YBCO films may provide an effective solution to this problem. In Chapters 6 and 7, we show that a simple process of depositing BZO-doped YBCO films on vicinal substrates leads to enhanced J_c at all field range and orientation.

Lastly, the electronic properties of the RTO-doped YBCO films suggest that a large improvement in J_c can be achieved in YBCO films if the degradation in T_c and self field J_c caused by lattice strain and lattice contamination during insertion of nanorods can be eliminated. In this study, we also show that by employing vicinal growth, the degradation in T_c was significantly reduced. In addition, the lattice contamination was also retarded. This allowed insertion of BZO-NRs in a higher concentration leading to record high J_c values.

Chapter 3

Experimental Techniques

3.1 Fabrication of doped and un-doped YBCO films

All YBCO films studied in this work were fabricated using a pulsed laser deposition (PLD) technique. In this method, which is illustrated in Figure 3.1, a focused high energy UV laser beam, with dimension of 1.5 mm x 3 mm, is used to ablate a very thin layer of the target material. Afterwards, the ablated material, which is contained inside the plume, is deposited on a chosen substrate mounted on a heater block. Deposition is done inside a high vacuum chamber and the target material is rotated to ensure uniform ablation over the target surface. The deposition conditions were optimized for the flat YBCO film at a deposition temperature of 790 ℃, substrate-to-target distance of 5.5 cm, O_2 partial pressure of 300 millitorr, deposition rate of 13-15 nm/min and annealed at 500 ℃ with 1 atm O_2.[Haugan 2003]
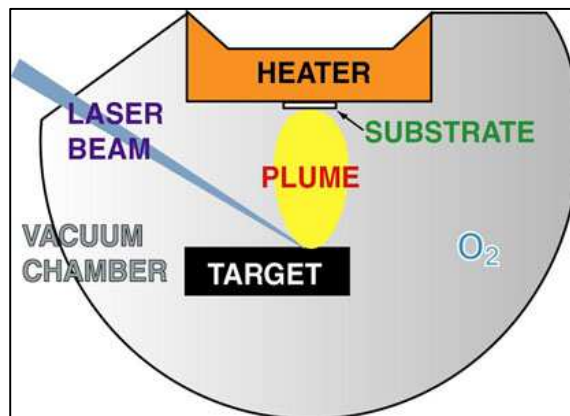
Figure 3.1 Illustration of a pulsed laser deposition system.

32

YBCO films were doped with nanotube pores by depositing the latter on as-received commercial vicinal SrTiO$_3$ (STO) substrates. A schematic diagram of a vicinal substrate is shown in Figure 3.2. The vicinal substrate is formed when the latter is cut in such a way that its c-axis is oriented a few degrees away from its normal. As a result, the vicinal substrate shows a step-like surface morphology. When YBCO is deposited on the vicinal substrate, the growth mode of the latter switches from island-type to step-flow-type [Lowndes 1992]. Consequently, the YBCO film's microstructure becomes anisotropic in the plane of the substrate. The direction parallel to the surface steps is denoted as the longitudinal direction, whereas the perpendicular, the transverse direction. The vicinal angles employed in this study are flat=0°, 5°, 10° and 20°.
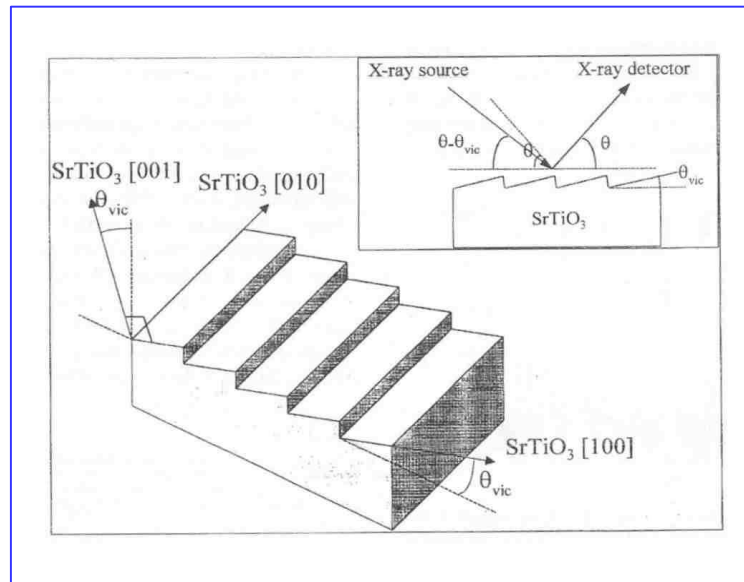
Figure 3.2 Schematic diagram of a vicinal STO substrate.
[Mechin 1998]

Splayed BaZrO$_3$ (BZO) nanorods were incorporated inside the YBCO film by depositing BZO-doped YBCO on vicinal STO substrates. The BZO concentrations used for this study are: 2 vol.%, 4 vol.% and 6 vol.%.

3.2 Characterization of surface morphology

The surface morphologies of the films studied here were investigated using a JEOL scanning electron microscope (SEM) and Veeco atomic force microscope (AFM). In an SEM, a sample is imaged by using a rastered high-energy beam of electrons. Figure 3.3 illustrates the schematic of a typical SEM. The electrons produced by the electron gun are attracted to the anode and accelerated towards the sample stage. On its way down, the electron beam is collimated by a condenser lens and then focused by an objective lens. Scanning coils are used to raster the electron beam across the sample surface. When the electron beam collides with the sample surface, electrons are emitted off the latter and the emitted electrons are collected by an appropriate detector and fed into a cathode ray tube [Goldstein 2003].
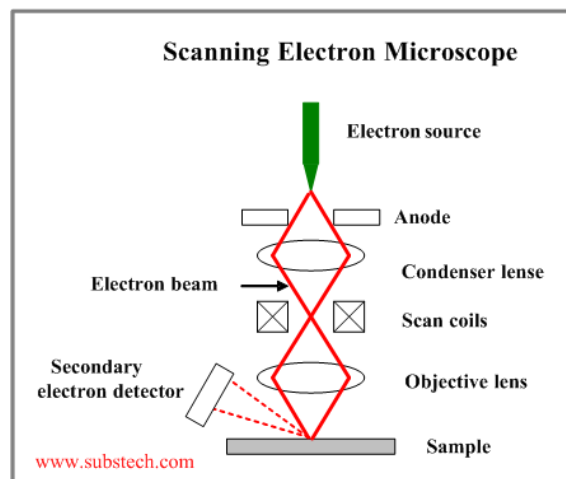
Figure 3.3 Schematic diagram of a scanning electron microscope. [www.substech.com]

On the other hand, the AFM employs a microscale cantilever with a sharp tip at the end to scan the sample surface. This is illustrated in Figure 3.4. The sample is mounted on a stage controlled by piezoelectronic elements that facilitate tiny but accurate and precise movements, which enable the very precise scanning of the sample's surface. The interaction between the tip and the sample surface causes the cantilever to deflect. This deflection is typically measured by using a laser spot reflected from the top surface of the cantilever into an array of photodiodes [Cohen 2008].
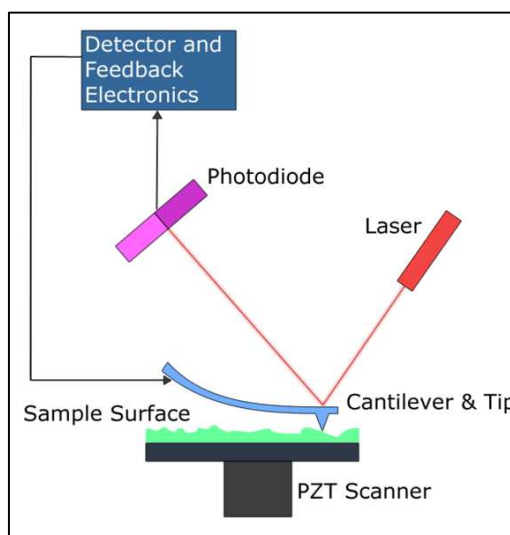
Figure 3.4 Schematic diagram of an atomic force microscope. [http://en.wikipedia.org]

3.3 Characterization of crystalline structure

The crystalline structure and phase purity of the films were investigated by using a Bruker D8 x-ray diffraction (XRD) system. Diffraction occurs when x-rays incident upon a sample are scattered by the atoms in the latter and undergo constructive interference in accordance to Bragg's law ($n\lambda = 2d\sin\theta$). A diffraction

pattern is obtained by measuring the intensity of scattered waves as a function of scattering angle. Very strong intensities known as Bragg peaks are obtained in the diffraction pattern when scattered waves satisfy the Bragg condition [Warren 1990 and Kittel 1995]. A typical illustration of an XRD system is depicted in Figure 3.5. It is composed of an x-ray source, detector and sample stage mounted on a goniometer. The crystalline orientation is determined by doing a θ-2θ scan. Rocking curves or ω-scans are used to determine the out-of-plane alignment of thin films. This is achieved by setting the x-ray source to θ (which corresponds to a certain d-spacing) and allowing the detector to graze at a certain range of ω angles. The full-width-at-half-maximum (FWHM) of the peak is then measured. On the other hand, a φ-scan is employed to determine the in-plane alignment of the films. A pole figure (acquired from Oakridge National Laboratory) is measured at a fixed scattering angle (constant d spacing) and consists of a series of φ-scans (in-plane rotation around the center of the sample) at different tilt or χ (azimuth) angles.
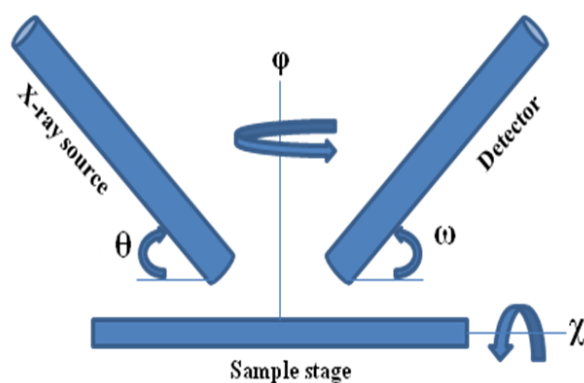
Figure 3.5 Schematic diagram of an x-ray diffraction system.

For the case of the vicinal films, the following steps were done to determine the crystalline integrity. First, the θ and 2θ were set to the angles corresponding to the (005) peak of YBCO. Then the χ was set to the vicinal angle of the substrate and a φ-scan was performed. The peak of the φ-scan corresponds to the orientation where the surface steps are parallel to the plane of the source and detector. After the proper orientation of the planes was determined, the χ angle was optimized. Finally, the θ-2θ and rocking curves of the (005) peak were obtained for the vicinal films. The in-plane alignment was determined by first setting the θ, 2θ and χ angles to the angles corresponding to the (103) planes (which are 16°, 32° and 45°+~θ_v, respectively) and then φ-scans were done. The FWHM of the peaks in the φ-scans were then measured.

3.4 Microstructure characterization

To study the cross-section of the films in this work, transmission electron microscopy (TEM) was done in the Air Force Research laboratory. Cross-sections were prepared using a FEI Nova 600 NanoLab and DB235 focused ion beam systems. Care was taken to cut the cross-sectional foils perpendicular to the vicinal steps, so that the effects of the modulated surface could be directly observed. The microstructures of the films were studied using a Philips CM200 and FEI Titan TEM operating at 200 kV and 300 kV, respectively [Baca 2009].

3.5 Fabrication of YBCO microbridges and contact pads

A standard photolithography technique, which is illustrated in Figure 3.6(a), was employed to fabricate microbridges on the films studied in this work. Due to the anisotropic nature of the vicinal films, two perpendicular bridges with dimensions of

37

20 µm x 500 µm were patterned on the films; one bridge is parallel to the surface steps (longitudinal) while the other perpendicular to the steps (transverse). The film was spin-coated with an S1813 positive photoresist with thickness of approximately 1.3 µm for 60 seconds at ~4000 rpm. The film was then baked at 90 °C for 5 minutes. Afterwards, the film was exposed to UV light for ~30 seconds using a Karl-Suss Mask Aligner and then developed in a 1:3 solution of microposit developer and deionized water. The exposed film was etched using 0.05% nitric acid and the remaining photoresist was rinsed off using acetone. Silver contact pads were deposited on the films by using DC sputtering. The final circuit is illustrated in Figure 3.6(b).
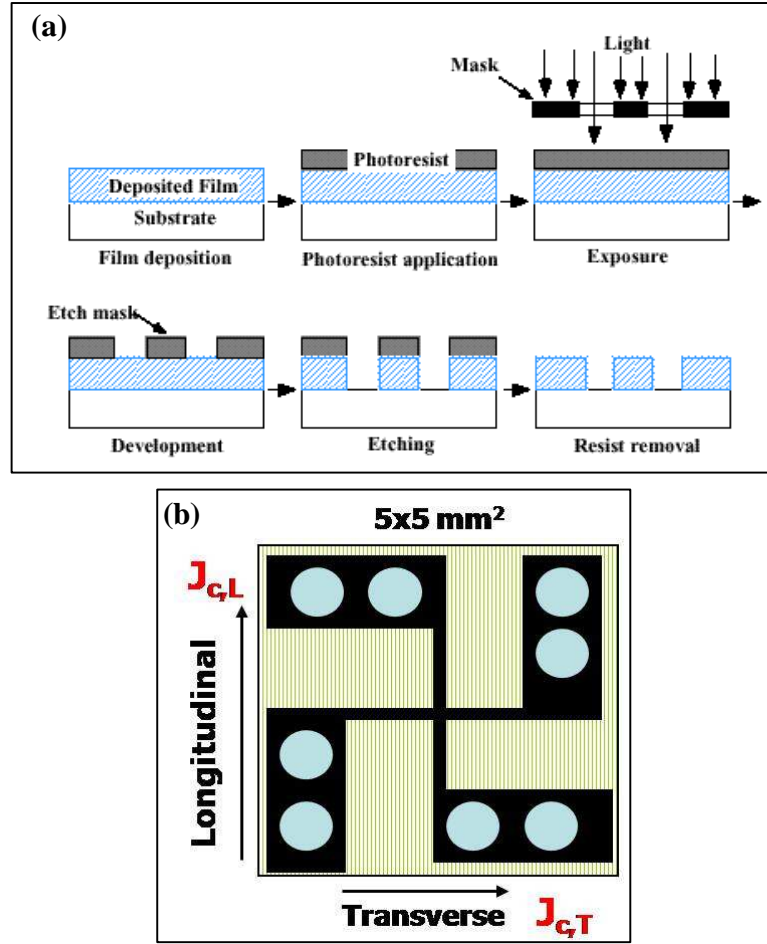
Figure 3.6 Illustration of (a) the photolithography procedure [www.hitequest.com] and (b) final circuit with contact pads.

3.6 Characterization of electronic properties

After patterning, gold wires are attached to the contact pads using indium. The film is then mounted on the probe stage using a low temperature Apiezon N grease and the gold wires are soldered to the contact posts. The stage can be rotated to a maximum of 120° clockwise and 120° counter-clockwise. Transport measurements were done using the standard four-point probe technique in an 8 T-superconducting magnet. The resistance versus temperature and J_c as function of applied magnetic

39

field strength (J_c-H) and orientation (J_c-θ) were measured. For the J_c-θ measurements, the samples were mounted in such a way that the field was always in the maximum Lorentz force configuration. An illustration is shown in Figure 3.7. J_c was determined by applying the 1μV/cm criterion. A Keithley 2430 Pulsed-Current source with pulse width of 500 ms was employed for I-V measurements for minimal Joule heating. A Lakeshore 330 temperature controller and an HP 34420A nanovoltmeter were used in these measurements.
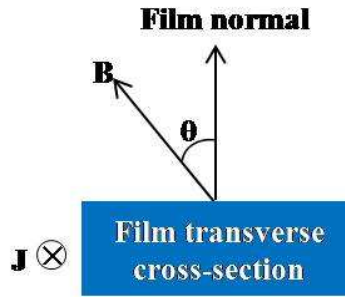
Figure 3.7 Schematic of J_c-θ measurement.

3.7 Magneto-optical imaging

Magneto-optical (MO) characterization was performed in the Applied Physics Laboratory at the University of Wisconsin using a Bi-doped magneto-optical garnet film with in-plane magnetization grown on gadolinium gallium garnet substrates [Polyanskii 1999 and 2003]. The sample was mounted on a cold finger of a continuous flow optical cryostat capable of cooling to ~6 K located on an X-Y stage of a polarized optical microscope in reflective mode. A silicone heat sink compound created a tight temperature contact between the bottom face of the sample and the cold finger. To register the normal component of the magnetic flux distribution H_z on

the sample surface the indicator film was placed on the top sample face without any restraint. A silicon diode and the LakeShore temperature controller adjusted the sample temperature. The external magnetic field was applied perpendicular to the film plane by a small solenoid surrounding the cold finger [Polyanskii 1999 and 2003]. A digital camera was used to record the magneto-optical images. A deconvolution procedure [Perkins 2002] and depth measurements of the flux penetration into films [Brandt 1993 and Polyanskii 1996] were used to calculate the J_c distribution and its anisotropy in flat and vicinal samples.

Chapter 4

Enhancing self field and low field J_c via nanotube pore pinning

High J_c at applied magnetic fields <0.2 T is necessary for the application of YBCO films in electrical devices such as transmissions cables. This can be accomplished by doping YBCO films with low density (<97 pins/μm^2), strong pinning centers. From the discussion in Chapter 2, the immobilization of magnetic vortices would be optimum if the change in the order parameter between the superconducting phases and surrounding pinning centers is abrupt and enormous. In other words, strong pinning can be achieved if voids or pores are utilized as pinning centers. Furthermore, since columnar defects have been observed as the most efficient pinning center, it is most favorable that the voids are columnar or tube-like. Also, the dimensions of these columnar voids should be on the order of a few to a hundred nanometers since the size of the vortex core is on the same order of magnitude. Columnar voids on the order of a few microns will significantly reduce the superconducting volume. However, it is difficult to generate nanotube pores in YBCO films and it is especially challenging to control the pore size and density.

In this chapter, we report enhanced J_c values up to 8.3 MA/cm^2 at 77 K and SF in YBCO films by doping nanotube pores of low density on the order of several pores/μm^2. The process we have developed for fabrication of these porous YBCO

films has two important components: nanoparticle generation and substrate miscut, both are used for controlling mechanical strain on the YBCO lattice at nanoscale.

4.1 Surface morphology, cross-section and crystalline structure of porous vicinal YBCO films

Figures 4.1(a) to 4.1(d), taken by SEM, illustrate the surface morphology of 0.2 µm thick YBCO films deposited on flat, 5°, 10º and 20º vicinal STO substrates. It is noticeable that the surface morphology of the vicinal films is highly porous while the flat film's surface morphology is smooth and dense. The vicinal angle of the STO substrate does not seem to affect the pore density significantly in the angle range of 5º-20º, while the morphology of the pores experiences a systematic change with increasing vicinal angle. At smaller vicinal angles, the pores are more isotropic while at larger ones, they seem to be squeezed along the transverse direction (perpendicular to the surface steps) and become considerably anisotropic. The pore density of the porous vicinal films is 5 ± 3 pores/μm^2 and the pores' dimensions are in the range of a few to a few hundreds of nm when the θ_v (angle between the film normal and the c-axis) is in the range of 5-20°.
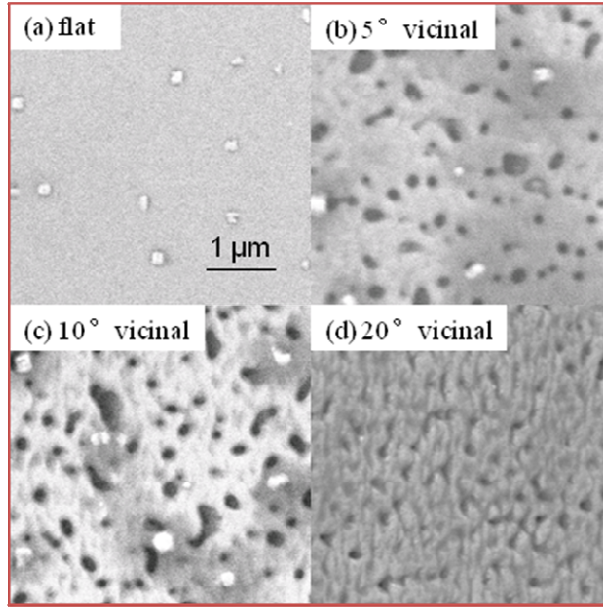
Figure 4.1 SEM pictures of 0.2 µm thick YBCO films deposited on STO substrates with different vicinal angles: (a) flat, (b) 5º, (c) 10º and (d) 20º. [Wu 2008]

It should be mentioned that on vicinal substrates, most pores run through the entire or a large portion of the film thickness up to a few micrometers. This is revealed by the TEM cross-section of a 1 µm-thick porous YBCO film on a 15º vicinal STO substrate depicted in Figure 4.2. It is noticeable that the pores seem to initiate near or at the substrate-film interface. The inset of Figure 4.2 shows the TEM image of the film/substrate interface of the same film. Surface steps, on which anti-phase boundaries (APBs) initiate, can be clearly visualized. The step width is in the range of 3-5 nm and the step height is comparable to the c-axis lattice constant of YBCO. It is also shown that the ab-planes of these porous vicinal films are tilted from the film-substrate interface by $\sim\theta_v$ and the film-substrate interface is mostly filled with defects

such as stacking faults. Although the interface is highly defective, the YBCO lattice looks nearly perfect above ~5-10 nm from the interface after the appearance of stacking faults. This means that the lattice strain due to vicinal growth may initiate at or near this thickness.
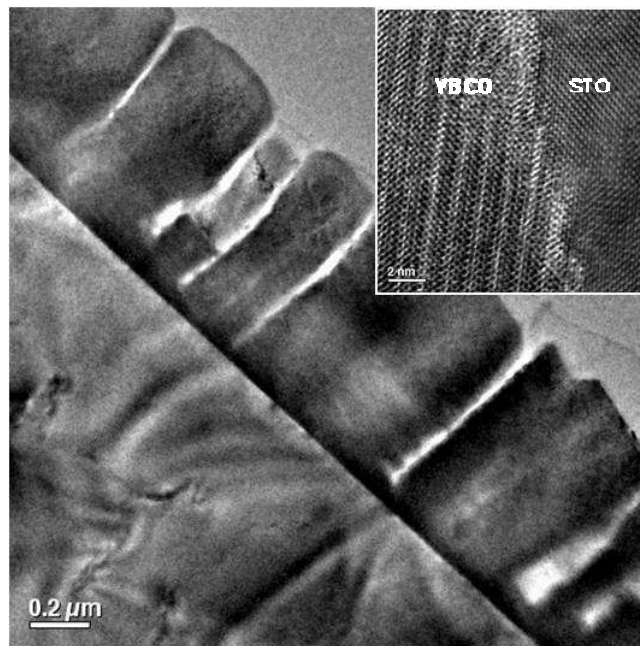
Figure 4.2 TEM cross-section of a 1.0 μm thick YBCO film deposited on 15° vicinal STO substrate. Its inset shows a TEM image of the film/substrate interface of the same film. [Wu 2008]

The YBCO films grown on vicinal STO substrates are c-axis oriented as confirmed in XRD θ-2θ scans. In addition, no other impurity phases were visible from the XRD spectra. The c-axis of the vicinal YBCO films is tilted away from the normal by an angle close to the miscut angle of the substrates. Figure 4.3 depicts an XRD (005) pole figure of a 2.0 μm thick YBCO film on a 10° miscut STO substrate. The split center pole is because of detector saturation and the extra four poles are due

to the YBCO (104) reflections having the same d-spacing as (005). The tilt angle of ~11.0° is clearly shown. This indicates that the YBCO films grew epitaxially under the influence of the miscut substrate. The epitaxial growth of the film is evidenced from the four clear poles.
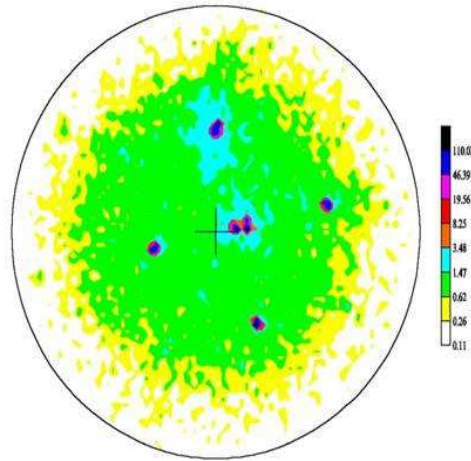
Figure 4.3 XRD (005) pole figure of a 2.0 µm thick YBCO film on 10º vicinal STO substrate. [Emergo 2004]

4.2 Nucleation and evolution of nanopores

To understand the mechanism of the nucleation of nanopores, very thin YBCO layers were grown on top of vicinal STO substrates. Figure 4.4(a) shows the AFM image of an 8 nm-thick 20° vicinal YBCO film. Nanoparticles (NP) with density of ~9.3×10^7/cm^2 were observed on the surface of this film. However, the density of NP's was reduced to ~3.4×10^7/cm^2 when the film thickness was increased to 16 nm, as shown in Figure 4.4(b). An AFM scan of this film at higher magnification, as illustrated in Figure 4.4(c), shows the presence of nanopores. A closer inspection of a nanopore reveals the presence of a nanoparticle at the bottom of the nanopore (Figure

46

4.4(d)). Indeed, a line scan of the same nanopore confirms the existence of a hump on its base. Interestingly, the density of these nanopores corresponds closely to the difference between the density of nanoparticles in the 8 nm and 16 nm thick films. This strongly suggests that the NP's seem to catalyze the nucleation of nanopores. As a matter of fact, a TEM cross-section of a nanopore, illustrated in Figures 4.5(a) to (c), reveals a nanoparticle underneath the nanopore (Figure 4.5(b)). Chemical analysis revealed that the nanoparticle is composed of Y_2O_3 (Figure 4.5(c)).
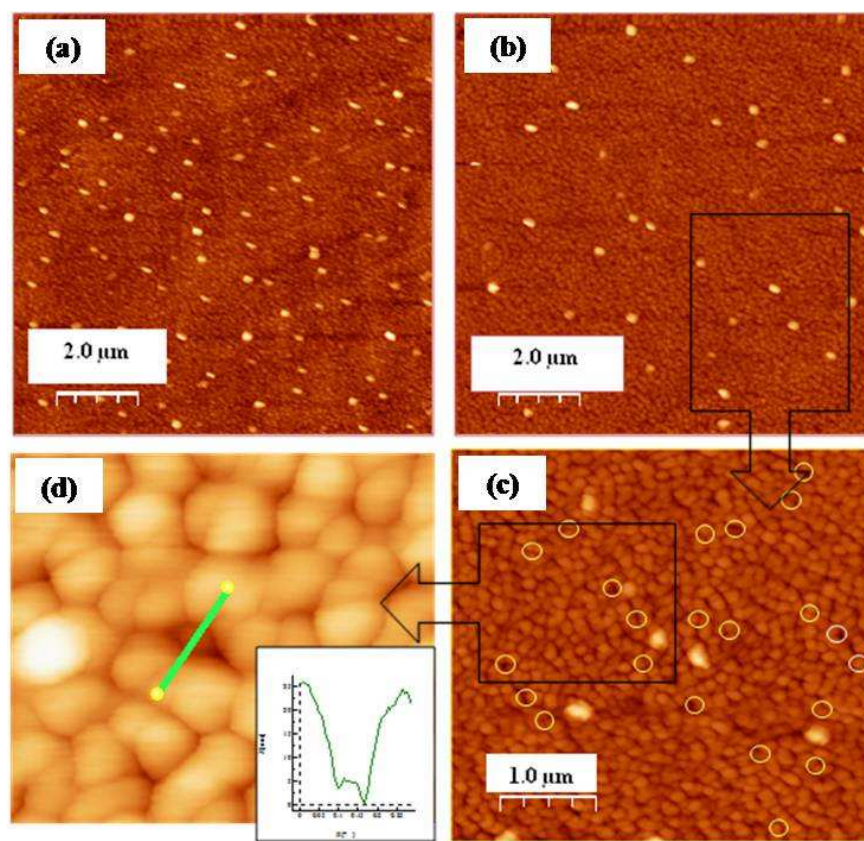
Figure 4.4 AFM images of (a) 8 nm-thick and (b) 16 nm-thick YBCO films deposited on 20° vicinal STO substrate, respectively. The nanopores just initiated atop NPs are circled on (c); (d) AFM image of a selected pore and the inset shows the depth profile. The x-direction in the inset is the scan direction defined by the green line in (d). A NP at the bottom of the pore can be clearly seen. [Data taken by Guowei Xu.]

47
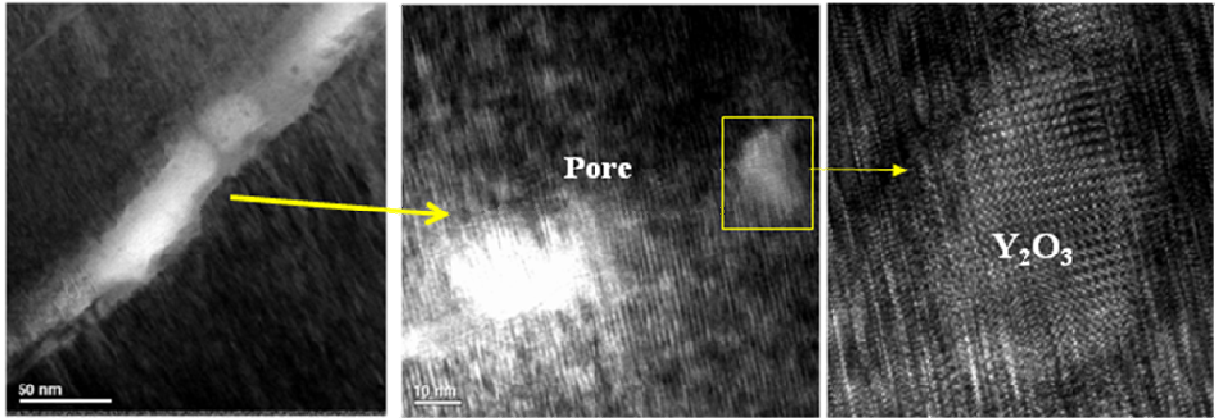
Figure 4.5 (a) TEM cross-section of a nanopore; (b) TEM image of the base of a nanopore showing a nanoparticle underneath; (c) higher resolution image of the nanoparticle. [Data taken by Dr. Hong Hui Chou.]

Interestingly, YBCO films grown on flat LAO substrates with a buffer layer of Y_2O_3 nanoparticles also exhibited a porous microstructure. However, the pores in these films were annihilated at film thicknesses greater than 0.45 µm, which is contrary to the nanopores in vicinal films that persist up to a film thickness of 3 µm. This suggests that the strained lattice in vicinal YBCO films plays a vital role in the evolution of the pores through large thickness.

4.3 Comparison of critical current density and pinning force density between dense and porous YBCO films

Figure 4.6(a) compares the longitudinal J_c at 77 K of three porous YBCO films and a reference YBCO film as a function of magnetic field (H) on a log-log scale. The H field was applied along the normal of the film. It is clearly seen that all of the porous YBCO films carry significantly higher J_c values than their reference counterpart in SF and low H fields. The SF J_c values of these three films are in the range of 8.0-8.3 MA/cm^2, which is significantly higher than that of the reference

48

YBCO film. Notice that the flat YBCO film's J_c of ~4.0 MA/cm^2 is within the range of J_c values obtained from optimized standard YBCO films without impurity doping [Foltyn 2007]. A similar trend was also observed at other temperatures and the longitudinal J_c comparison of the same four samples at 65 K is shown in Figure 4.6(b). The SF J_c values in the range of 15.2-17.5 MA/cm^2 were obtained on porous YBCO films as opposed to 7.8-8.5 MA/cm^2 for the reference samples.
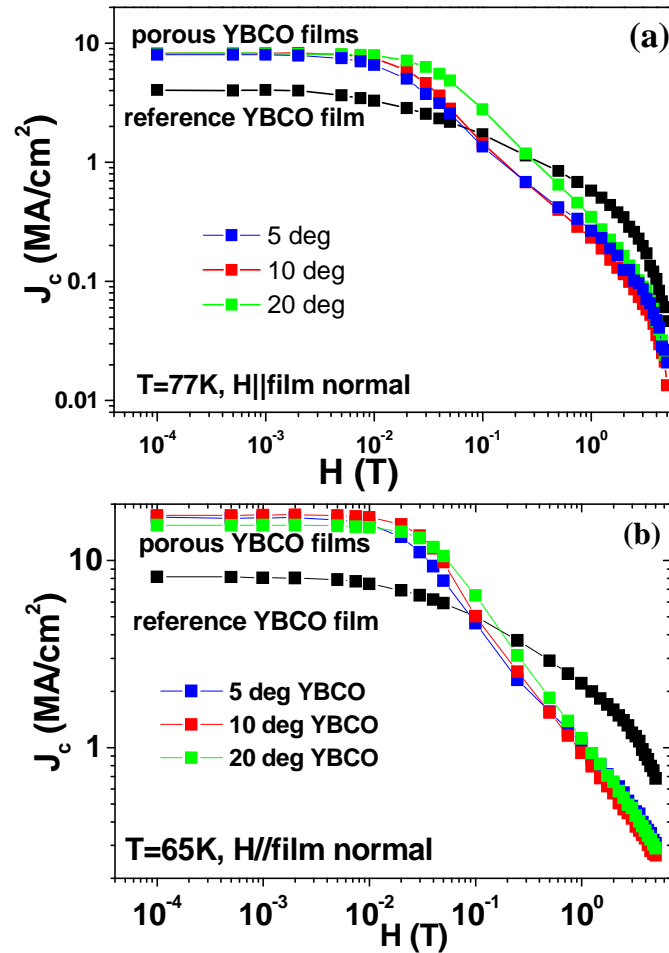
Figure 4.6 Comparison of the longitudinal J_c values of a reference and three porous vicinal YBCO films with H||film normal at (a) 77 K and (b) 65 K. All samples have thickness of 0.2 µm. [Wu 2008]

We argue that the significant increase in $J_{c,L}$ of these vicinal samples is due to the strong magnetic pinning provided by the nanotube pores. The pinning potential of the nanopore surface can be approximated from the N value derived from the relation $V \propto I^N$ for the flux creep [Tahara 1991 and Blatter 1994]. Since the N value is proportional to the pinning potential and the latter is proportional to J_c, a correlation between the J_c and N value is expected. Indeed, in low field up to H~0.01 T, the J_c values were found to follow the trend of the N value as shown in Figure 4.7(a). Furthermore, the N value and J_c of the porous vicinal films follow the same field dependence up to H~0.05 T as shown for the 20º sample in Figure 4.7(b). However, the N value and J_c diverge from each other above H~0.05 T. While other reasons may exist, the lower accuracy in approximating the N value may be a dominant reason at higher H due to the more broadened I-V curve as shown in the inset of Figure 4.7(b).
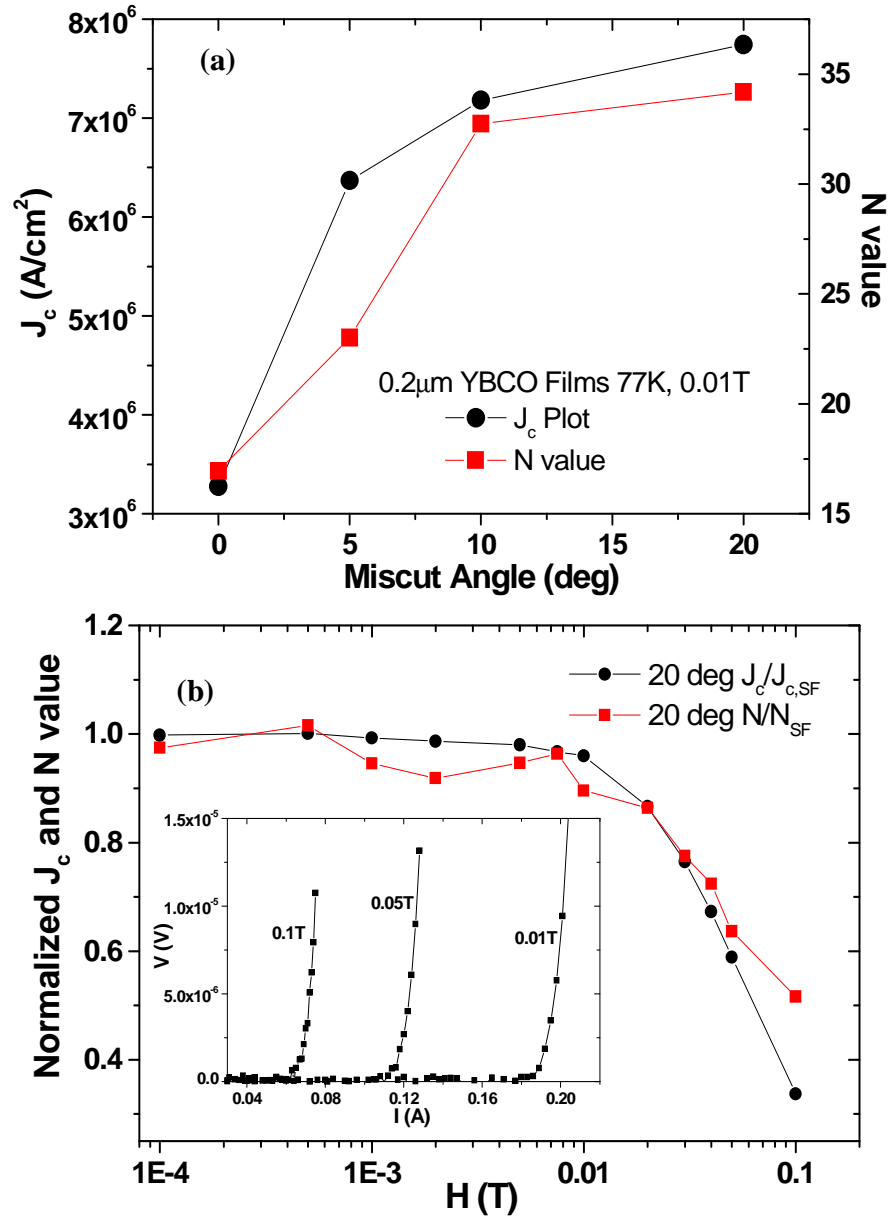
Figure 4.7 (a) Comparison of the J_c and N values of the four samples shown in Figure 4.6 at 77 K and 0.01 T. (b) Normalized N-value and J_c as function of H for a porous 20º vicinal YBCO film. Inset refers to the I-V curves at different applied H fields. [Emergo 2008]

At low H fields, the $J_{c,L}$ values of the vicinal films are comparable, which is plausible since $J_{c,L}$ is the J_c in the ab-plane and should not be affected by vicinal angles. At higher H>0.01 T, the J_c value in both flat and vicinal samples decreases monotonically while a qualitative difference exists. In the former, J_c decreases gradually with increasing H field. In the latter, the J_c decreases more rapidly after an apparent "shoulder" in the J_c-H plot, occurring at H~0.01-0.02 T. This shoulder may correspond to the applied H where the density of magnetic vortices exceeds the pores' matching field H_m~ 6-16 mT estimated from the pore density of 5±3 pores/μm^2. This shoulder was also observed in the normalized N-H plot of the porous vicinal film in Figure 4.7(b). It is plausible that a switch from pore surface pinning to bulk pinning may have occurred near this shoulder. However, this switch is not expected to occur in the flat YBCO film since it has the same pinning mechanism for the whole field range.

Above the H_m, the $J_{c,L}$ in porous YBCO samples is determined by the bulk pinning centers available. The defects that were mostly observed in these porous vicinal films include nanoparticles (where the pores nucleated), stacking faults along the ab-planes and anti-phase boundaries (APBs). The edge and screw dislocations that may serve as dominant pinning centers in the flat YBCO samples are eliminated in the vicinal samples when the growth mode is switched from island-type [Hawley 1991 and Gerber 1991] to step-flow type [Lowndes 1992]. Also, the columnar defects that were observed on nonporous vicinal film with dimensions of 2-3 nm that traverse the entire film thickness [Lowndes 1995] were not observed in the porous vicinal

films. However, we are not ruling out the existence of other types of defects in these porous vicinal films, but we argue that their density may be small.

Since most of the nanoparticles observed in our films are nucleating sites for the nanopores, the nanoparticles and nanopores may have more or less the same density, on the order of $H_m \sim 6\text{-}16$ mT. Furthermore, even though other planar defects parallel to the ab-planes such as stacking faults have been observed on these porous vicinal films, they are not expected to make significant contributions to the $J_{c,L}$ when H is not parallel to them. Nevertheless, they are expected to improve the $J_{c,L}$ when H is parallel to the ab-plane (H||ab). As a matter of fact, a study on the H-orientation effect on $J_{c,L}$ of these vicinal films [Emergo 2009(a)] showed a slightly higher J_c peak at H||ab compared to that of a standard YBCO film. Thus, the most likely remaining defects in the porous vicinal film that may serve as bulk pinning centers are APBs. The APBs observed in nonporous vicinal YBCO films are mostly observed at the film-substrate interface with a vertical length of a few unit cells. They are planar defects along the L-direction with a matching field H_m estimated to be ~ 60 T for APBs with a mean distance of 6 nm [Haage 1997]. Nevertheless, the benefit of APBs on pinning was observed in the $J_{c,L}$ measured in the low field region of $H \sim 0.1\text{-}0.3$ T [Cantoni 2005]. Thus, the higher J_c values observed in porous vicinal films in the intermediate field region of $H_m \leq H \leq 0.3$ T may be due to the APBs.

To further analyze the factors affecting the H-dependence of the $J_{c,L}$ in the porous vicinal films, the H-dependence of the pinning force per volume (f_p) is shown in Figure 4.8, comparing three films: a flat YBCO, an 8° nonporous vicinal YBCO

53

(derived from Cantoni *et al's* study [Cantoni 2005]) and a 10º porous vicinal YBCO. For the vicinal samples, f_p is along the longitudinal direction. At H<0.03 T, the 10º porous vicinal YBCO shows the strongest f_p, suggesting the pore surface pinning is stronger than the APBs pinning in the nonporous vicinal sample and the bulk pinning in the flat sample. However, the crossover at H~0.03 T of the f_p's of the porous and nonporous vicinal films (which more or less coincides with the J_c-H "shoulder" discussed above) may signify the switch from pore surface pinning to the APBs pinning. Notice that the nonporous vicinal film has higher f_p at H>0.05 T than the porous vicinal film, which is not unexpected since the former has much higher APB density than the latter. At H~0.1 T, the f_p curves for the two vicinal samples experienced a crossover with that of the flat YBCO sample and above H~0.1 T the flat YBCO film has the highest f_p. One possible explanation for this crossover is that the APBs are relatively weaker pins since their length is only a few percent of the whole vortex length at 200 nm film thickness. Consequently, their effective pinning strength may be lower than that of the through-thickness screw dislocations and randomly distributed second phase inclusions in the flat YBCO films. A similar crossover of the $J_{c,L}$ in porous vicinal samples with the J_c of the flat sample observed at H~0.25 T may be due to the same reason. In addition, our recent experiment on adding BZO nanorods to the vicinal YBCO films shows that this crossover can be eliminated, supporting the argument that the crossover is caused by lack of the pinning centers in vicinal YBCO films [Emergo 2009(a)].
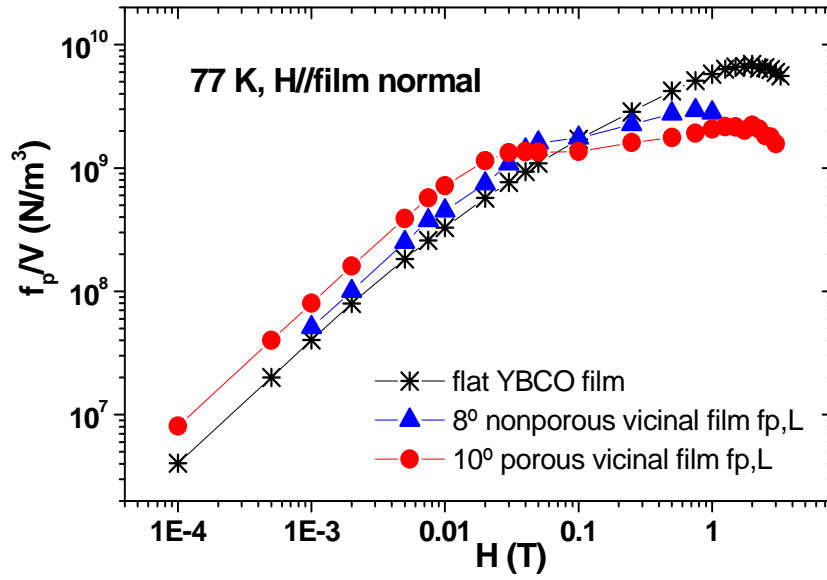
Figure 4.8 Pinning force per volume as function of the applied H field for a flat, 8º nonporous vicinal (derived from Cantoni 2005 data) and 10º porous vicinal YBCO films. [Emergo 2008]

Chapter 5

Anisotropy of the normal and superconducting properties of porous vicinal YBCO films

YBCO is composed of superconducting layers and almost insulating blocks, which results in a large anisotropy of the resistivity, $\rho(T)$, and J_c [Matshushita 2007]. In fact, the room temperature resistivity (ρ_{300K}) along the c-axis is an order of magnitude higher than that along the ab-plane. Also, the $\rho(T)$ along the ab-plane shows a metallic behavior while the $\rho(T)$ along the c-axis exhibits either a semiconducting or metallic behavior depending on the oxygen doping [Friedman1990, Takenaka 1994]. Consequently, the J_c flowing along the c-axis is much lower than that in the ab-plane. Finally, as discussed in Chapter 1, the J_c is much smaller in an applied magnetic field parallel to the c-axis than in a field parallel to the ab-plane.

It has been reported that the growth mode of $YBa_2Cu_3O_{7-\delta}$ (YBCO) films switches from island-type [Gerber 1991 and Hawley 1991] to step-flow type [Lowndes 1991 and 1994, Haage 1997, Habermeier 1998, Brötz 1999 and 2000, Jooss 1999, Czerwinka 2002, Cantoni 2005 and Djupmyr 2005] on vicinal SrTiO$_3$ (STO) substrates, where the c-axis is tilted at a small angle (θ_v) with respect to the normal to the substrate [refer to Figure 3.2]. Typically, the vicinal substrates are pre-annealed at high temperatures in ultrahigh vacuum, which facilitates cleaning of the

substrate surface and generating prominent surface steps on the substrate [Lowndes 1991 and 1994, Haage 1997, Habermeier 1998, Brötz 1999 and 2000, Jooss 1999, Czerwinka 2002, Cantoni 2005 and Djupmyr 2005]. The vicinal YBCO film on annealed STO substrates has a dense microstructure with steps on the film surface. In the direction along the steps, the so called longitudinal (L) direction, electrons move along the ab-planes while in the direction perpendicular to the steps (transverse or T-direction), the electrons' path has an angle θ_v with respect to the ab-planes. Consequently, higher resistivity is anticipated along the T-direction (ρ_T) as compared to the longitudinal resistivity ρ_L due to the intrinsic anisotropy of the YBCO [Friedman 1990 and Takenaka 1994]. The out-of-plane and in-plane resistivity anisotropy ratio (ρ_c/ρ_{ab}) on single crystal YBCO has been reported to be ~60 at 100 K [Friedman 1990 and Takenaka 1994] while on vicinal YBCO films, very scattered values of the ratio, ranging from 35 to 100, have been reported at the same temperature [Haage 1997, Habermeier 1998, Czerwinka 2002 and Pedarnig 2002].

It should be pointed out that the YBCO lattice is strained in vicinal growth, which may sensitively dictate the electronic structure and therefore affect the resistivity anisotropy. The critical current density J_c is also anisotropic between the L ($J_{c,L}$) and T ($J_{c,T}$) directions in a vicinal YBCO film. This anisotropy is, however, affected by both intrinsic electronic structure and extrinsic defect structures. The latter may behave differently in different magnetic fields (H). For example, the antiphase boundaries (APBs) that occurred on the prominent surface steps of the vicinal substrate have been found to provide strong transverse pins to the magnetic

57

vortices in low fields, leading to higher $J_{c,L}$. The J_c anisotropy $J_{c,L}/J_{c,T} \sim 1.67$ was reported on a 0.2 μm thick YBCO on an 8° STO substrate [Cantoni 2005]. At higher fields, H > 0.3 T, however, the effect of APBs was found to be minimal and the J_c anisotropy was reported to be ~1 on the same sample.

On the other hand, when a YBCO film is deposited directly on an as-received commercial vicinal substrate, the microstructure of the vicinal YBCO film becomes highly porous, as discussed in Chapter 4 [Emergo 2004, Emergo 2005, Polyanskii 2005, Wu 2008 and Emergo 2008]. Also, a significantly enhanced J_c has been observed in these porous vicinal YBCO films, which raises a question about the roles the pores play in the intrinsic electronic structure and magnetic pinning properties. A systematic study of the transport properties, particularly the anisotropy of the resistivity and the J_c as function of magnetic field, is important to shed insights on this matter. Motivated by this, we have made a comparative study of the transport properties of porous YBCO thin films and reference YBCO films made under optimized conditions. In this chapter, we report our experimental results.

5.1 Anisotropy of resistivity

The resistivity (ρ) vs. temperature (T) plots for the flat, 5°, 10° and 20° vicinal YBCO films are shown in Figure 5.1. The longitudinal resistivities $\rho_L(T)$ of the vicinal YBCO films are comparable, despite some subtle differences, to the resistivity along the ab-plane (ρ_{ab}) of the flat YBCO film in the entire temperature range of 100-300 K. Table 5.1 summarizes ρ_L and ρ_T for the 5°, 10° and 20° YBCO films at 300 K. The 300 K resistivity in the flat and longitudinal directions in vicinal YBCO films is in the

range of 230-260 $\mu\Omega\cdot$cm, which is typical of a standard c-axis oriented YBCO film measured in this work and reported previously [Friedmann 1990 and Takenaka 1994]. The ratio of the resistivity at 300 K and 100 K (ρ_{300K}/ρ_{100K}) of the vicinal samples ranges from 3.07-3.63, which is within $\pm14\%$ of the flat sample's ρ_{300K}/ρ_{100K} of 3.18. It should be mentioned that this ratio decreases with increasing θ_v. As a matter of fact, this ratio change results in a 20% difference in ρ_{ab} at 100 K between the 5° and 20° samples, as listed in Table 1. In addition, the T_c of the vicinal samples in the range of 89.24-89.36 K is comparable but slightly lower than that (89.89 K) of the standard sample. The slightly convex ρ_L-T curves for all four samples indicate that minor oxygen deficiency may occur in all samples. This seems to be reasonable considering they were made in the same run under identical processing conditions.
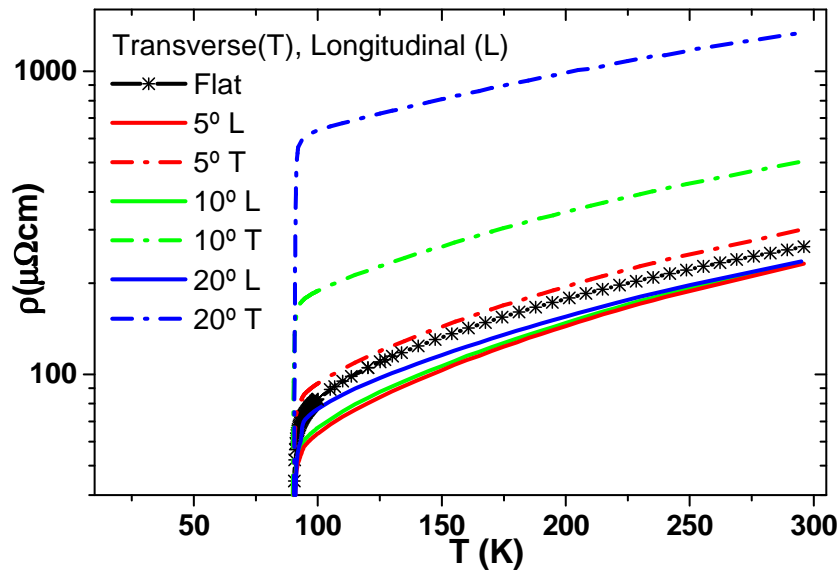
Fig 5.1 Resistivity versus temperature plots of the longitudinal and transverse bridges of 0.2 μm-thick porous 5°, 10° and 20° vicinal YBCO films. [Emergo 2008]

Miscut Angle	$\rho_L = \rho_{ab}$ ($\mu\Omega\cdot$cm) (300K)	ρ_T ($\mu\Omega\cdot$cm) (300K)	ρ_{ab} ($\mu\Omega\cdot$cm) (100K)	ρ_c ($\mu\Omega\cdot$cm) (100K)	ρ_T/ρ_{ab} (300K)	ρ_c/ρ_{ab} (300K)	ρ_c/ρ_{ab} (100K)
flat	263.6	263.6	82.77	-	1	-	-
5°	234.3	302	63.84	3941.50	1.29	39.82	61.74
10°	234.8	504.1	66.70	4118.22	2.15	39.02	61.74
20°	236	1339.4	77.00	4969.11	5.68	40.97	64.53

Table 5.1 Summary of ρ_{ab}, ρ_T, ρ_c and anisotropy (ρ_T/ρ_L, ρ_c/ρ_{ab}) for porous 5°, 10° and 20° vicinal YBCO films at 100 K and 300 K. [Emergo 2008]

The transverse resistivity $\rho_T(T)$ of vicinal samples [dash-dot lines in Figure. 5.1 is systematically higher and increases monotonically with θ_v (as listed in Table 1) due to the increasing contribution of the c-axis component $\rho_c(T)$. To assess this contribution quantitatively, $\rho_c(T)$ was estimated using the rotation of the resistivity tensor by θ_v, expressed as: $\rho_c = \left(\rho_T - \rho_L\cos^2\theta_v\right)/\left(\sin^2\theta_v\right)$ [Yun 2000]. The $\rho_c(T)$ data are depicted in Figure 5.2. It is shown that the ρ_c-T curves of all three vicinal YBCO films are comparable over the temperature range of 100-300 K with a metallic behavior, which is characteristic of an optimally-oxygenated YBCO film [Takenaka 1994]. However, the calculated ρ_c values of all three vicinal YBCO films, on the order of 3900-5000 $\mu\Omega\cdot$cm at 100 K (as summarized in Table 5.1), are higher than the reported ρ_c value for an optimally doped (~6.93 oxygen per unit cell) twinned single-crystal YBCO of ~3400 $\mu\Omega\cdot$cm [Friedmann 1990 and Takenaka 1994]. A possible reason for the observed higher ρ_c is the minor reduction of T_c caused most probably by minor oxygen deficiency as suggested in the ρ_L-T study. For a 120 nm-thick nonporous YBCO film on annealed 10º STO substrate, Haage *et al* reported an

increase in the ρ_c to ~6000 $\mu\Omega\cdot$cm at 100 K [Haage 1997], which is about 76% higher than that of the twinned crystal [Friedmann 1990 and Takenaka 1994]. Considering the decrease in T_c of ~3-4 K [Haage 1997] for this nonporous vicinal sample, it seems that the higher ρ_c in our porous vicinal samples cannot be fully accounted for by the minor T_c decrease of ~0.5-0.7 K. Another factor that can cause ρ_c to change is the uni-axial pressure along the c-axis [Crommie 1989]. Basically, ρ_c increases when the c-axis is expanded. Indeed, a 0.05% c-axis lattice constant increase was observed in the x-ray diffraction study of the 10° porous YBCO films, which is expected to raise ρ_c by ~16% according to a previous report [Crommie 1989]. This, together with the ~10% ρ_c increase due to the T_c reduction, is close to the ~21% ρ_c increase observed on this sample. Furthermore, the observed systematic increase in ρ_c with increasing vicinal angle is not unexpected since the T_c reduction and c-axis expansion increase with increasing vicinal angle.
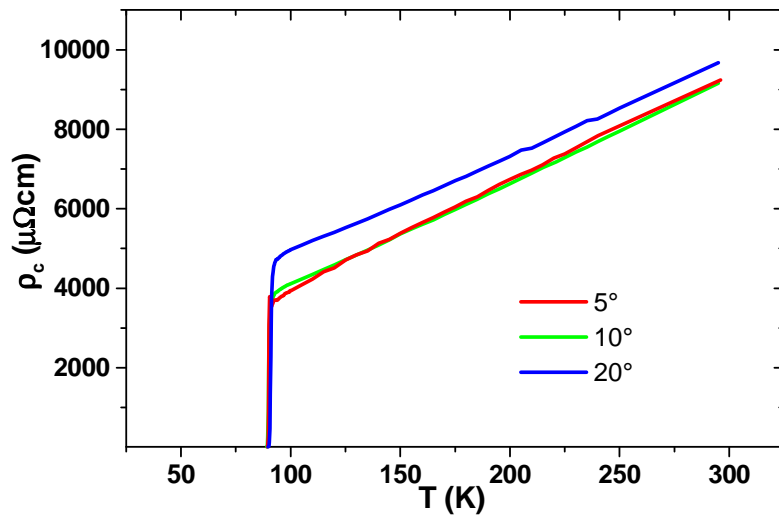
Figure 5.2 Temperature dependence of ρ_c of the porous 5°, 10° and 20° vicinal YBCO films. [Emergo 2008]

The resistivity anisotropy ratios at 100 K and 300 K for the three vicinal samples are listed in Table 5.1. Since the temperature slope of ρ_c is smaller than that of ρ_{ab}, higher resistivity anisotropy (ρ_c/ρ_{ab}) was observed at lower T, as shown in Figure 5.3(a). The anisotropy increases by about 65% from 300 K to 100 K. The normalized ρ_c/ρ_{ab} vs. T curves for 5°, 10° and 20° vicinal samples nearly coincide in the normal state as shown in Figure 5.3(b), indicating that the integrity of the YBCO lattice and its electronic structure in vicinal YBCO films are well maintained at relatively small vicinal angles up to 20°. This argument is further supported by the comparable values of ρ_c/ρ_{ab} at 100 K of our porous YBCO films (61.7-64.5) with that of single crystal YBCO film (~60) [Friedmann 1990 and Takenaka 1994]. It is interesting that the three vicinal samples have very close ρ_c/ρ_{ab} ratios at 100 K since the increase in θ_v affects both the ρ_c and ρ_{ab} in a similar way.
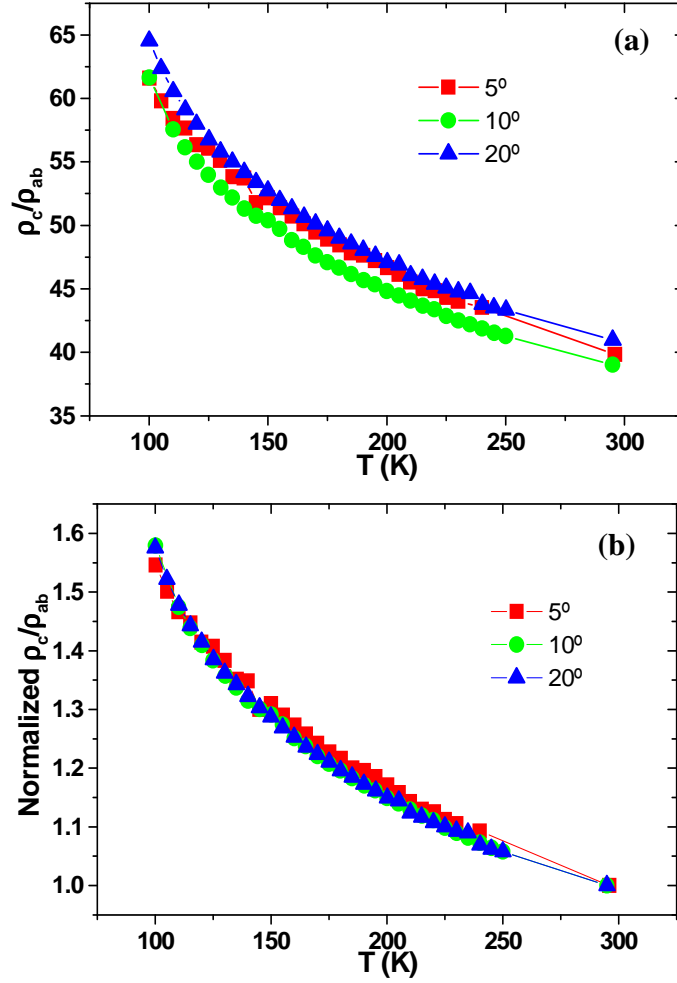
Figure 5.3 (a) Temperature dependence of ρ_c/ρ_{ab} for the porous 5°, 10° and 20° vicinal YBCO films; (b) Normalized temperature dependence of ρ_c/ρ_{ab} for the three samples mentioned above. [Emergo 2008]

5.2 Anisotropy of flux penetration

Figures 5.4(a) and (b) illustrate the magneto-optical (MO) images taken at T =10 K and H= 28 mT on a flat and a 10° vicinal YBCO film with film thickness of 0.2 µm. The flat sample (Figure 5.4(a)) has more or less uniform superconducting properties everywhere around the sample [Polyanskii 2005]. In homogeneous

63

superconductors of square or rectangular shapes, magnetic flux starts penetrating at the middle of the sample edges [Polyanskii 1996] and forms a "roof" pattern with well-developed diagonal lines (discontinuity d-line). These diagonal lines represent the region where the current changes direction by 90°. These dark color contrast lines are well visible in the MO image in Figure 5.4(a) (when H field was increased to 28 mT). The flux carrying regions have the bright contrast. The dark square at the center of the sample expels the external magnetic field and only the Meissner current circulates in this area. In contrast to the flat samples, the 10° vicinal YBCO film (Figure 5.4(b)) shows a very anisotropic flux penetration along the longitudinal and transverse directions. The magnetic flux exhibits a specific filamentary pattern and penetrates more easily along the longitudinal (P_L) direction due to the planar anti-phase boundaries (APBs) [Jooss 1999] generated in vicinal films during epitaxial growth. The APBs serve as strong pinning centers only for magnetic vortices traveling transverse with respect to the APBs [Haage 1997]. It is clearly seen in Figure 5.4(b) that the magnetic flux penetrates into the sample along the PL direction deeper than in the flat sample.

Figures 5.5(a) and (b) show, respectively, the streamlines and map of magnetization current extracted by a deconvolution procedure [Perkins 2002] of the same sample in Figure 5.4(b) at 10 K and 120 mT. The calculated images confirmed a very anisotropic current distribution in the vicinal film. The streamlines are much more dense in the direction of the growth steps and consequently the $J_{c,L}$ is much larger than $J_{c,T}$. Figure 5.5(a) illustrates that the streamlines of the magnetization

current flow uniformly along all edges of the sample and change direction by 90° directly on the d-lines where the strong contrast appears on MO images. The map of current distribution shows different intensity contrasts, which reflect the values of I_c flowing parallel and perpendicular to growth steps. The segments on the top and bottom of the image are brighter than in the direction perpendicular to the steps of growth. The intensity of the contrast ratio reflects the anisotropy of the critical current. The $J_{c,L}$ is about 3.5 times higher than the $J_{c,T}$ and this ratio is in good agreement with the anisotropy of critical currents taken by MO on a similar YBCO sample (0.24 µm thick 10° vicinal film at 4.2 K [Haage 1996]).

In order to study the temperature and field dependences of the J_c anisotropy of the 10° vicinal YBCO film, the lengths of the flux penetration P from the edges of this sample and $2b$ widths (width of flux-free Meissner region) were measured. The J_c's along the longitudinal and transverse directions at different temperature and applied field were calculated using the procedure described in references [Brandt 1993] and [Polyanskii 1996]. The same procedure was applied to calculate the J_c of the flat film. It was observed that the J_c's do not depend on H for 8 K≤T≤80 K as long as H is below the field of full flux penetration. Figure 5.6 presents the T-dependence of J_c in the 0.2 µm thick flat and 10° vicinal YBCO films taken at 10 K≤T≤80 K. As seen from the plot, the $J_{c,L}$ (closed triangles) is much higher than the $J_{c,T}$ (closed squares). The flat sample (closed circles) has J_c values higher than $J_{c,L}$ at T≤ 15 K. However, with increasing temperature the J_c of the flat sample decreases faster and becomes lower than $J_{c,L}$ and even lower than $J_{c,T}$ at T≥ 50 K. The plot of the

anisotropy of J_c in the 10° vicinal YBCO sample is shown as a function of T in the inset of Figure 5.6. The solid circles are the MO experimental data in the zero field-cooled (ZFC) regime, and the open circles, are the calculated ratio of PL/PT in remnant mode. Both measurements show the same results, namely, the influence of the growth steps is slowly disappearing with increasing temperature.

Figure 5.4 MO images of flux behavior in the 0.2 µm thick (a) flat and (b) 10° vicinal YBCO samples taken at temperature T=10 K and H= 28 mT. $2w$ is the sample width, $2b$ is the width of flux-free Meissner region and *PL* and *PT* are the depths of flux penetration parallel and perpendicular to the steps of growth, respectively. [Polyanskii 2005]
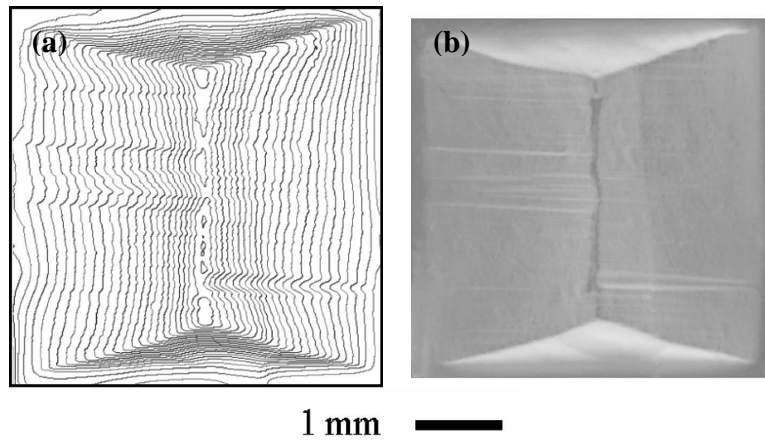
Figure 5.5 (a) Contours of the magnetization current streamlines and (b) current distribution map calculated by deconvolution procedure for MO image of the same sample in Figure 5.4(b) taken at 10 K and 120 mT. [Polyanskii 2005]
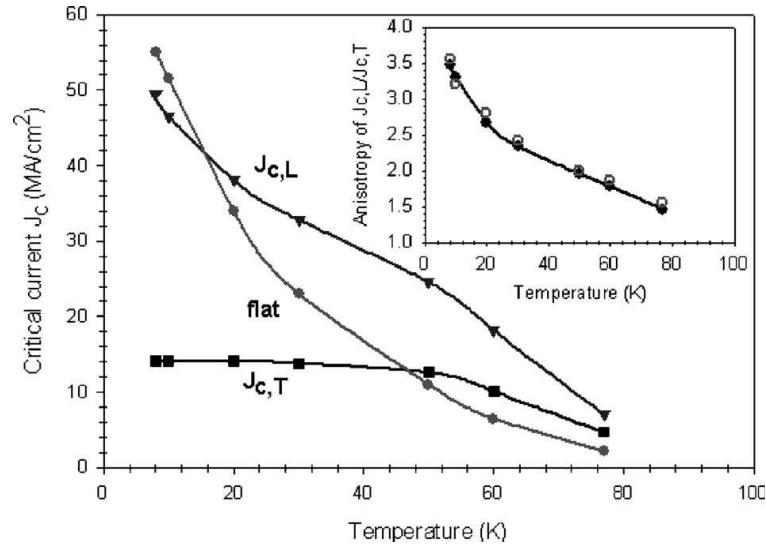
Figure 5.6 Temperature dependence of J_c in the 0.2 µm thick flat (circle) and 10° (square and triangle) vicinal YBCO samples. Inset: T dependence of the J_c anisotropy ($J_{c,L}$ /$J_{c,T}$) in the vicinal sample. [Polyanskii 2005]

5.3 Anisotropy of transport J_c

The transport $J_{c,L}$ (solid) and $J_{c,T}$ (open) of the 5° (red), 10° (green) and 20° (blue) porous vicinal YBCO films are shown as function of magnetic field at 77 K in Figure 5.7. The highly anisotropic J_c observed in the MO images were also observed here. Quantitatively, in the SF, the ratio of $J_{c,L}/J_{c,T}$ is around 2.45 for the 10° sample. Figure 5.7 also reveals that the J_c anisotropy is strongly affected by the applied magnetic field and the detailed analysis will be given in Figure 5.8. The low-field (SF and 0.01 T) and high-field (1 T) J_c anisotropy is listed in Table 5.2 for 5°, 10° and 20° films, respectively.

The detailed analysis of the $J_{c,L}$ of the vicinal films with respect to applied magnetic field was given in Chapter 4. It was observed that the $J_{c,L}$ at low field is not

affected by the substrate vicinal angle. The $J_{c,T}$ value of the vicinal samples, on the other hand, decreases with increasing vicinal angle due to the increasing contribution of the c-axis component. However, it is interesting to point out that the SF $J_{c,T}$ in the 5º YBCO film is still 32% higher than that of the flat YBCO film's J_c. Since the APB pinning is known to contribute along the L-direction only, this higher $J_{c,T}$ in porous film with small vicinal angle may be attributed to the strong pore surface pinning. For the 10º and 20° films, the $J_{c,T}$ is lower than the J_c in the flat sample due to a more reduced cross sectional area of the current flow in the ab-plane. It should be noticed that the observed $J_{c,T}$ on the 10º porous vicinal film is ~35% higher than that reported on an 8º nonporous vicinal YBCO film [Cantoni 2005], indicating the benefit of strong pore surface pinning in improved $J_{c,T}$ at SF and low H.
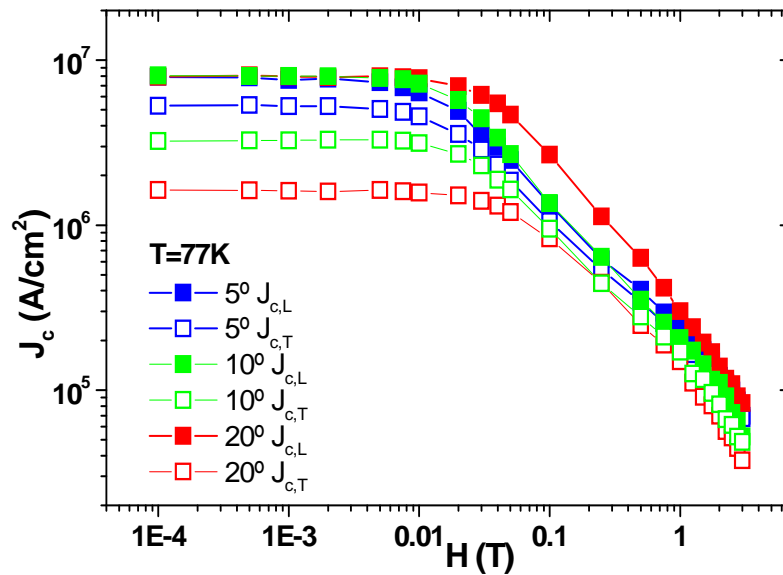
Figure 5.7 (a) H-dependence of the transport $J_{c,L}$ and $J_{c,T}$ values of 0.2 μm thick porous 5°, 10° and 20° vicinal YBCO films.

A similar J_c-H trend can be observed along the T-direction for the same reasons discussed for the L-direction J_c. In fact, the switch from pore surface pinning to bulk pinning may occur in the T-direction. The experimental data supporting this argument are the similar locations of the H~0.01-0.02 T "shoulders" in the L- and T-directions, which is expected from the same pore density in the two directions. To quantify the J_c anisotropy, Figure 5.8 shows the ratio of $J_{c,L}/J_{c,T}$ as a function of H for the three vicinal YBCO films. It is interesting to note that the three curves follow the same trend qualitatively with a constant J_c anisotropy ratio at low fields (H<0.01-0.02 T) followed by a rapid decrease of this ratio at higher H fields to a new constant above H~1 T. Generally, the J_c anisotropy increases with vicinal angle.
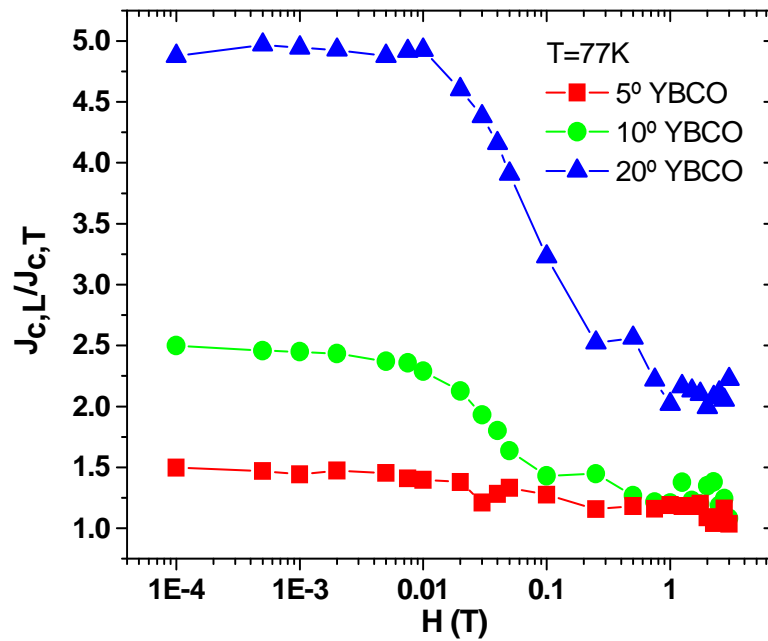
Figure 5.8 H-dependence of $J_{c,L}/J_{c,T}$ of the porous 5°, 10° and 20° vicinal YBCO films at 77 K. [Emergo 2008]

The constant anisotropy observed for 0 T<H<0.01 T suggests the same or at least similar pinning mechanisms (such as the pore surface pinning) determining $J_{c,L}$ and $J_{c,T}$ in this field range and the anisotropy may be attributed to the c-axis contribution in the T-direction. One interesting observation worthy of mentioning is that the ratio of the J_c between L- and T-directions is comparable to the ratio of resistivity between T- and L-directions at 300 K for all three vicinal samples (see Table 5.2). The rapid decrease in anisotropy at 0.01 T<H<0.2 T may be due to the rapid diminishing of the APBs' pinning strength. While the mechanism is not fully understood, Jooss *et al* also observed this rapid decrease in anisotropy from 0.01 T to 0.2 T on a nonporous 0.24 µm-thick YBCO film deposited on annealed 10° STO substrate at 5 K [Jooss 2000]. At higher fields, the two J_c directions only have isotropic pinning centers and exhibit the same field dependence and constant anisotropy. Furthermore, we have observed that on a 0.2µm-thick 10° YBCO film, the anisotropy value of ~2.45 obtained from the transport measurement is 38% higher than the previously reported anisotropy value of ~1.5 measured by MOI at SF and 77 K [Polyanskii 2005]. The MOI anisotropy of this sample was observed to be 23% higher than the reported MOI anisotropy of ~1.22 in a nonporous vicinal film of the same vicinal angle and thickness [Djupmyr 2005].

Miscut Angle	$J_{c,L}/J_{c,T}$ (SF,77K)	$J_{c,L}/J_{c,T}$ (0.01T,77K)	$J_{c,L}/J_{c,T}$ (1T,77K)
flat	1	1	1
5°	1.46	1.40	1.19
10°	2.45	2.29	1.21
20°	4.86	4.92	2.02

Table 5.2 Summary of $J_{c,L}/J_{c,T}$ for porous 5°, 10° and 20° vicinal YBCO films at 77 K and 0 T, 0.01 T and 1 T.

Chapter 6

Improving $J_c(B, \theta)$ by incorporating splayed BaZrO$_3$ (BZO) nanorods

In Chapters 4 and 5, tremendous improvement in the low field J_c was achieved by doping the YBCO film with nanotube pores. Unfortunately, the J_c drops rapidly at H >20 mT due to an insufficient density of the nanotube pores. Furthermore, at H >0.2 T, the un-doped flat YBCO film has higher J_c than the porous vicinal YBCO films because the edge and screw dislocations that may serve as dominant pinning centers in the un-doped flat YBCO samples are eliminated in the vicinal samples when the growth mode is switched from island-type to step-flow type [Lowndes 1992].

High J_c values at H >1 T are necessary for the application of YBCO films in devices such as motors and generators [Larbalestier 2001]. During the past decade or so, many exciting results have been obtained by incorporating strong pinning centers in YBCO films in order to enhance the in-field J_c and reduce the J_c anisotropy with respect to the orientation of the applied magnetic field [Foltyn 2007]. Nanoparticles, such as BaZrO$_3$ nanorods (BZO-NRs), which self-assemble into columnar defects along the c-axis of the YBCO matrix have been found to dramatically improve J_c by factors of 1.5-5 in applied magnetic fields and lower the $J_{c,SF}$ (J_c in self field) to $J_{c,5T}$ ratio as compared to that in un-doped YBCO films [Driscoll 2004, Yamada 2005, Goyal 2005, Kang 2006, Peurla 2006, Peurla 2007, Pompeo 2008, Mele 2008]. In

addition, the strong correlated pinning provided by the aligned BZO-NRs in the YBCO film resulted in a prominent peak in the angular dependence of J_c (J_c-θ) when the applied magnetic field H is parallel to the c-axis (H||c). Consequently, the J_c anisotropy between the H||c and H||ab directions was decreased. However, since the BZO-NRs are aligned nearly perfectly along the c-axis, the in-field J_c is not much improved or even reduced at field orientations deviating from the c-axis. This is unfortunate for many applications of YBCO coated conductors, such as motors and generators, wherein the generated strong magnetic field may bend or twist causing the vortices to stray from the correlated pins. Splaying columnar defects in YBCO films may provide an effective solution to this problem. In fact, theoretical work by T. Hwa *et al* predicted that splayed columnar defects force vortex entanglement and enhance J_c [Hwa 1993]. In addition, YBCO single crystals containing splayed columnar defects produced by high-energy Sn ion irradiation was observed experimentally to carry higher J_c(B) than those with more or less the same density of uniformly oriented columnar tracks [Civale 1994].

Strain manipulation may provide a promising approach to achieve splayed BZO-NRs via growth. In fact, the mechanism proposed to explain the formation of BZO-NRs along the c-axis of YBCO films is similar to that responsible for the vertical assembly of quantum dots (QDs) in heteroepitaxy of semiconductors of large lattice mismatch [Gao 2008]. The strain generated, which is determined by the elasticity of the embedding material, serves as a nucleation site for succeeding QDs [Zhang 2004]. Theoretical [Holy 1999] and experimental [Springholz 1998] studies

73

have also shown that the complexity of the QD stacking can be determined by the elasticity of the embedding matrix and/or the growth direction of the QDs. This implies that the alignment of the BZO-NRs in YBCO may be manipulated by altering one or both of the above-mentioned parameters. On vicinal SrTiO$_3$ (STO) substrates [Lowndes 1992], an anisotropic elastic strain in the YBCO film exists [Haage 1997] due to the mismatch between the substrate step height and the YBCO's unit cell. This additional strain may produce a possible control of the alignment of the BZO-NRs. In this chapter, we show that a relatively simple experimental method of depositing on vicinal substrates - can be used to increase the average splay of the BZO nanorods almost to the optimum predicted by theory [Hwa 1993] . As a consequence, a strong benefit is realized and the J$_c$ is strongly increased for a wide range of angles, compared to non-vicinal growth.

6.1 Surface morphology, cross-section and crystalline structure of vicinal YBCO/BZO-NRs films

A comparison of the surface morphology between the vicinal YBCO and vicinal YBCO/BZO-NRs films was made and scanning electron microscope (SEM) images are shown in Figures 6.1 (a) and (b). The striking difference between the two morphologies is the reduced density of nanopores and nanopore dimension in the presence of BZO-NRs. This may be attributed to the much reduced nanoparticle formation with BZO-NRs doping. Our recent investigation suggests that these nanoparticles serve as catalysts for nanopores. [Wu 2008] It is also possible that the

nanopores became squeezed by the additional BZO-NRs, suggesting that the nanopores absorbed the strain induced by the insertion of BZO-NRs.
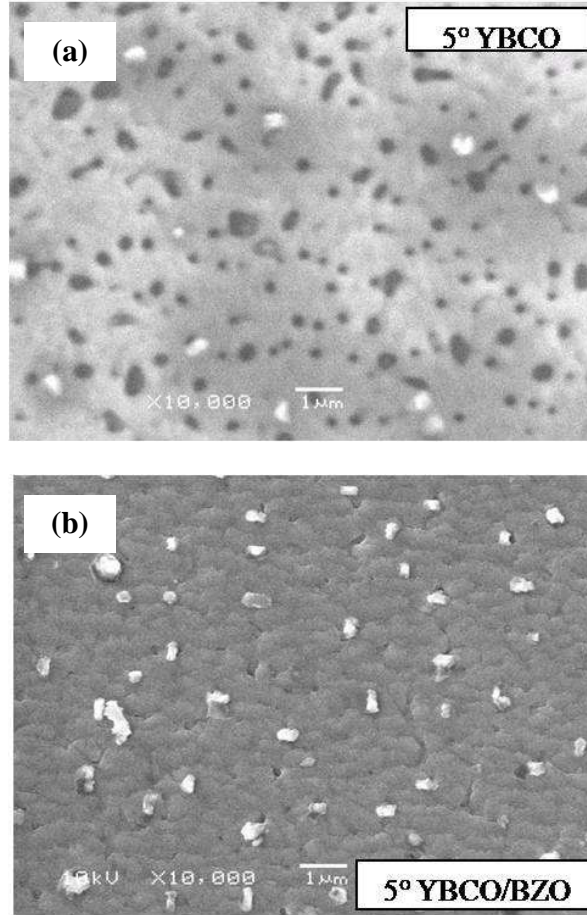
Figure 6.1 SEM images of the surface morphology of 0.2 µm thick (a) 5° porous vicinal YBCO film and (b) 5° vicinal YBCO/BZO-NRs film.

A cross-sectional TEM image of the vicinal YBCO/BZO-NRs film is shown in Figure 6.2. The BZO-NRs initiate near the film-substrate interface and traverse through the whole film thickness. The average width of the BZO-NRs is 5.72±1.62 nm, which is within the range of reported values [Goyal 2005, Peurla 2006 and Mele 2008]. The ab-plane is tilted by ~5° with respect to the film-substrate interface and

corresponds very well to the substrate miscut angle. Consequently, the c-axis is tilted by ~5° to the right of the vicinal YBCO/BZO-NRs film normal. Previously, our group have reported that in the flat YBCO/BZO-NRs film, the BZO-NRs' mean splay around the c-axis is 5.3±2.4° [Baca 2009]. Representative nanorods in Figure 6.2 are labeled with white dashed lines and their angles, θ, with respect to the c-axis are also included. The majority of the BZO-NRs is tilted towards the film normal with an angle of up to 20° from the c-axis and thus, is expected to shift the J_c-θ peak to the left of the c-axis direction. This asymmetric orientation of the BZO-NRs is a manifestation of the anisotropic strain induced by vicinal growth. The mean splay of the BZO-NRs around the c-axis is 9.7 ± 3.0°, which is almost twice that observed in its flat counterpart. The splayed BZO-NRs are expected to improve the J_c values via vortex entanglement as observed in Sn-irradiated YBCO single crystals [Civale 1994]. Furthermore, it has been established that a splay angle of ~10° around the c-axis results in the best J_c values [Hwa 1993, Hardy 1996, Krusin-Elbaum 1996 and Park 1997]. Due to the splayed distribution of the BZO-NRs, it is difficult to determine the absolute defect spacing and matching field, B_m. However, an estimate yields an average separation of 15.15±6.93 nm and B_m in the range of 4.3 T-30.6 T. The B_m of ~9 T reported on flat YBCO/BZO-NRs films containing a similar BZO concentration falls within this range [Goyal 2005].
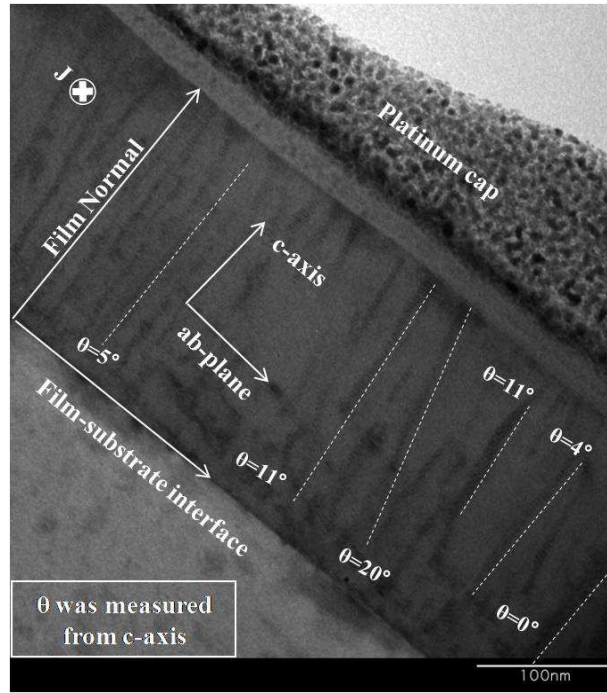
Figure 6.2 Cross-sectional TEM data of a 0.2
μm thick 5° vicinal YBCO/BZO-NRs film.

Analysis of the lattice constants from the x-ray diffraction patterns, as illustrated in the position of the (005) peaks in Figure 6.3, showed that the c-axis of the flat YBCO film increased from 11.74 Å to 11.82 Å upon insertion of BZO-NRs. This confirms previously reported c-axis expansion in flat YBCO/BZO-NRs films [Mele 2008]. Since the expansion of the YBCO's c-axis leads to an increase in the separation between the superconducting CuO_2 planes, T_c is usually reduced [Crommie 1989]. Thus, this expansive c-axis strain could be the culprit in the observed reduction of T_c in flat YBCO/BZO-NRs films [Mele 2008]. On the other hand, the c-axes of the YBCO and YBCO/BZO-NRs films decreased to 11.55 Å and 11.56 Å respectively when grown on the vicinal substrate. Consequently, this slight compression of the c-

axis is expected to improve T_c [Crommie 1989] and indeed transport measurements showed that the vicinal YBCO/BZO-NRs film has a T_c of ~88.30 K, in contrast to a T_c of ~86.14 K in the flat YBCO/BZO-NRs film. Finally, Figure 6.3 also shows the full-width-at-half-maximum (FWHM) of the (005) peak for the four films. The addition of BZO-NRs in the flat YBCO film increased the FWHM from ~0.24° to ~0.34°. On the contrary, the FWHM decreased to ~0.15° when the BZO-NRs were incorporated inside the vicinal YBCO film, which is comparable to the vicinal YBCO film's FWHM of ~0.13°. This demonstrates that aside from dispersing the BZO-NRs' orientation, the vicinal growth also promotes better crystalline alignment and reduces T_c degradation.
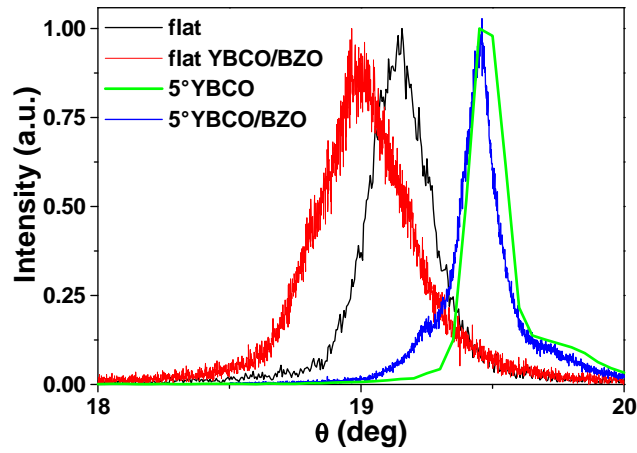
Figure 6.3 FWHM of the (005) peak of the flat and 5° porous vicinal YBCO and flat and 5° vicinal YBCO/BZO-NRs films.

6.2 Normal state properties of vicinal YBCO/BZO-NRs film

Figure 6.4 illustrates the temperature dependence of the ρ_L for the four samples shown in Figure 6.3. The flat YBCO/BZO-NRs film (blue) has the highest ρ_L

in the normal state while the vicinal YBCO sample (green) has the lowest. Interestingly, the ρ_L of the vicinal YBCO/BZO-NRs film (red) is much lower than that of its flat counterpart. At 300 K, the ρ_L of ~252.60 $\mu\Omega\cdot$cm of the former is about 39.5% lower than that of the latter. In fact, the ρ_L-T curve of the vicinal YBCO/BZO-NRs film almost coincides with that of flat YBCO film (black), suggesting that the detrimental strain on the flat YBCO/BZO-NRs lattice that causes T_c reduction and ρ_L increase could be eliminated by introducing additional strain via vicinal growth.
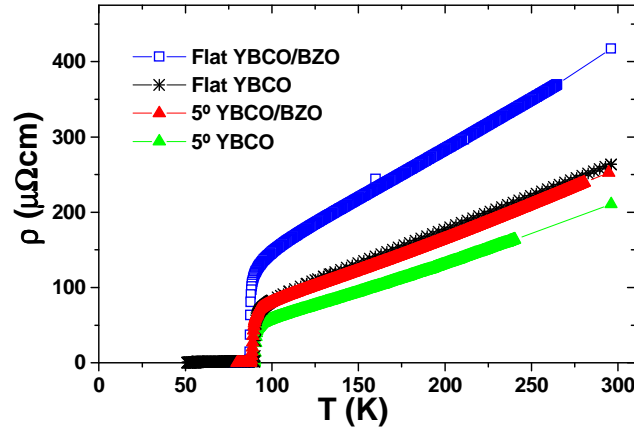
Figure 6.4 Temperature dependence of the longitudinal resistivity, $\rho_L(T)$, of 0.2 µm thick flat and 5º porous vicinal YBCO and flat and 5º vicinal YBCO/BZO-NRs films.

6.3 Comparison of J_c in YBCO films containing splayed and non-splayed BZO-NRs

The J_c's as a function of H (when H is parallel to the c-axis) for the four above-mentioned films are shown in Figure 6.5. The J_c value at self field of the flat YBCO/BZO-NRs film falls within the range of reported values [Goyal 2005 and Mele 2008]. The $J_{c,SF}$ of ~5.4 MA/cm^2 in the vicinal YBCO/BZO-NRs film (red) is lower

than that of vicinal YBCO film (green), which is most probably due to a more effective defect-YBCO interface and therefore higher pinning potential energy in the latter case [Wu 2008]. A possible culprit can also be the decreased superconducting volume in the vicinal YBCO/BZO-NRs film. Nevertheless, the $J_{c,SF}$ in the vicinal YBCO/BZO-NRs film is ~100% and ~28% higher than that of the flat YBCO/BZO-NRs (blue) and flat YBCO (black) films, respectively. This is not surprising considering the combined benefits of better ab-plane conduction and higher T_c in the vicinal YBCO/BZO-NRs film. Comparison of the $J_{c,SF}$ for the flat YBCO and flat YBCO/BZO-NRs films at the same reduced temperature showed that the latter's lower $J_{c,SF}$ is not entirely due to its lower T_c [Wang 2008]. The change in temperature corresponds to only a ~60% increase in $J_{c,SF}$ of the flat YBCO/BZO-NRs film [Wang 2008]. In the applied field of 30 mT < H $\leq$ 5 T, the vicinal YBCO/BZO-NRs film carries the highest J_c among the four samples.

The inset of Figure 6.5 illustrates the comparison of J_c as a function of H (when H is along the c-axis) for 1.0 µm-thick flat and vicinal YBCO/BZO-NRs films. The J_c-H trend of the two films follows the same J_c-H trend of the 0.2 µm-thick films at H$\leq$ 2 T. However, at H> 2 T, a crossover between the J_c's of the flat and 5° vicinal YBCO/BZO-NRs films occurs signifying a weakened pinning along the c-axis of the latter. This suggests that the alignment of BZO-NRs along the c-axis in vicinal films is not preserved at higher thickness.
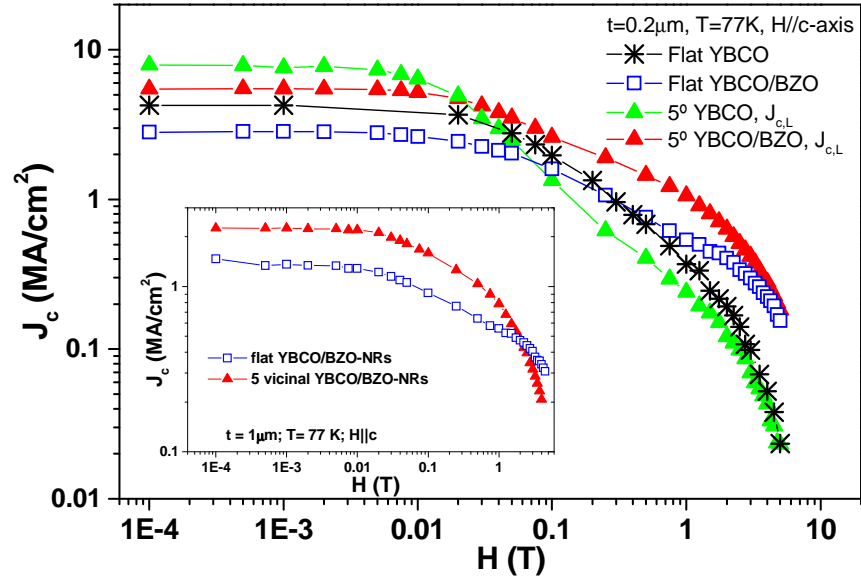
Figure 6.5 J_c vs H plot of 0.2 µm thick flat and 5° vicinal YBCO films and flat and 5° vicinal YBCO/BZO-NRs films in log-log scale. Inset: J_c vs H plot of 1.0 µm thick flat and 5° vicinal YBCO/BZO-NRs films in log-log scale.

Figure 6.6 depicts the pinning force density ($\mathbf{F_p}/V=\mathbf{J_c(H)}\times\mathbf{H}$) as a function of H for the four samples mentioned above. The flat and vicinal YBCO/BZO-NR samples both show a strong peak in the H field range of 2-3.5 T, suggesting that the BZO-NRs are responsible for pinning in both cases. Interestingly, the peak location for the vicinal YBCO/BZO-NRs sample is at ~2.5 T while that of the flat one is higher at ~3.2 T. This peak location has been observed to depend on the defect density of the film but it does not correspond to the matching field [Macmanus-Driscoll 2004 and Mele 2008]. At the peak, the $\mathbf{F_p}/V$~12.8 GN/m³ of the vicinal YBCO/ZO-NR sample is about 44% higher than that of its flat counterpart, which may be attributed to the improved pinning efficiency by "splaying" the BZO-NR columnar defects [Hwa 1993, Civale 1994, Hardy 1996, Krusin-Elbaum 1996 and Park 1997]. The FWHM of the

81

F_p/V peak in the former is about 4.3 T as compared to 5.2 T in the latter case, which is probably caused by the lower density of BZO-NRs in the vicinal YBCO/BZO-NR sample. This suggests that better overall F_p/V performance may be obtained by increasing the volume portion of the BZO-NR doping in vicinal YBCO film.
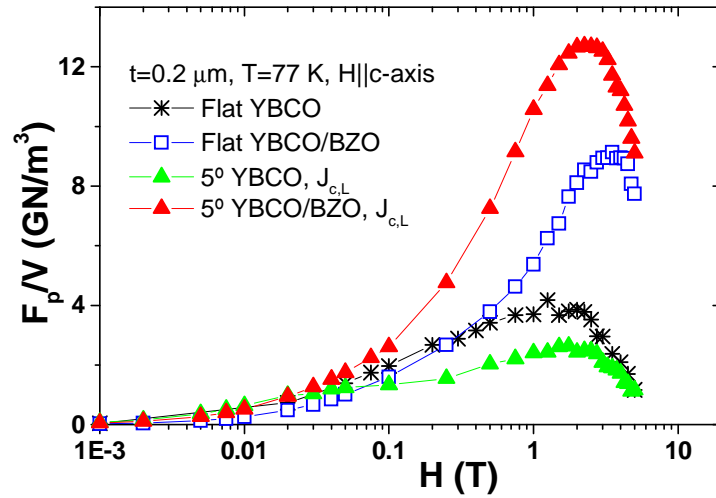
Figure 6.6 Field dependence of the pinning force density (F_p/V) for the flat and vicinal YBCO films and flat and vicinal YBCO/BZO-NRs films.

6.4 Angular dependence of J_c in YBCO films doped with splayed BZO nanorods

Figure 6.7(a) compares the angular dependence of J_c at 1 T and 77 K for the four samples shown in Figure 6.6. Note that the J_c-θ peak of the vicinal YBCO/BZO-NRs film is shifted to the left of the c-axis direction by ~20°, confirming the tilt angle observed from the TEM data. In fact, a comparison of the J_c-θ plots at 5 T and 77 K in Figure 6.7(b) shows that the peak is actually ~13° to the left of the c-axis, suggesting that the majority of the BZO-NRs are tilted in this direction. Finally, the utmost advantage of the splayed BZO-NRs is the availability of strong pins on a

wider field orientation. As a matter of fact, the vicinal YBCO/BZO-NRs film carries the highest J_c in all the field directions at both fields. At 1 T, the J_c of ~0.76 MA/cm^2 at the valley of the J_c-θ curve of the vicinal YBCO/BZO-NRs film is 97.5%, 111% and 200% higher than that of the flat YBCO, flat YBCO/BZO-NRs and vicinal YBCO films, respectively. Furthermore, this splayed alignment of the BZO-NRs reduces the anisotropy of the J_c at different magnetic field orientations, resulting in a peak-to-valley ratio of ~1.88 on the vicinal YBCO/BZO-NRs film, which is less than half of that on the flat YBCO film (~3.79) and vicinal YBCO film (~3.75). The benefit of splaying the BZO-NRs is more apparent at high field especially at the H||ab direction as shown in Figure 6.7(b). The much enhanced peak at H||ab of the vicinal YBCO/BZO-NRs film suggests that vicinal growth may also generate defects along the ab-planes.

The J_c-θ plots at 1 T and 77 K for the 1.0µm-thick flat and vicinal YBCO/BZO-NRs films are shown in Figure 6.7(c). The H||c peak in the J_c-θ curve is still very prominent in the flat YBCO/BZO-NRs film, suggesting that the BZO-NRs are still aligned along the c-axis. However, the broadened H||c peak in the 5° vicinal YBCO/BZO-NRs film is very broad and asymmetrical, confirming that the BZO-NRs' alignment along the c-axis is diminished at higher thickness resulting in lower J_c at H> 2 T. Nevertheless, the 5° vicinal YBCO/BZO-NRs film carries the highest J_c for all field orientations. This implies that the vicinal growth helped release the strain during BZO-NRs insertion by broadening the alignment of BZO-NRs, thus allowing us to achieve high $J_c(B,\theta)$ in thick films.
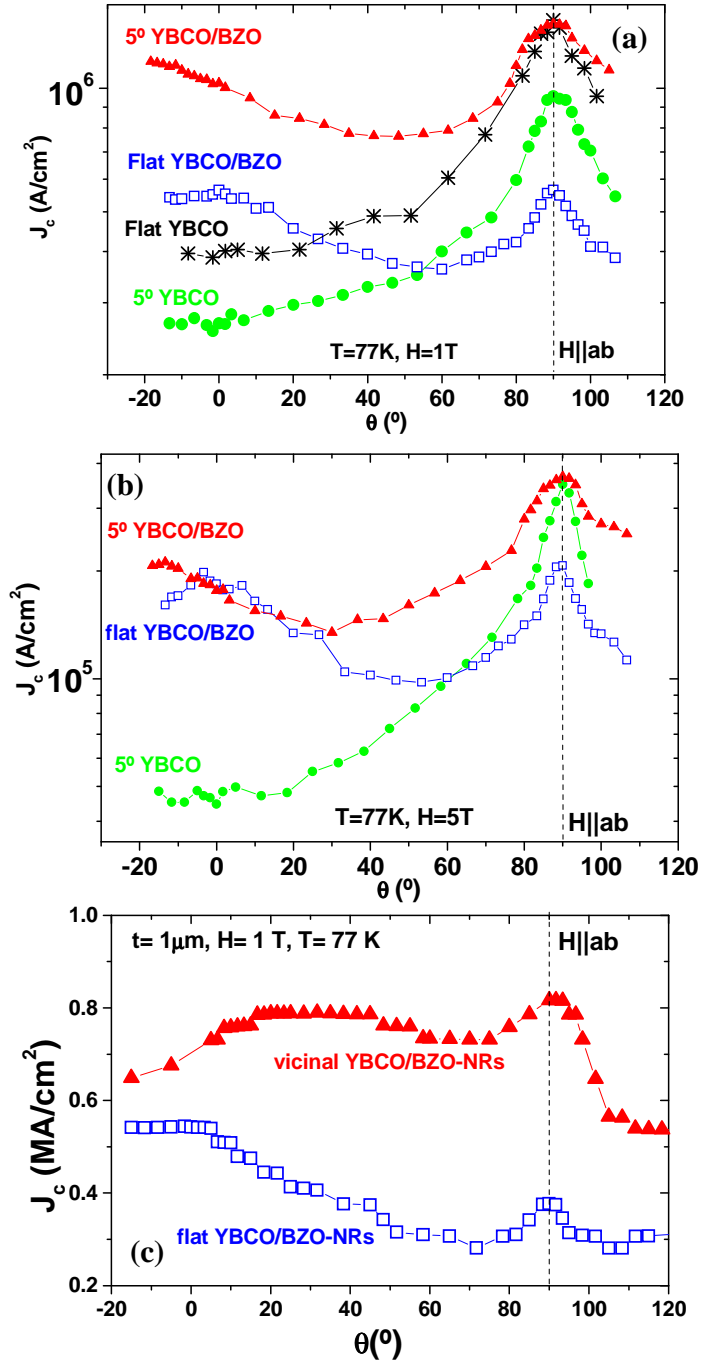
Figure 6.7 (a) J_c-θ plot at 1 T and 77 K of 0.2 µm thick flat and 5° porous vicinal YBCO films and flat and 5° vicinal YBCO/BZO-NRs films; (b) J_c-θ plot at 5 T and 77 K of 0.2 µm thick 5° porous vicinal YBCO film and flat and 5° vicinal YBCO/BZO-NRs films; (c) J_c-θ plot at 1 T and 77 K of 1.0 µm thick flat and 5° vicinal YBCO/BZO-NRs films.

84

6.5 Effect of vicinal angle on the H-dependence of J_c in BZO-doped YBCO films

YBCO/BZO-NR films with 0.2 µm thickness were deposited on flat, 5°, 10° and 20° vicinal STO substrates. All the vicinal YBCO/BZO-NR films have higher T_c than their flat counterpart, and the T_c values are summarized in Table 6.1. Furthermore, the flat YBCO/BZO-NR film has the highest resistivity, suggesting that the latter is subjected to higher lattice strain, and may contain more defects.

Miscut Angle	T_c (K)	J_c (MA/cm^2) (SF,77 K)	Crossover Field with Flat (H‖c)
Flat	86.33	2.72	-
5°	88.30	5.44	5 T
10°	89.38	6.38	1.25 T
20°	89.07	5.39	0.6 T

Table 6.1 Summary of T_c, J_c at 0 T and 77 K and crossover H‖c field for the flat, 5°, 10° and 20° vicinal YBCO/BZO-NRs films.

Figure 6.8 depicts the field dependence of J_c when H is along the c-axis for the four YBCO/BZO-NRs films and the $J_{c,SF}$ values at 77 K are summarized in Table 6.1. All the vicinal films have higher self field and low field (H<0.3 T) J_c than the flat YBCO/BZO film, which is attributed to the higher T_c and better crystalline alignment in the vicinal films. However, it is interesting to note that the J_c values at high field decreases with increasing vicinal angle. The magnetic fields where the cross-over between the J_c's of the vicinal YBCO/BZO-NR films and the flat YBCO/BZO-NR

film occur are summarized in Table 6.1. The decreasing cross-over field suggests a

decreasing density of c-axis aligned BZO-NRs with increasing vicinal angle.
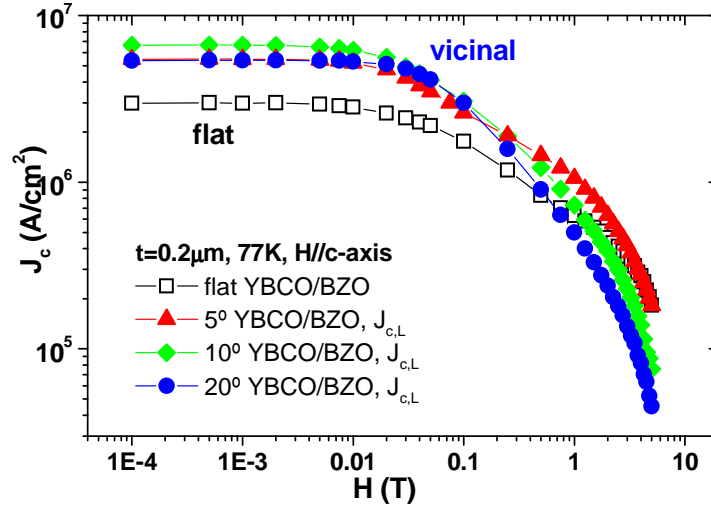
Figure 6.8 J_c-H plots at 77 K for the flat, 5°, 10°
and 20° vicinal YBCO/BZO-NRs films.

Figure 6.9 illustrates the angular dependence at 5 T and 77 K of the four films

mentioned above. The direction parallel to the film normal is labeled in the plot. It is

observable that the J_c-θ plots of the flat and 5° YBCO/BZO-NR films exhibit peaks

when H is along the c-axis. These are manifestations of the strong pinning due to the

c-axis aligned BZO-NRs which were indeed observed from the TEM cross-sections

of the flat and 5° YBCO/BZO-NRs films (Figures 6.10 (a) and (b)). However, the

absence of the J_c-θ peak at H||c for the 10° and 20° vicinal YBCO/BZO-NRs films

suggests that the alignment of BZO-NRs along the c-axis is destroyed at higher

vicinal angle. Furthermore, the decreasing J_c at H||c with increasing vicinal angle

implies that a systematic change in the alignment of the BZO-NRs occurs. As a

matter of fact, Figure 6.10(c) shows that the 10° vicinal YBCO/BZO-NR film has a lower density of BZO-NRs along the c-axis and a higher density of BZO-NRs along the ab-plane; and, interestingly, Figure 6.10(d) shows that the BZO-NRs are completely aligned along the ab-plane when the substrate vicinal angle was increased to 20°. The J_c-θ peak in the H||ab-plane exists for all films. Notice from the TEM cross-sections in Figures 6.10 (a)-(d) that the ab-plane is tilted from the film-substrate interface by an angle corresponding to the substrate vicinal angle. These tilts result in the shifting of the J_c-θ peak at H||ab in Figure 6.9. The flat film's lower peak when H is along the ab-plane implies a decrease in the pinning along the ab-plane, which can be attributed to reduced ab-plane alignment. On the other hand, all vicinal films exhibited enhanced J_c in the H||ab direction. As a result, the 5° YBCO/BZO-NR film gives the optimal $J_c(B,\theta)$ because it takes advantage of the strong pinning due to the correlated BZO-NRs along the c-axis while preserving the integrity of the ab-plane. It is expected that the 20° vicinal YBCO/BZO-NR film will have the narrowest and highest J_c-θ peak when H is along the ab-plane since the majority of the BZO-NRs are aligned along this direction.
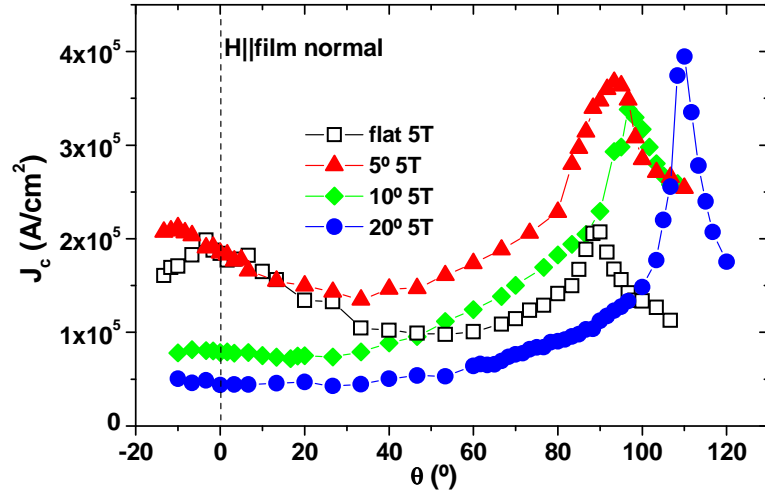
Figure 6.9 J_c-θ plots at 5 T and 77 K for the flat, 5°, 10° and 20° vicinal YBCO/BZO-NRs films.
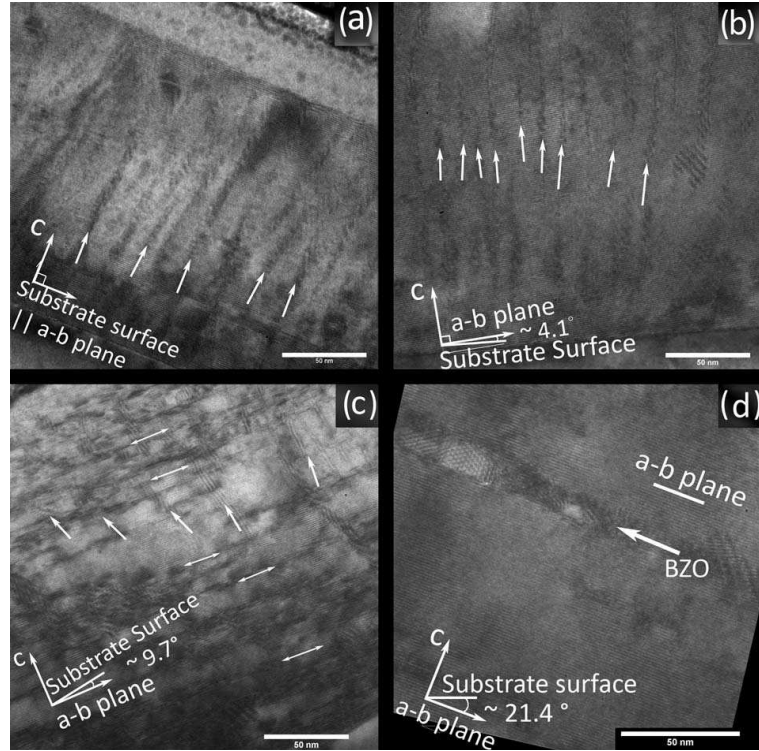
Figure 6.10 TEM cross-sections of BZO-NRs doped YBCO films deposited on (a) flat STO substrate, (b) 5°, (c) 10° and (d) 20° vicinal STO substrates. [Baca 2009]

Chapter 7

Effect of BZO-NR concentration on the physical and transport properties of

vicinal YBCO films

The application of YBCO for devices such as superconducting magnetic-energy storage requires high J_c for H >5 T. A possible route to accomplishing this is to insert strong pinning centers, such as $BaZrO_3$ nanorods (BZO-NRs), with density comparable to the desired matching field. Unfortunately, it has been observed that the critical temperature (T_c) and low field J_c of $YBa_2Cu_3O_{7-\delta}$ (YBCO) films were significantly reduced upon insertion of BZO-NRs and degraded further with increasing density of BZO-NRs [Peurla 2006]. A probable cause of these degradations could be chemical contamination due to Zirconium substitution in the lattice. As a matter of fact, Driscoll *et al* reported the presence of $Ba_2Zr_{2-x}Y_xO_6$ particles in YBCO films doped with 5 mol.% BZO [Macmanuss-Driscoll 2004]. On the other hand, YBCO films doped with self-assembled rare earth tantalite RE_3TaO_7 (RTO, where RE = rare earth, Er, Gd and Yb) did not show any chemical contamination and consequently no T_c degradation [Harrington 2009]. Another likely reason could be the lattice strain produced by the large lattice mismatch of ~8.55% between the YBCO's (ab= 3.86 Å) and the BZO's (a= 4.19 Å) lattice constants [Driscoll 2004, Yamada 2005, Goyal 2005, Kang 2006, Peurla 2006, Peurla 2007, Pompeo 2008, Mele 2008]. Interestingly, insertion of $BaSnO_3$ (BSO), which has a

smaller lattice mismatch of ~6.6% with YBCO, did not diminish the T_c of YBCO as much as BZO insertion did [Mele 2008]. In addition, P. Mele *et al* observed that the expansion along the c-axis is smaller in YBCO/BSO-NRs film as compared to that in YBCO/BZO-NRs film [Mele 2008], suggesting that the latter experiences more lattice strain. Furthermore, YBCO films containing RTO, with lattice mismatch ranging from 1.4-4.7%, did not suffer any T_c degradation at all [Harrington 2009]. This is true even for RTO concentrations of up to 8 mol.% [Harrington 2009]. In contrast, a recent study done by M. Peurla *et al* showed that increasing the BZO-NR concentration increased the lattice strain and consequently decreased the T_c and low field J_c of YBCO films [Peurla 2007]. These observations led us to hypothesize that the lattice strain seems to be a dominant cause responsible for the observed degraded T_c and low field J_c in BZO-NR-doped YBCO films. As a matter of fact, when BZO nanoparticles were introduced in YBCO via a chemical solution deposition technique [Gutierrez 2008], the BZO nanocomposites did not grow epitaxially with the YBCO matrix and the T_c (~91 K) and self field J_c at 77 K (~6.5 MA/cm^2) were not reduced in these films. This suggests that the strain due to lattice mismatch seems not to be the case here. In this light, we believe that reducing or switching the lattice strain in YBCO during BZO-NR insertion is necessary to avoid T_c and low field J_c degradation.

In the previous chapter, we have shown that incorporating BZO-NRs in porous vicinal YBCO films resulted in improved J_c over the range of fields and orientations. Furthermore, degradation in the crystalline structure, T_c and low field J_c,

typically observed in flat YBCO films doped with BZO-NRs was almost eliminated when the BZO-NRs were incorporated in the porous vicinal YBCO films. This suggests that the density of BZO-NRs may be increased without undue damage to the porous vicinal films. In this chapter, we report our results on the effect of the BZO-NR concentration on the physical and transport properties of porous vicinal YBCO films.

7.1 Effect of increasing BZO-NR concentration on the crystalline integrity of flat and vicinal YBCO/BZO-NRs films

YBCO doped with 2 vol.%, 4 vol.% and 6 vol.% BZO-NRs were deposited on flat and 5° vicinal STO substrates. The θ-2θ scans of the un-doped and BZO-doped flat and 5° vicinal YBCO films are shown in Figures 7.1(a) and (b). The peak intensities in the plot were normalized using the YBCO (005) peak intensity and the dashed lines represent the (00ℓ) peaks of the YBCO lattice. All films are highly c-axis oriented for all concentrations of BZO-NRs. Figure 7.1(a) illustrates the evolution of the crystalline structure for the flat YBCO film with increasing BZO concentration. The presence of the BZO (200) peak, marked with an asterisk, suggests that the BZO grew epitaxially with the YBCO film. In addition, the higher BZO (200) peak in the 4 vol.% flat YBCO/BZO-NRs film as compared to that of the 2 vol.% flat YBCO/BZO-NRs film suggests a higher density of BZO-NRs in the former. However, it is interesting to note that the BZO (200) peak decreased when the BZO concentration was increased to 6 vol.%. It is also noticeable in the θ-2θ scans that there are strong peaks corresponding to the different orientations of YBa_2ZrO_6 (YBZO), which are

91

encircled in the plots. This suggests that the reduced T_c observed in flat YBCO/BZO-NRs films can be attributed to the substitution of Zr in the YBCO lattice, which confirms a previous report [Macmanus-Driscoll 2004]. Furthermore, the observed doubling of the YBZO peaks when the BZO concentration was increased from 2 vol.% to 4 vol.% suggests that the observed monotonic T_c degradation in YBCO/BZO-NRs films with increasing BZO concentration [Peurla 2006] is also due to worsening lattice poisoning. However, the diminished YBZO peaks and the absence of other anomalous peaks when the BZO concentration was increased to 6 vol.% suggest that the excess BZO may have grown amorphously inside the YBCO film. Figure 7.1(b) shows the θ-2θ scans of the 5° vicinal YBCO films containing different BZO concentrations. The BZO peaks in these films are not as prominent as those observed in the flat YBCO/BZO-NRs films when the BZO concentration is less than 6 vol.%. Furthermore, the YBZO peaks in the 5° vicinal YBCO/BZO-NRs films did not become obvious until the BZO concentration was increased to 6 vol.%. This implies that the vicinal growth at small angle retards the substitution of Zr in the YBCO lattice.
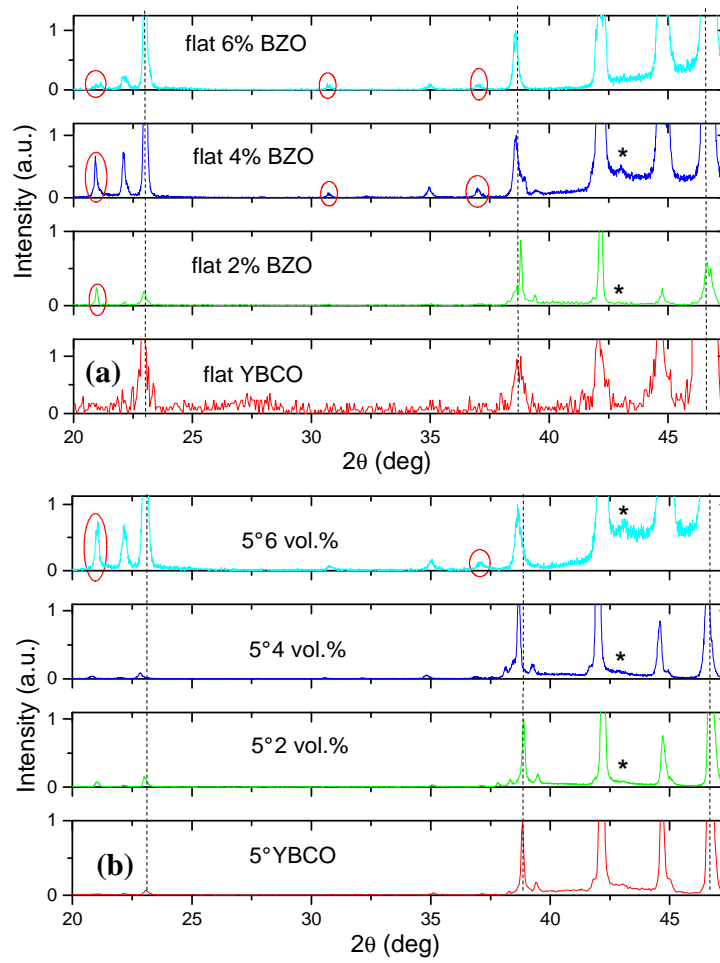
Figure 7.1 θ-2θ plots for (a) flat, (b) 5° vicinal YBCO films containing 0 vol.% (1st row), 2 vol.% (2nd row), 4 vol. % (3rd row) and 6 vol.%. (4th row) BZO. The dashed lines represent the (00ℓ) peaks of the YBCO film while the asterisk marks the BZO (200) peak. The YBa_2ZrO_6 (YBZO) peaks are encircled in red. [Emergo 2009(b)]

The full-width-at-half-maximum (FWHM) values of the (005) and (103) peaks of the eight films depicted in Figure 7.1 were measured and are summarized in Table 7.1. The flat YBCO/BZO-NRs films have greater in-plane and out-of-plane misalignment as compared to all of the vicinal YBCO/BZO-NRs films. This suggests that the vicinal growth promotes better crystalline structure, which could allow better

93

electronic conduction along the ab-plane of the vicinal films leading to lower room temperature resistivities even in the presence of high density BZO-NRs [Crommie 1989]. The in-plane and out-of-plane misalignment of the flat YBCO film increased by 35% and 50%, respectively, when the BZO concentration was increased to 2 vol.%, which is expected due to the increased strain induced during BZO-NR insertion. However, the misalignment of the flat YBCO/BZO-NRs film decreases with increasing BZO concentration. As a matter of fact, the FWHM of the (103) and (005) peaks of the 6 vol.% flat YBCO/BZO-NRs film are more or less the same as those of the un-doped flat YBCO film. This somehow suggests that the substitution of Zr in the YBCO lattice is triggered by the film's need to minimize crystalline disorder. On the other hand, the (103) peak FWHM values of the 5° vicinal YBCO/BZO-NRs seem to fluctuate within ~15% of that of the un-doped 5° vicinal YBCO film. In contrast, the FWHM of the (005) peak appears to increase monotonically with increasing BZO-NRs concentration. Indeed, the FWHM of the 6 vol.% 5° vicinal YBCO/BZO-NRs film is ~480% higher than that of the un-doped 5° vicinal YBCO film. This illustrates that the insertion of BZO-NRs degrades mostly the out-of-plane alignment of the vicinal YBCO films and not the in-plane alignment. This also suggests that the maximum BZO concentration allowable to maintain crystalline integrity in the vicinal film is 4 vol.%.

Lastly, the c-axis lattice constants for the eight films mentioned above were calculated from the position of the (005) peaks and are summarized in Table 7.1. Again, in general, the flat YBCO/BZO-NRs films have longer c-axes than all the 5°

94

vicinal YBCO/BZO-NRs films, confirming the presence of an expansive strain in the former [Mele 2008]. On the other hand, the additional anisotropic strain existing in the vicinal films creates a compressive strain along the c-axis of the latter. Since the separation between the superconducting planes more or less dictates the resulting T_c, all the vicinal films are expected to have higher T_c's than all the flat films [Crommie 1989]. Interestingly, the c-axes of the flat YBCO/BZO-NRs films show a similar trend in the FWHM of the (103) and (005) peaks with respect to increasing BZO concentration. The c-axis constant increased by 0.08 Å when the BZO concentration was increased to 2 vol.% but the former decreased as the BZO concentration was increased. As a matter of fact, the 4 vol.% and 6 vol.% flat YBCO/BZO-NRs films' c-axes are 0.03 Å and 0.07 Å, respectively, smaller than that of the un-doped flat YBCO film, suggesting that the formation of secondary phases, such as YBZO, is indeed strain related and switching the direction of the strain may hinder the formation of unnecessary poisoning of the YBCO lattice. In contrast, for BZO concentrations less than 6 vol.%, the c-axis of the 5° YBCO/BZO-NRs film is within ±0.01 Å of that of the un-doped 5° YBCO/BZO-NRs film, which implies that the addition of BZO-NRs does not significantly alter the lattice of the vicinal YBCO film. However, a significant increase of 0.09 Å was observed in the c-axis of the 6 vol.% 5° vicinal YBCO/BZO-NRs film as compared to that of its un-doped counterpart. This plus the observed significant increase in the out-of-plane misalignment and the enhanced YBZO peak are expected to considerably degrade the superconducting properties of this film.

Sample (%BZO)	FWHM (103)	FWHM (005)	c-axis (Å)	ρ_{300K} (μΩ·cm)	T_c (K)
Flat 0%	0.20°	0.24°	11.74	267.20	89.89
Flat 2%	0.27°	0.35°	11.82	423.48	86.14
Flat 4%	0.23°	0.34°	11.71	475.74	86.02
Flat 6%	0.20°	0.27°	11.67	564.68	84.45
5° 0%	0.20°	0.13°	11.55	214.22	89.55
5° 2%	0.17°	0.15°	11.56	257.65	88.30
5° 4%	0.20°	0.17°	11.54	246.16	89.12
5° 6%	0.19°	0.76°	11.64	306.15	88.93

Table 7.1 Summary of FWHM of (103) and (005) peaks and c-axis length of the flat and 5° vicinal YBCO/BZO-NRs films doped with different BZO concentration.

7.2 Effect of increasing BZO-NRs concentration on the room-temperature resistivity and T_c

Figure 7.2(a) shows the temperature dependence of the resistivity along the longitudinal direction (ρ_L) for all of the eight films mentioned above. The solid symbols correspond to the flat YBCO/BZO-NRs while the open symbols correspond to the vicinal YBCO/BZO-NRs films. Notice that the ρ_{300K} of the un-doped flat YBCO film falls in the range of reported room temperature resistivities of high

quality YBCO films [Foltyn 2007]. The resistivity at 300 K of the flat YBCO/BZO-NRs film increases with increasing BZO concentration. This is shown in more detail in Figure 7.2(b) and the values are summarized in Table 7.1. Although the BZO and YBZO peaks in the θ-2θ scans of the flat YBCO film containing 6 vol.% BZO shrank, the observed increase in ρ_{300K} for this film confirms the presence of additional BZO nanodots and secondary phases, which may be dispersed in their orientations. Furthermore, the flat YBCO/BZO-NRs films have overall higher ρ_L's at 300 K than those of their vicinal counterparts, which is expected due to the higher density of secondary phases and higher crystalline disorder in the former. The room temperature ρ_L of the vicinal YBCO/BZO-NRs film also increases with increasing BZO concentration, as shown in Figure 7.2(b). However, the rate of increase is much smaller in the vicinal YBCO/BZO-NRs film as compared to that of the flat YBCO/BZO-NRs films. In fact, the ρ_{300K} values and ρ-T curves of the 2 vol.% and 4 vol.% vicinal YBCO/BZO-NRs films are very comparable to each other. Surprisingly, although significant out-of-plane misalignment and YBZO density were observed in the 6 vol.% 5° vicinal YBCO/BZO-NRs film, its resistivity is still considerably smaller than that of its flat counterpart.

The T_c's as a function of BZO concentration for the flat and 5° vicinal YBCO/BZO-NRs films are shown in the inset of Figure 7.2(b) and the values are summarized in Table 7.1. In general, all 5° vicinal YBCO/BZO-NRs films have higher T_c values than their flat counterparts, which is expected due to the higher density of secondary phases and longer c-axes in the latter. The T_c decreases with

97

increasing BZO concentration for the flat YBCO/BZO-NRs films. As a matter of fact, the T_c dropped by almost 6 K, when the concentration was increased from 0 vol.% to 6 vol.%. On the other hand, the T_c's of the vicinal YBCO/BZO-NRs films fluctuate only within ~1.25 K of that of the un-doped 5° vicinal YBCO film. The lower T_c observed in the 2 vol.% 5° vicinal YBCO/BZO-NRs film may be due to degradation during patterning. This indeed shows that the vicinal growth impedes the T_c degradation during BZO-NRs insertion. However, it is interesting that the T_c of the 6 vol.% 5° vicinal YBCO/BZO-NRs film is not significantly reduced even though the latter has a more elongated c-axis plus higher out-of-plane misalignment and YBZO density as compared to the other vicinal YBCO/BZO-NRs films.
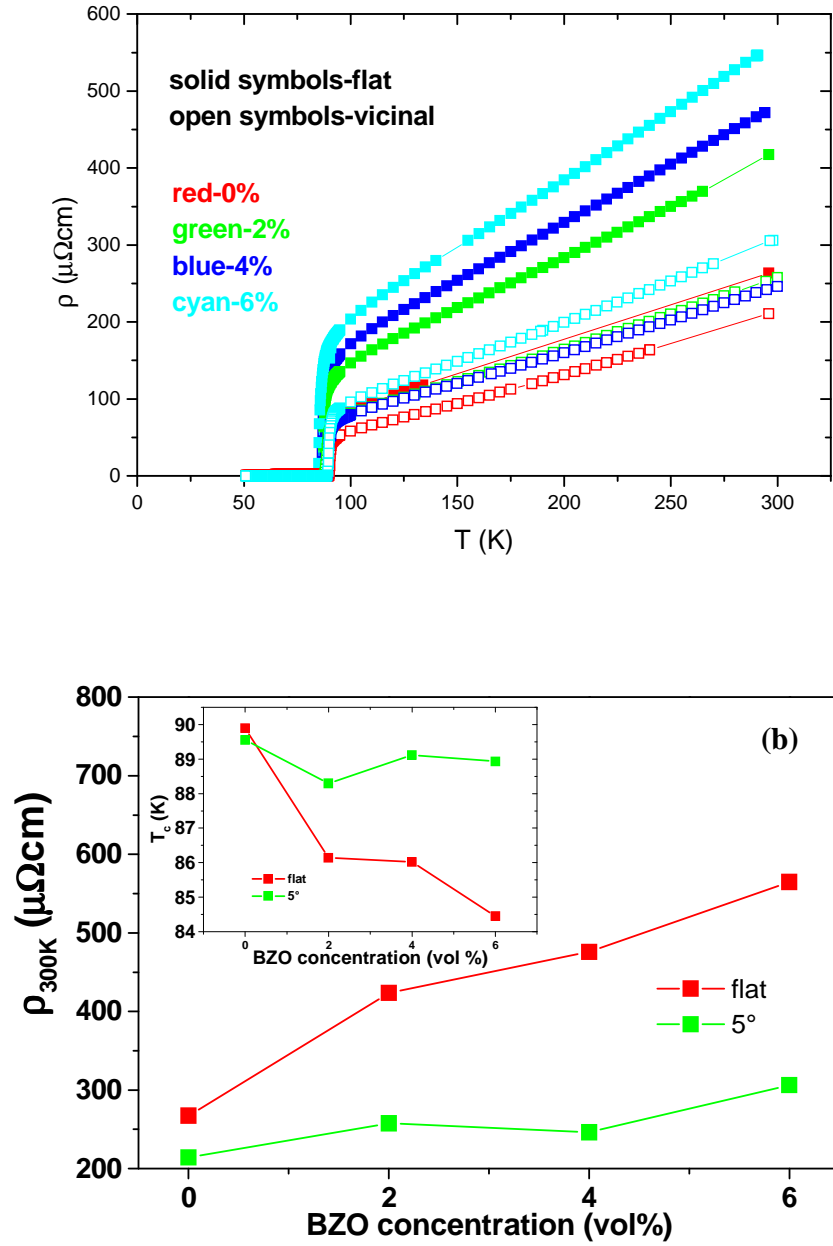
Figure 7.2 (a) Resistivity as function of temperature for the flat and 5° vicinal YBCO/BZO-NRs films containing 0 vol.%, 2 vol.%, 4 vol.% and 6 vol.% BZO concentration; (b) ρ_{300K} as function of BZO concentration for the flat and 5° vicinal YBCO/BZO-NRs films. Inset: T_c as function of BZO concentration for the flat and 5° vicinal YBCO/BZO-NRs films.

7.3 Effect of increasing BZO-NRs concentration on the critical current density

Figure 7.3(a) shows the J_c as a function of H (when the latter is parallel to the film's c-axis) at 77 K for the eight films mentioned above. The solid symbols correspond to the flat YBCO/BZO-NRs while the open symbols correspond to the vicinal YBCO/BZO-NRs films. The J_c values at self field of the flat YBCO and flat YBCO/BZO-NRs films are in the range of reported values. As expected, the flat YBCO/BZO-NRs films carry the lowest SF J_c at all BZO concentrations. Also, the J_c at SF for all films decreases with increasing BZO concentration resulting from the combined effects of decreased T_c and superconducting volume portion due to the increased BZO-NR and YBZO densities. For the flat YBCO/BZO-NRs films, the decrease in SF J_c is more or less linear with the increase in BZO concentration, as shown in more detail in Figure 7.3(b). However, for the vicinal YBCO/BZO-NRs films the drop is not directly proportional to the increase in BZO concentration, suggesting an optimal doping level. As a matter of fact, the change in the SF J_c is not very significant when the BZO concentration was increased from 2 vol.% to 4 vol.%. Thus, the vicinal growth allows insertion of a higher BZO concentration in YBCO films, which is necessary for improving the high field J_c, without sacrificing the low field J_c. Lastly, it is expected that all films will suffer J_c degradation at self field when the concentration is increased to 6 vol.% as a result of advanced YBCO poisoning.

For the flat YBCO/BZO-NRs films, the J_c at H> 3 T (when H||c) was improved when the BZO concentration was increased from 2 vol.% to 4 vol.%. This is most likely due to the increase in the density of BZO-NRs aligned along the c-axis,

which is supported by the observed increase in the BZO (002) peak depicted in Figure 1(a). Quantitatively, the J_c at 5 T increased by ~80% when the BZO concentration was increased from 2 vol.% to 4 vol.%. Considering that the pinning force density is proportional to J_c, this suggests that ~20% of the additional BZO nanoparticles either grew in different orientations or substituted inside the YBCO lattice to form YBZO. In contrast, the J_c value at high field of the 5° YBCO/BZO-NRs film decreased when the BZO concentration was increased from 2 vol.% to 4 vol.%. Since the T_c and J_c at self field were not degraded in this film, it is most likely that the decrease in high field J_c is due to the diminished density of BZO-NRs aligned along the c-axis.
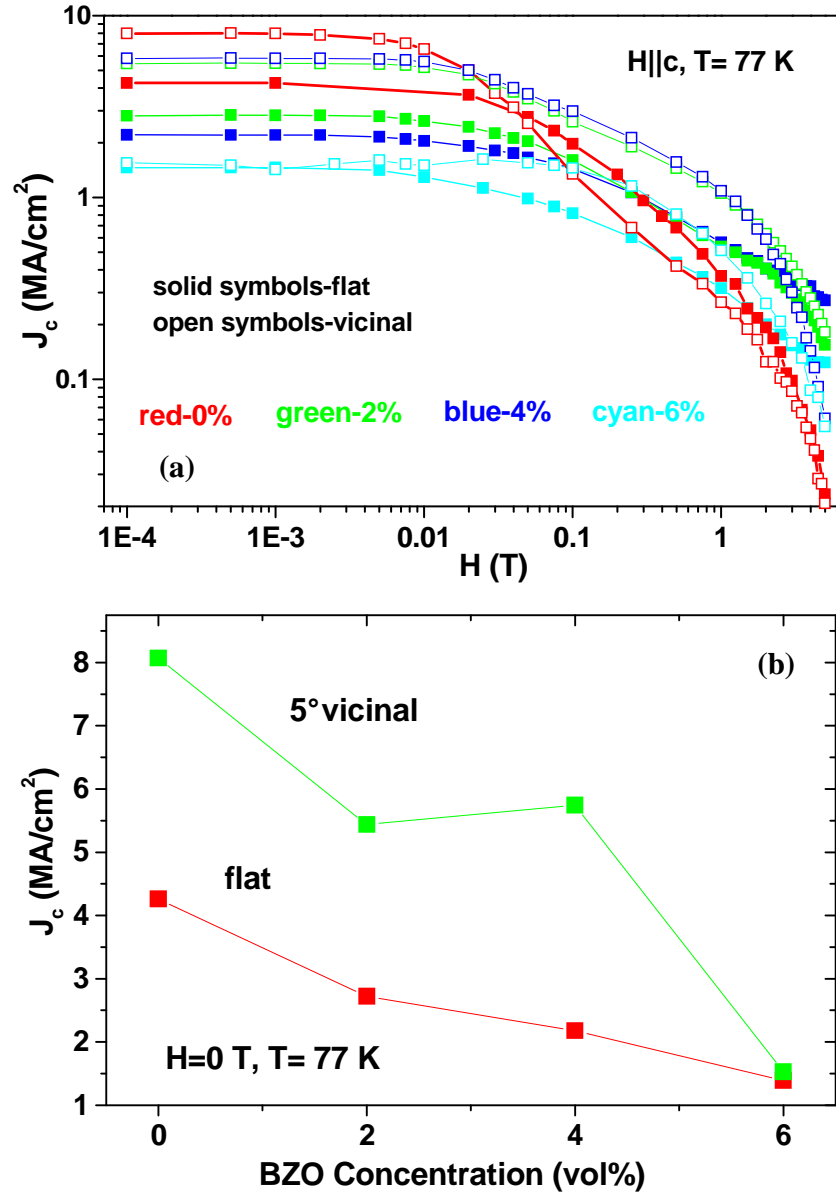
Figure 7.3 (a) J_c as function of H along the c-axis at 77 K for the flat and 5° vicinal YBCO/BZO-NRs films with increasing BZO concentration; (b) J_c at self field as function of BZO concentration for the flat and 5° vicinal YBCO/BZO-NRs films

The angular dependences of J_c at 1 T and 77 K for the eight samples mentioned above are depicted in Figure 7.4. The solid and open symbols correspond to the flat and vicinal YBCO/BZO-NRs films, respectively. For all BZO concentrations, the flat YBCO/BZO-NRs films show a peak when H is along the c-axis, confirming that the BZO nanoparticles assembled into columnar defects aligned along the c-axis. The decreasing peak with increasing BZO-NRs concentration suggests that the additional BZO-NRs are only helpful at applied fields greater than 1 T. On the other hand, for the vicinal YBCO/BZO-NRs film, the J_c-θ peak when H is along the c-axis ($\theta=0°$) is only observable when the BZO concentration is equal to 2 vol.%. This confirms that the low J_c values at H>3 T in vicinal YBCO/BZO-NRs film is indeed due to the lack of c-axis aligned columnar defects. However, the J_c-θ peak when H is in the ab-plane is enhanced significantly in the vicinal YBCO/BZO-NRs film when the concentration was increased to 4 vol.%. As a matter of fact, an amazing J_c value of ~4 MA/cm^2 was achieved in this film at 1 T. This corresponds to a pinning force density of ~37.37 GN/m^3. This implies that the vicinal film retards lattice degradation by switching the alignment of additional BZO-NRs along the ab-plane. Also, the diminished J_c values over the entire field range for both H||c and H||ab directions in the 6 vol.% vicinal YBCO/BZO-NRs film suggests that the optimal BZO concentration in the vicinal YBCO/BZO-NRs film is 4 vol.%.
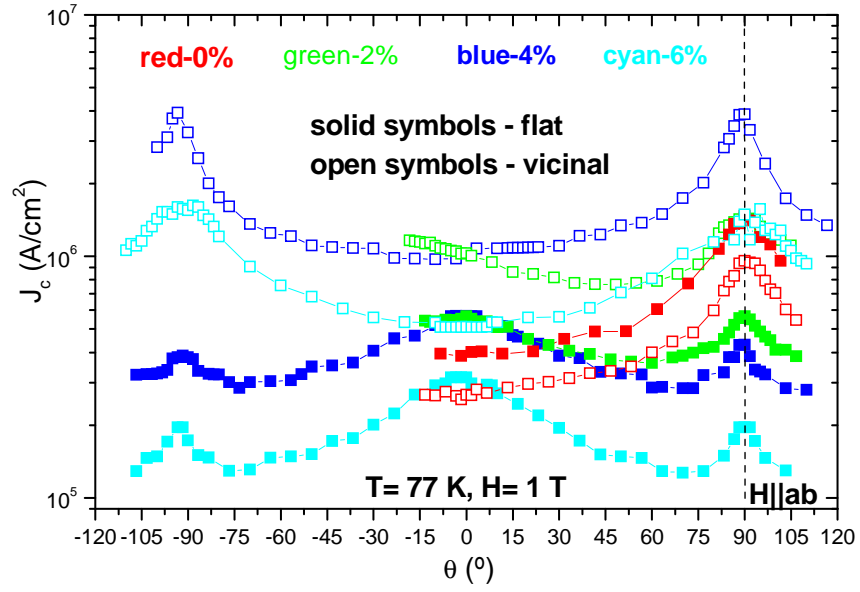
Figure 7.4 Angular dependence of J_c at 1 T and 77 K for the flat and 5° vicinal YBCO/BZO-NRs films doped with different BZO concentrations.

Chapter 8

Conclusions

Addressing issues involved in improving $J_c(B,\theta)$ is necessary for making YBCO suitable for power-related device applications. In this work, significant enhancements in J_c over a wide range of field strength and orientation were achieved in YBCO films by tailoring pinning structures at the nanometer scale.

Through-thickness nanopores were incorporated inside the YBCO films by depositing the films on as-received commercial vicinal STO substrates. The Y_2O_3 nanoparticles were observed to catalyze the nucleation of nanopores while the vicinal growth promoted the evolution of the nanopores throughout the film thickness. The porous vicinal YBCO films contain uniformly distributed nanopores of density around 2-8/μm^2, which appears to be independent of the substrate vicinal angle (θ_v) over the range 5-20°. The pores' dimensions are in the range of a few to a few hundreds of nm. The morphology of the pores experiences a systematic change with increasing vicinal angle. The pores are more isotropic at smaller angles whereas they become squeezed along the transverse direction (perpendicular to the surface steps) and become considerably anisotropic at higher angles.

The resistivities ρ_L along the longitudinal direction of the porous vicinal YBCO films were found to be close to those of the nonvicinal reference YBCO films in the normal state. The anisotropy of the resistivity ρ_c/ρ_{ab} is comparable to that

observed in twinned YBCO single crystals. In addition, the ρ_c/ρ_{ab} vs. T curves of the three vicinal films more or less overlap in the temperature range of 100-300 K. These results, together with the sub-Kelvin T_c discrepancy of these samples with respect to the reference nonvicinal YBCO films, suggest that the effect of nanopores on the electronic properties of the porous vicinal films is minimal.

The MO images showed that the magnetic flux penetration in the flat samples is isotropic while it is highly anisotropic in the vicinal samples. A significantly enhanced $J_{c,L}$ (J_c along the longitudinal direction), up to 8.3 MA/cm^2 at 77 K and self field has been obtained for the porous vicinal YBCO films. The close correlation between the J_c value and the pinning potential energy, U_p, suggests that the strong pinning on the nanopore surface is responsible for the observed high J_c and higher pore density may allow one to extend the high J_c to higher H fields. The higher $J_{c,T}$ (J_c along the transverse direction) in porous vicinal YBCO films as compared to that of nonporous vicinal counterparts implies that the isotropic pore surface pinning also enhances the J_c values along the transverse direction. A significant decrease in the J_c when the applied magnetic field exceeded the matching field of the nanopores, H_m, suggests a switch from pore surface pinning to bulk pinning, which justifies the need to further increase the density of the nanopores for high-field applications.

Splayed BZO nanorods were generated by depositing 2 vol.% BZO-doped YBCO films on 5° vicinal STO substrates. The interplay between the lattice strain caused by the large lattice mismatch between YBCO and BZO and the anisotropic strain due to the vicinal growth resulted in the dispersed orientation of BZO-NRs in

106

the range of 9.7 ± 3.0° around the c-axis. This is almost twice the range observed in its flat counterpart and corresponds to the optimal splay angle predicted by theory. The splayed BZO-NRs proved to be more effective in pinning magnetic vortices, as demonstrated by the higher maximum pinning force density and higher $J_c(H)$ up to 5 T in the 5° vicinal YBCO/BZO-NRs films as compared to the flat YBCO/BZO-NRs films. Furthermore, the splayed BZO-NRs can provide more isotropic strong pins to the vicinal YBCO/BZO-NRs films leading to an enhanced J_c at all orientations of the applied magnetic field. Finally, the additional benefit of the vicinal growth is the slight compression of the c-axis of the YBCO film and improved out-of-plane alignment, resulting in minimized T_c degradation and enhanced electronic conduction along the longitudinal direction. This suggests that a higher concentration of BZO-NRs can be inserted in the vicinal YBCO films with minimal detrimental consequences.

YBCO films doped with 2 vol.% BZO nanorods were deposited on flat, 5°, 10° and 20° vicinal STO substrates to determine the effect of the vicinal angle on the alignment of the BZO-NRs. It was observed that the peak of the J_c-θ plot when H is along the c-axis disappears and the J_c value decreases with increasing substrate vicinal angle. This plus the narrowing and increasing peak in the H∥ab direction when the vicinal angle is increased suggest that the BZO-NRs along the c-axis can be switched to align along the ab-plane at θ_v= 20°. This shows a novel method of employing the vicinal growth to control the alignment of BZO-NRs inside the YBCO film.

Lastly, 2 vol.%, 4 vol.% and 6 vol.% YBCO/BZO-NRs films were deposited on flat and 5° vicinal STO substrates. The flat YBCO/BZO-NRs films contained a

higher density of secondary phases (such as YBZO) and more lattice misalignment than the vicinal YBCO/BZO-NRs films upon increase of the BZO concentration. This suggests that the vicinal growth impedes lattice poisoning in BZO-NRs doped YBCO films and results in slower degradation of T_c and low field J_c values. The diminished J_c-θ peak when His along the c-axis and the enhanced J_c-θ peak when H is in the ab-plane for vicinal YBCO/BZO-NRs films containing BZO concentrations greater than 2 vol.% suggests that the vicinal growth prevents the degradation of normal and superconducting properties of the BZO-doped YBCO film by aligning the excess BZO-NRs along the ab-plane. At the moment, further studies are necessary to determine the mechanism of nanotube pore and BZO-NR formation in vicinal YBCO films. A detailed microstructural study of very thin BZO-doped YBCO films deposited on vicinal STO substrates may provide a clue for this.

All samples studied in this work were deposited on single crystal substrates so the next logical step is to transfer the technique of creating nanotube pores and splayed BZO-NRs to YBCO coated conductors. A major component of these techniques is the vicinal growth, so the first and foremost challenge is to create a vicinal template on the coated conductor substrate. An ion beam assisted deposition technique could be helpful in creating these templates [Vallejo 2006].

References

Aytug, T., et al, J. Appl. Phys. **98**, 114309 (2005).

Baca, F.J., Fisher, D., Emergo, R.L.S. and Wu, J.Z., Supercond. Sci. Technol. **20,** 554 (2007).

Baca, F.J., Barnes, P.N., Emergo, R.L.S., Haugan, T.J., Reichart, J. and Wu, J.Z., Appl. Phys. Lett. **94,** 102512 (2009).

Bardeen, J., Cooper, L. N. and Schrieffer, J. R., Physical Review 108 (1957).

Blatter, G., Feigelman, M.V. and Geshkenbein, V.B., Rev. Mod. Phys. **66**, 1125 (1994).

Brandt, E.H., Phys. Rev. Lett. **69,** 1105 (1992).

Brandt, E.H. and Indenbom, M., Phys. Rev. B **48,** 893 (1993).

Brötz, J., Fuess, H., Haage, T., Zegenhagen, J., Jooss, Ch., Forkl, A. and Warthmann, R., J. Appl. Phys. **85**, 635 (1999).

Busch, H., Fink, A. and Müller, A., J. Appl. Phys. **70**, 2449-2451 (1991).

Campbell, A.M., and Evetts, J.E., Critical Currents in Superconductors. Taylor and Francis Ltd, London: 1972.

Cantoni, C., Verebelyi, D.T., Specht, E.D., Budai, J. and Christen, D.K., Phys. Rev. B **71**, 054509 (2005).

Chakalova, R.I., Jackson, T.J., Passerieux, G., Jones, I.P., Mikheenko, P., Muirhead, C.M. and Darlington, C.N.W., Phys. Rev. B **70**, 214504 (2004).

Civale, L., Krusin-Elbaum, L., Thompson, J.R., Wheeler, R., Marwick, A.D., Kirk, M.A., Sun, Y.R., Holtzberg, F. and Field, C., Phys. Rev. B **50,** 4102 (1994).

Civale, L., Maiorov, B., MacManus-Driscoll, J.L., Wang, H., Holesinger, T.G., Foltyn, S.R., Serquis, A. and Arendt, P.N., IEEE Trans. on Appl. Supercond. **15**, 2808 (2005).

Cohen, S.H. and Lightbody M.L., Atomic Force Microscopy/Scanning Tunneling Microscopy 2 (Hardcover). Plenum Publishing Corporation, New York: 2008.

Crommie, M.F., Liu, A.Y., Zettl, A., Cohen, M.L., Parilla, P., Hundley, M.F., Creager, W.N., Hoen, S. and Sherwin, M.S., Phys. Rev. B **39**, 4231 (1989).

Czerwinka, P.S., King, P.J., Misat, S., Campion, R.P., Staddon, C.R. and Villegier, J.C., Phys. Rev. B **65**, 184509 (2002).
Dam, B. et al, Nature **399**, 439 (1999).

Djupmyr, M., Cristiani, G., Habermeier, H.-U. and Albrecht, J., Phys. Rev. B **72**, 220507(R) (2005).

Emergo, R.L.S., Wu, J.Z., Aytug, T. and Christen, D.K., Appl. Phys. Lett. **85**, 4 (2004).

Emergo, R.L.S., Wu, J.Z., Haugan, T.J. and Barnes, P.N., Appl. Phys. Lett. **87**, 232503 (2005).

Emergo, R.L.S., Wu, J.Z., Haugan, T.J. and Barnes, P.N., Supercond. Sci. Technol. **21,** 085008 (2008).

Emergo, R.L.S., Baca, F.J., Wu, J.Z., Haugan, T.J. and Barnes, P.N., in preprint

Emergo, R.L.S., Baca, F.J., Wu, J.Z., Haugan, T.J. and Barnes, P.N., in preprint

Foltyn, S.R., Tiwari, P., Dye, R.C., Le, M.Q., and Wu, X.D, Appl. Phys. Lett. **63**, 1848 (1993).

Foltyn, S.R., Jia, Q.X., Arendt, P.N., Kinder, L., Fan, Y. and Smith, J.F., Appl. Phys. Lett. **75,** 3692 (1999).

Foltyn, S.R., Arendt, P.N., Jia, Q.X., Wang, H., Macmanus-Driscoll, J.L., Kreiskott, S., De Paula, R.F., Stan, L., Groves, J.R. and Dowden, P.C., Appl. Phys. Lett. **82,** 4519 (2003).

Foltyn, S.R., Civale, L., MacManus-Driscoll, J.L., Jia, Q.X., Maiorov, B., Wang, H. and Maley, M., Nat. Mater. **6,** 631 (2007), and many references therein.

Friedmann, T.A., Rabin, M.W., Giapintzakis, J., Rice, J.P. and Ginsberg, D.M., Phys. Rev. B **42**, 6217 (1990).

Gerber, C., Anselmetti, D., Bednorz, J.G., Mannhart, J., Schlom, D.G., Nature **350**, 279 (1991).

Goldstein, J., Newbury, D.E., Joy, D.C., Lyman, C.E., Echlin, P., Lifshin, E., Sawyer, L.C. and Michael J.R. Scanning Electron Microscopy and X-ray Microanalysis (Hardcover). Springer, New York: 2003.

Goyal, A., Kang, S., Leonard, K.J., Martin, P.M., Gapud, A.A., Varela, M., Paranthaman, M., Ijaduola, A.O., Specht, E.D., Thompson, J.R., Christen, D.K., Pennycook, S.J. and List, F.A., Supercond. Sci. Technol. **18,** 1533 (2005).

Gutierrez, J., Llordes, A., Gazquez, J., Gibert, M., Roma, N., Ricart, S., Pomar, A., Sandiumenge, F., Mestres, N., Puig, T. and Obradors, X., Nat. Mater. **6**, 367 (2007).

Haage, T., Zegenhagen, J., Li, J.Q., Habermeier, H.-U. and Cardona, M., Phys. Rev. B **56**, 8404 (1997).

Habermeier, H.-U., Haage, T., Zegenhagen, J., Warthmann, R. and Joos, Ch., Supercond. Sci. Technol. **11,** 929 (1998).

Hardy, V., Ruyter, A., Wahl, A., Maignan, A., Groult, D., Provost, J., Simon, Ch. and Noël, H., Physica C **257,** 16 (1996).
Harrington, S.A., Durrell, J.H., Maiorov, B., Wang, H., Wimbush, S.C., Kursumovic, A., Lee, J.H. and MacManus-Driscoll, J.L., Supercond. Sci. Technol. **22,** 022001 (2009).

Haugan, T., Barnes, P.N., Brunke, L., Maartense, I. and Murphy, J., Physica C **397,** 47 (2003).

Haugan, T., Barnes, P.N., Maartense, I., and Cobb, C.B., Lee, E.J. and Sumption, M., J. Mat. Res. **18,** 2618 (2003).

Haugan, T.J., Barnes, P.N., Wheeler, R., Meisenkothen, F. and Sumption, M., Nature **430**, 867 (2004).

Hawley, M., Raistrick, I.D., Beery, J.G. and Houlton R.J., Science **251,** 1587 (1991).

Hwa, T., Doussal, P.L., Nelson, D.R. and Vinokur, V.M., Phys. Rev. Lett. **71,** 3545 (1993).

Huebner, R.P. Magnetic Flux Structures in Superconductors. Springer, Berlin: 2001.

Hunt, T.K., Phys. Rev. **151,** 325 (1966).

Jooss, Ch., Warthmann, R., Kronmuller, H., Haage, T., Habermeier, H.-U. and Zegenhagen, J., Phys. Rev. Lett. **82**, 632 (1999).

Jooss, Ch., Warthmann, R. and Kronmuller, H., Phys. Rev. B **61**, 12433 (2000).

Kang, B. W., Goyal, A., Lee, D. R., Mathis, J. E., Specht, E. D., Martin, P. M., Kroeger, D. M., Paranthaman, M. and Sathyamurthy, S., J. Mater. Res. **17,** 1750 (2002).

Kang, S., Goyal, A., Li, J., Martin, P.M., Heatherly, L., Thompson, J.R., Christen, D.K., List, F.A., Paranthaman, M., and Lee, D.F., Science **311**, 1911 (2006).

Kittel, C., Introduction to solid state physics 7th Ed. Wiley, New Jersey: 1995.

Krusin-Elbaum, L., Marwick, A.D., Wheeler, R., Feild, C., Vinokur, V.M., Leaf, G.K. and Palumbo, M., Phys. Rev. Lett. **76,** 2563 (1996).

Larbalestier, D., Gurevich, A., Feldman, D.M., Polyanskii, A., Nature 414, 368-377 (2001).

London, F., Superfluids Volume I. Dover, New York: 1950.

London, H., Phys. Lett., **6,** 162 (1963).

Lowndes, D.H., Zheng, X.-Y., Zhu, S., Budai, J.D. and Warmack, R.J., Appl. Phys. Lett. **61**, 852 (1992).

Lowndes, D.H., Christen, D.K., Klabunde, C.E., Wang, Z.L., Kroeger, D.M., Budai, J.D., Zhu, S. and Norton, D.P., Phys. Rev. Lett. **74**, 2355 (1995).

Luborsky, F.E., Kwasnick, R.F., Borst, K., Garbauskas, M.F., Hall, E.L., and Curran M.J., J. Appl. Phys. **64**, 6388 (1988).

Macmanus-Driscoll, J.L., Foltyn, S.R., Jia, Q.X., Wang, H., Serquis, A., Civale, L., Maiorov, B., Hawley, M.E., Hawley, M.P. and Peterson, D.E., Nature Materials **3**, 439 (2004).

Matsumoto, K., Horide, T., Osamura, K., Mukaida, M., Yoshida, Y., Ichinose, A. and Horii, S., Physica C **412**, 1267 (2004).

Matsushita, T., Supercon. Sci. Technol. **13,** 730-737 (2000).

Matsushita, T., Flux Pinning in Superconductors. Springer, New York: 2007.

Mechin, L., Berghuis, P. and Evetts, J.E., Physica C **302**, 102 (1998)

Meissner, W. and Ochsenfeld, R., Naturwissenschaften 21, 787 (1933)

Mele, P., Matsumoto, K., Horide, T., Ichinose, A., Mukaida, M., Yoshida, Y., Horii, S. and Kita, R., Supercond. Sci. Technol. **21,** 032002 (2008).

Miura, S., Hashimoto, K., Wang, F., Enomoto, Y. and Morishita, T., Physica C **278,** 201-206 (1997).

Onnes, H. K., Comm. Leiden 120b (1911).

Orlando, T.P. Foundations of Applied Superconductivity. Addison-Wesley Publishing Company, Massachusetts: 1991.

Paranthaman, M., Park, C., Cui, X., Goyal, A., Lee, D.F., Martin, P.M., Verebelyi, D.T., Norton, D.P., Christen, D.K. and Kroeger, D.M., J. Mater. Res. **15,** 2647 (2000).

Park, J.H., Kim, D.H., Shim, S.Y., Kim, Y.H., Lee, J.M., Hahn, T.S., Hettinger, J.D. Steel, D.G., Gray, K.E., Glagola, B., Lee, J. and Khim, Z.G., Physica C **281,** 310 (1997).

Poole Jr., C.P. ed. Handbook of Superconductivity. Academic Press, San Diego: 2000.

Pedarnig, J.D., Rössler, R., Delamare, M.P., Lang, W., Bäuerle, D., Köhler A. and Zandbergen, H.W., Appl. Phys. Lett. **81**, 2587 (2002).

Perkins, G.K., Bugoslavsky, Yu.V. and Caplin, A.D. Supercond. Sci. Technol. **15**, 1140 (2002).

Peurla, M., Paturi, P., Stepanov, Y.P., Huhtinen, H., Tse, Y.Y., Bodi, A.C., Raittila, J. and Laiho, R., Supercond. Sci. Technol. **19**, 767 (2006).

Peurla, M., Huhtinen, H., Tse, Y.Y., Raittila, J., and Paturi, P., IEEE Trans. on Applied Superconductivity, **17**, 3608 (2007).

Polyanskii, A.A., Gurevich, A., Pashitski, A.E., Heinig, N.F., Redwing, R.D., Nordman, J.E. and Larbalestier, D.C., Phys. Rev. B **53** 8687 (1996).

Polyanskii, A.A., Cai, X.Y., Feldmann, D.M., Larbalestier, D.C. Nano-crystalline and Thin Film Magnetic Oxides, edited by I. Nedkov and M. Ausloos, NATO Science Series 3: High Technology Kluwer Academic, Dordrecht, 353 (1999).

Polyanskii, A.A., Feldmann, D.M. and Larbalestier, D.C., Magneto-Optical Characterization Techniques, edited by D. Cardwell, Handbook of Superconducting

Materials, University of Cambridge, UK; D. Ginley, NREL IOP, Bristol, 1551 (2003).

Polyanskii, A., Emergo, R.L.S., Wu, J.Z., Aytug, T., Christen, D.K., Perkins, G.K. and Larbalestier, D., Phys. Rev. B **72**, 174509 (2005).

Pompeo, N., Galluzzi, V., Augieri, A., Fabbri, F., Celentano, G., Petrisor, T., Rogail, R. and Silva, E., Journal of Physics: Conference Series **97,** 012173 (2008).

Roas, B., Shultz, L., Saemann-Ischenko, G., Physical Review Letters 64, 479-482 (1990).

Stavrev, S. , Dissertation (2002).

Tahara, S., Anlage, S., Halbritter, J., Eom, C.B., Fork, D.K., Geballe, T.H. and Beasley, M.B., Phys. Rev. B **41**, 11203 (1991).

Takenaka, K., Mizuhashi, K., Takagi, H. and Uchida, S., Phys. Rev. B **50**, 6534 (1994).

Tinkham, M., Introduction to Superconductivity. McGraw-Hill, Inc., New York: 1996.

Vallejo, R.N., Disseration (2006).

Van der Beek, C.J. and Konczykowski, M., Phys. Rev. B **66,** 024523 (2002).

Wang, X., Dibos, A. and Wu, J.Z., Phys. Rev. B **77**, 144525 (2008).

Wang, X., published thesis (2008).

Warren, B.E. X-Ray Diffraction. Dover Publications: 1990.

Wu, J.Z., Emergo, R.L.S., Wang, X., Xu, G., Haugan, T.J., and Barnes, P.N., Appl. Phys. Lett. 93, 062506 (2008).

Yamada, Y., Takahashi, K., Kobayashi, H., Konishi, M., Watanabe, T., Ibi, A., Muroga, T., Miyata, S., Kato, T., Hirayama, T. and Shiohara, Y., Appl. Phys. Lett. 87, 132502-1 (2005).

Yun, S.H., Pedarnig, J.D., Rossler, R., Bauerle, D. and Obradors, X., Appl. Phys. Lett. **77**, 1369 (2000).

List of Publications

1. Vicinal growth impedes degradation of superconducting properties in $BaZrO_3$-doped $YBa_2Cu_3O_{7-\delta}$ films
   R.L.S. Emergo, J.Z. Wu, F.J. Baca, T.J. Haugan, and P.N. Barnes, in preprint

2. Control of $BaZrO_3$ nanorod alignment in $YBa_2Cu_3O_{7-x}$ thin films by microstructural modulation
   F.J. Baca, P.N. Barnes, R.L.S. Emergo, T.J. Haugan, J. Reichart and J.Z. Wu, Appl. Phys. Lett. **94,** 102512 (2009)

3. Generating Splayed $BaZrO_3$ nanorods in $YBa_2Cu_3O_{7-\delta}$ films
   R.L.S. Emergo, J.Z. Wu, F.J. Baca, T.J. Haugan, and P.N. Barnes, in preprint

4. Strong nanopore pinning enhances J_c in $YBa_2Cu_3O_{7-\delta}$ films
   J.Z. Wu, R.L.S. Emergo, X. Wang, G. Xu, T.J. Haugan, and P.N. Barnes, Appl. Phys. Lett. **93,** 062506 (2008)

5. Anisotropy of resistivity and critical current density of porous vicinal $YBa_2Cu_3O_{7-\delta}$ films
   R.L.S. Emergo, J.Z. Wu, T.J. Haugan and P.N. Barnes, Supercond. Sci. Technol. **21,** 085008 (2008)

6. Pore formation and increased critical current density in $YBa_2Cu_3O_{7-\delta}$ films deposited on a substrate surface modulated by Y_2O_3 nanoparticles,
   F.J. Baca, D. Fisher, R.L.S. Emergo and J.Z. Wu, Supercond. Sci. Technol. **20,** 554 (2007)

7. Fabrication and characterization of two-pole X-band $HgBa_2CaCu_2O_{6+\delta}$ microstrip filters
   J.R. Dizon, H. Zhao, J. Baca, S. Mishra, R.L.S. Emergo, R.S. Aga, Jr., and J.Z. Wu, Appl. Phys. Lett. **88,** 092507 (2006)

8. Magneto-optical imaging and electromagnetic study of $YBa_2Cu_3O_{7-\delta}$ vicinal films of variable thickness
   A. Polyanskii, R.L.S. Emergo, J.Z. Wu, T. Aytug, D.K. Christen, G.K. Perkins and D. Larbalestier, Phys. Rev. B **72,** 174509 (2005)

9. Tuning porosity of $YBa_2Cu_3O_{7-\delta}$ vicinal films by insertion of Y_2BaCuO_5 nanoparticles
   R.L.S. Emergo, J.Z. Wu, T.J. Haugan and P.N. Barnes, Appl. Phys. Lett. **87,** 232503 (2005)

10. Thickness dependence of superconducting critical current density in vicinal $YBa_2Cu_3O_{7-\delta}$ thick films
R.L.S. Emergo, J.Z. Wu, T. Aytug and D.K. Christen, Appl. Phys. Lett. **85,** 618 (2004)

11. Magnetic flux pinning enhancement in $HgBa_2CaCu_2O_{6+\delta}$ films on vicinal substrates
Y.Y. Xie, J.Z. Wu, S.H. Yun, R.L.S. Emergo, R. Aga and D.K. Christen, Appl. Phys. Lett. **85,** 70 (2004)